Fluid-structure interaction of flexible lifting bodies with multi-body dynamics of order-reduced models and the actuator-line method

Vom Promotionsausschuss der
Technischen Universität Hamburg-Harburg
zur Erlangung des akademischen Grades
Doktor-Ingenieur (Dr.-Ing.)

genehmigte Dissertation

von

Sönke Neumann

aus Soltau

2016

Bibliografische Information der Deutschen Nationalbibliothek
Die Deutsche Nationalbibliothek verzeichnet diese Publikation in der Deutschen Nationalbibliografie; detaillierte bibliografische Daten sind im Internet über `http://dnb.dnb.de` abrufbar.

1. Gutachter: Prof. Dr. Norbert Hoffmann
2. Gutachter: Prof. Dr.-Ing. Alexander Düster

Tag der mündlichen Prüfung: 19.02.2016

Fluid-structure interaction of flexible lifting bodies with multi-body dynamics of order-reduced models and the actuator-line method
Sönke Neumann

Verlag: epubli GmbH, Berlin, `www.epubli.de`

URN `urn:nbn:de:gbv:830-88214013`
ISBN 978-3-7375-9146-1
1. Auflage 2016

PREFACE

ABSTRACT

The development of complex energy converters generates currently unresolved demands on simulation tools. In this thesis, a model-based method to represent fluid-structure interaction is developed using the example of vertical-axis turbines. The kinematics of a turbine are simulated with a multi-body approach supporting flexible bodies. The dynamics of the flexible bodies are based on order-reduced models.

The fluid domain is represented by Reynolds-averaged Navier-Stokes equations combined with an actuator-line method, a reduced model of the blade approximated by external forces in the momentum equations. Coupling of mechanical and fluid solver is achieved by a two-way iterative approach. The convergence rate is increased by usage of a step prediction based on quasi-Newton methods. An acceleration using a proper orthogonal decomposition to decompose the system dynamics achieves the fastest convergence rates. As an alternative to the partitioned approach a monolithic approach is outlined and its restrictions by using the selected solvers are identified.

The simulation method is validated with experimental data and applied to vertical-axis turbines, both in air and water domains. Extensive validation of uncoupled flow problems and coupled dynamic response of turbines is accomplished. The results are in good agreement with experimental data and analytic solutions. Comparison to potential flow and streamtube methods shows the enhanced accuracy of the developed tool chain. Compared to available, fully meshed solutions, the computational costs are significantly lower.

Conclusively, a vertical-axis tidal turbine with flexible blades is simulated and deflections are compared to a linear solution. The local blade deflections are examined and linked to wake-body interaction.

ABSTRAKT

Die Entwicklung von innovativen Quellen erneuerbarer Energie stellt neue Anforderungen an Simulationswerkzeuge. In dieser Dissertation werden modellbasierte Methoden zur Abbildung einer Fluid-Struktur-Interaktion am Beispiel einer Vertikalachsenturbine entwickelt. Die Kinematik einer Turbine wird durch einen Mehrkörperansatz mit flexiblen Körpern simuliert. Die Dynamik der flexiblen Körper ist durch ordnungsreduzierte Modelle repräsentiert.

Die Fluiddynamik wird über Reynolds-gemittelte Navier-Stokes-Gleichungen in Verbindung mit einer Aktuatorlinienmethode abgebildet. Diese benutzt ein reduziertes Modell eines Tragfügels, der durch externe Kräfte in den Momentengleichungen angenähert wird. Die Kopplung von mechanischem und Fluid-Löser wird über einen iterativen Zwei-Wege-Ansatz durchgeführt. Die Konvergenzraten der Kopplung sind über eine Iterationsschrittvorhersage basierend auf quasi-Newton Methoden beschleunigt. Eine Vorhersage, die Systemdynamiken durch orthogonale Zerlegung (*proper orthogonal decomposition*) auflöst, erzielt die schnellsten Konvergenzraten. Alternativ zum partiellen ist ein monolithischer Ansatz skizziert und die Einschränkungen im Zusammenhang mit den gewählten Methoden identifiziert.

Die Methoden sind mit Experimentdaten validiert und für Vertikalachsenturbinen in Luft und Wasser eingesetzt. Eine umfassende Validierung anhand von ungekoppelten Strömungsproblemen und gekoppelten, dynamischen Simulationen einer Turbine werden durchgeführt. Die Ergebnisse stimmen gut mit Experimentdaten und analytischen Lösungen überein. Der Vergleich zu Methoden basierend auf Potentialströmungen oder der *double-multiple streamtube method* (DMST) zeigt die höhere Genauigkeit des entwickelten Simulationsbaukasten. Im Vergleich zu verfügbaren, vollvermaschten Lösungen ist der Berechnungsaufwand signifikant geringer.

Abschließend wird eine Vertikalachsenturbine für Gezeitenströmungen mit flexiblen Blättern simuliert und die Verbiegungen mit einem linearen Ansatz verglichen. Die lokalen Verbiegungen werden untersucht und in Verbindung zur Interaktion von Wirbeln und Auftriebskörper gesetzt.

ACKNOWLEDGEMENTS

I would like to thank my supervisor Prof. Norbert Hoffmann for his support, guidance, trust in my work and the opportunity to work in both academic and engineering orientated projects. In addition, I would like to thank Dr. David Tempelmann for his constructive ideas and academic guidance.

Then my (former) colleagues in the Dynamics Group, at the Institute of Mechanics and Ocean Engineering and in the projects at Bosch, namely Amin Chabchoub, Andy Witt, Axel Hackbart, Bernhard Stingl, Cem Bassoy, Christian Radisch, Dennis Bünte, Eugen Solojow, Jasper Behrendt, Leo Dostal, Ludwig Krumm, Merten Tiedemann and the one I missed to list. All of them made these three years interesting and often initiated stimulating talks.

I like to thank Arne Wenzel for his collaboration, inspiration, motivation, reliance and of course his work in the ALM. And he is always a good driver or shotgun.

Additionally, I would like to thank Mr. Reinhard Resch, Mr. Tommaso Solcia and Prof. Pierangelo Masarati for their helpful hints at implementing the connection towards MBDyn.

In closing, I like to thank my parents, my family and friends for their aid, support and trusting in me, my sister for her academic advice and Carole for her love and trust.

CONTENTS

LIST OF TABLES

LIST OF FIGURES

ACRONYMS

ALE	arbitrary Lagrangian–Eulerian
ALM	actuator-line method
BET	blade element theory
BiCGSTAB	biconjugate gradient stabilized method
CFD	computational fluid dynamics
DAE	differential-algebraic equation
DOF	degree of freedom
DST	double-multiple streamtube
FE	finite-element
FEM	finite-element method
FSI	fluid-structure interaction
GRP	glass-reinforced plastic
HAWT	horizontal-axis wind turbine
IRS	improved reduced system
LLT	lifting-line theory
LS	least squares
MBS	multi-body system
MOR	model order reduction
NACA	national advisory committee for aeronautics
OpenFOAM	open source field operation and manipulation
OWC	oscillating water column
OWSC	oscillating wave surge converter
PIMPLE	PISO-SIMPLE algorithm

PISO	transient solver for incompressible flows
POD	proper orthogonal decomposition
PTO	power take-off
RANS	Reynolds-averaged Navier-Stokes
RBF	radial basis function
SEREP	system equivalent reduction expansion process
SIMPLE	steady-state solver for incompressible, turbulent flows
TSR	tip speed ratio
URANS	unsteady Reynolds-averaged Navier-Stokes
VATT	vertical-axis tidal turbine
VAWT	vertical-axis wind turbine
VLM	vortex lattice method

α	angle of attack
β	pitch
ε	axial strain
ε_w	deflection error
η	convergence bound
γ	axial strain
κ	curvature
λ	tip speed ratio
λ_i	eigenvalue
λ_k	wave number
μ	doublet strength
ν	dynamic viscosity
ν_s	Poisson's ratio
ω	angular velocity
ω_n	natural frequency
ϕ	RBF
ρ	density
σ	source strength
θ	azimuth
ξ	relaxation parameter
Γ	circulation strength
Λ	taper ratio
Φ	velocity potential
a_m	doublet coefficient
b_m	source coefficient
c	chord
c_{f_m}	panel force coefficient
c_{p_m}	panel pressure coefficient
d	airfoil thickness
f	force
l	beam length
p	pressure
r	relative distance

s	span length
t	time
q	lift distribution
w	displacement
x, y, z	spatial coordinates
A	section area
A_R	rotor area
C_D	total drag coefficient
C_d	section-wise drag coefficient
C_L	total lift coefficient
C_l	section-wise lift coefficient
C_P	power coefficient
E	Young's modulus
G	shear modules
I	area moment of inertia
L	lift
M	momentum
P	power
R	radius
S	planform area
S_m	panel area
T	torque
T_v	viscous stress tensor
$\boldsymbol{\alpha}$	LS solution vector
$\mathbf{c}_{f_m}$	force coefficient vector
$\mathbf{c}_{p_m}$	pressure coefficient vector
$\mathbf{d}$	displacement vector
$\mathbf{f}$	force vector
$\mathbf{h}$	modal force vector
$\mathbf{k}_c$	constitutive law
$\boldsymbol{\lambda}$	Lagrange multipliers
$\boldsymbol{\lambda}_v$	eigenvalue vector
$\boldsymbol{\mu}$	doublet vector
$\mathbf{n}$	normal vector
$\boldsymbol{\omega}$	rotational state vector
$\mathbf{p}$	momentum vector
$\boldsymbol{\phi}$	holonomic constraints
$\mathbf{q}$	state vector

$\mathbf{r}$	residual vector
σ	source vector
$\mathbf{u}$	inflow vector
$\mathbf{v}$	modal amplitude vector
$\boldsymbol{\varphi}$	basis modes
$\boldsymbol{\xi}$	relaxation vector
$\mathbf{x}$	spatial state vector
$\mathbf{y}$	generalised state vector
$\mathbf{A}$	source matrix
$\mathbf{B}$	doublet matrix
$\mathbf{I}$	identity matrix
$\mathbf{J}$	Jacobian matrix
$\mathbf{K}$	stiffness matrix
$\mathbf{M}$	mass matrix
$\boldsymbol{\Psi}$	modal matrix
$\mathbf{R}_v$	autocorrelation matrix
$\mathbf{R}$	reduction matrix
$\mathbf{T}$	transformation matrix
$\mathbf{V}$	residual observation matrix
$\mathbf{W}$	displacement observation matrix
$\mathbf{X}_v$	eigenvector matrix
$\mathit{Æ}$	aspect ratio
Re	Reynolds number

1

INTRODUCTION AND MOTIVATION

The demand for energy from renewable sources has grown in the past years in consequence of political decisions and climate change. From a scientific point of view, the field of renewable energy is still unexploited. In contrast, the share of sources of renewable energy is planned to be extended up to 27% in Europe in the year 2030 [Eur14] and up to 86% in Germany in 2050 [Sac11]. This includes a significant amount of energy from water and wind in the offshore area [Pre12].

The present energy mix implies that the goal is reachable but there is still a long way to go. In the year 2014 the share of energy from renewable sources in Germany was 26.2%, thereof 34.8% generated by wind power [Bun14]. The turnover of wind energy systems in Germany was €9.7 billion [Sta14] revealing the impact of this market.

The intention to reach the energy goals is accompanied by the European union releasing a framework programme called Horizon 2020 [Eur15] to face current energy problems. The focus is to increase the efficiency of consumers and develop available and renewable energy sources.

The harvesting of renewable energies often includes energy converters with a high degree of complexity. Along with this complexity the demands on design tools, which can numerically simulate these energy converters, increase. The design tools need to serve two major tasks: the *development of viable energy converters* for complex sources of energy, such as waves, and *optimisation of power outcome*.

The latter task reaches the limits of available tools in terms of flexibility. Projects like the wave flap [Whi+07] contain highly unsteady boundary conditions and flow regimes. In these so-called oscillating wave surge converters (OWSCs), the power take-off (PTO) device is subjected to a constant change of flow direction. The same holds true for oscillating water column (OWC) devices. Here, a turbine transforms a constantly changing airflow into rotational energy.

The second task, namely the optimisation of energy converters restricts the permissible computing effort of the simulation. A study of parameters with several simulations is cost intensive in both time and hardware. Thus, a robust simulation method with low computational effort is requested. The benefit of optimisation in turbine design is potentially large. With an iteratively optimised pitch motion the power outcome of a vertical-axis turbine in [PAH15] is raised by up to 50% compared to a fixed pitched turbine. Due to this higher power output the turbine concept can compete the with widely-used horizontal-axis wind turbines (HAWTs). Although, the study emphasise the demand on adapted simulation methods.

Beside the pure increase in power outcome, mechanical loads on a turbine must be taken into account, especially against the background of its life span. In terms of pitch control of a HAWT a trade-off between mechanical loads and power output must be balanced [Bos03]. By resolving mechanical loads in more detail, the life span can be prolonged and the overall efficiency is increased.

Related to the percentage of renewable energy in the market, the increase of efficiency of current turbines and the development of new energy converters represent a large potential, both economical and environmental.

This thesis is initiated by tasks in the field of wind and water turbine design. These turbines convert energy of a moving fluid into mechanical energy with a set of lifting bodies, namely blades. The task is to *accurately simulate the complete behaviour* of a turbine in a *generic formulation*. This thesis is focused on the vertical-axis turbine. Two types of turbines will be differentiated, the vertical-axis wind turbine (VAWT) and the vertical-axis tidal turbine (VATT) in a water domain.

The dynamics of a turbine are determined by the fluid and the mechanical side. For both sides, a well adapted numerical solver needs to be chosen and implemented.

The fluid side will be described with an actuator-line method (ALM) representing a lifting body with a line of actuators. The ALM is implemented by Wenzel in his thesis [Wen15]. The surrounding fluid is resolved with a Reynolds-averaged Navier-Stokes (RANS) approach in the OpenFOAM framework.

The motion of the body will be captured with a multi-body system (MBS) solver. It enables a generic formulation and includes elastic dynamics of bodies. The dynamics are represented by a modal decomposition. In order to reduce the size of the used model and the computational effort, a model order reduction (MOR) will be equipped.

The coupling of fluid and mechanical side requires an approach to so-called fluid-structure interaction (FSI). A FSI defines the influence of the fluid on the body and vice versa. It occurs in many technical applications, but in different scales, which can be distinct into weak and strong FSI. In strong FSI, the density of fluid and solid are of the same magnitude, as for a VATT.

For the simulation of a strongly coupled configuration the information between the states on each domain has to be exchanged simultaneously. This is commonly accomplished by a partitioned or a monolithic approach. In the partitioned approach the solver on each domain is called separately and the information are exchanged iteratively. In this thesis the focus lies on the partitioned approach.

The convergence of the iterations in the partitioned approach will be accelerated with adaptive methods to reduce the simulation time.

In order to allow an accurate statement concerning the power outcome of a turbine, the used solvers and approaches will be validated with available results. A consistent validation implies the separate examination of fluid and mechanical side, but also of the coupling of both solvers and the dynamic response of the FSI. The results of the simulations will be compared to experimental results and analytic solutions. This includes aerodynamic and mechanical properties of a wing in a parallel inflow as well as quasi-steady and dynamic results of a vertical-axis turbine.

In the first part of this thesis, the task will be presented and the choice of solvers will be described. In the following chapters MOR techniques will be examined. Subsequently, the MBS solver and an interface node mapping will be depicted. The used fluid solver with the ALM will be outlined and further approaches to lifting bodies and vertical-axis turbines are listed. The chapter on FSI describes the distinct coupling methods and accelerations of convergence. After the introduction of the simulation methods, a validation takes place on different stages. Finally, an advanced application of the depicted methods in a simulation is performed. The blade deflection of a VATT will be computed and analysed.

In the last chapter, the results of this thesis will be summarised and discussed. Conclusions will be drawn on the developed methods and possible future works proposed.

CENTRAL TASK AND CHOICE OF SOLVERS

This work intends to accomplish the simulation task in a turbine design process. The prerequisites for the simulation are to accurately simulate turbines and all their dynamics within a feasible computational time. The dynamics include unsteady fluid loads demanding a detailed rendering of the turbine mechanics.

The requirement of an efficient simulation leads to a certain choice of methods for both fluid and body dynamics. In terms of FSI a fast coupling scheme is needed as well.

For the field of turbine simulation a choice of suitable solvers is considered. A common approach in the field of HAWTs is the ALM [SS02]. The ALM offers a computational efficient simulation of lifting-body devices including a detailed representation of their wakes. In addition, it provides a high flexibility for body motion suiting a generic approach of body dynamics.

The ALM is integrated in a computational fluid dynamics (CFD) toolbox called open source field operation and manipulation (OpenFOAM). The advantage over other software is its functional extent and open source code.

A generic representation of body motion is summarized in the field of MBSs. For the application on turbines, however, not only the rigid body motion is utilised, but the subregion of flexible multi-body motion. By this, a complete turbine motion can be rendered including the deflection of blades or supporting structures like a tower. Elastic structures can be represented by a model of their dynamics. This can be simple elements like beams or a reduced model of their entire dynamics.

For the latter task the concept of MOR can be applied. It enables the capture of complex dynamics with fewer system states and thus less computational cost.

Starting from a complex model, the model reduction condenses the dynamics into the relevant parts for the given problem. In terms of body motion this usually implies a finite-element method (FEM) analysis of a component part, which is then reduced to a subset of its degrees of freedom (DOFs) and eigenmodes.

The system matrices of a reduced model are integrated in the multi-body solver and this way aspects of both a rigid body motion and elasticity is covered.

In order to capture the entire dynamic of a turbine, both fluid side and mechanical model have to be connected. This interaction of solvers and models requires a definition of interfaces and their management, which is outlined in Figure 1.1. The interaction between fluid and mechanical solver will be detailed in Chapter 5. The transfer from a FEM analysis towards a reduced model for the MBS solver is handled by the MOR. As a preprocessing for the multi-body software a modal analysis is applied to the reduced models.

For the interface between fluid and mechanical domain a choice of interface nodes is required. Concerning the ALM the nodes on the fluid side are fewer than the nodes of the MOR. In Chapter 2 a mapping of interface nodes is defined enabling the transfer of forces from fluid nodes to mechanical nodes and body positions in the opposite direction.

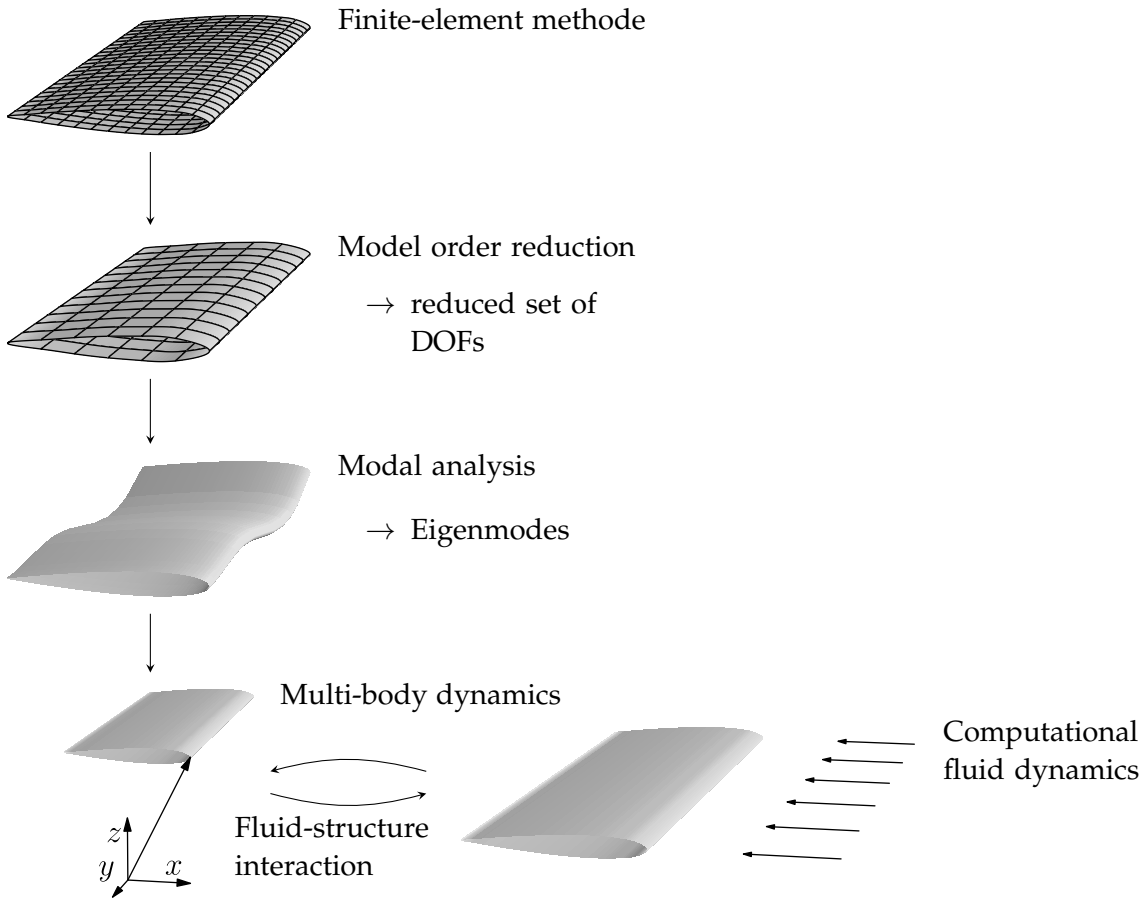

Figure 1.1.: Schematic flow of information between the engaged methods and solvers in FSI tool chain. Last section represents coupling between mechanical and fluid solver.

2

MODEL ORDER REDUCTION

The MOR provides a tool to reduce the complexity of a dynamic system and thereby lower computational time. The order of a model is defined by its number of DOFs and is lower in the *target system* than the *source system*. As a result, the reduced system is less comprehensive than the original system.

This leads to the requirement of suitable reduction processes. The aim is to obtain appropriate system dynamics of the reduced system by modifying the system matrices. At first, unneeded or DOFs with less influence on the system behaviour are neglected. A new system with the reduced set of DOFs is computed by condensing the full system matrices. The optimum is reached, when the system dynamics of interest are the same in the reduced as in the full model.

The system dynamics for a mechanical system can be modelled by a finite-element (FE) analysis. For an undamped system the equation of an elastic body motion is:

$$\mathbf{M}\ddot{\mathbf{x}} + \mathbf{K}\mathbf{x} = \mathbf{f}\,, \tag{2.1}$$

where $\mathbf{M}$ is the mass matrix, $\mathbf{K}$ the stiffness matrix, $\mathbf{f}$ the force vector and vector $\mathbf{x}$ containing all system states. For modelling of a viscoelastic body a further damping term is inserted.

2.1 FINITE-ELEMENT ANALYSIS

The system matrices and corresponding natural frequencies and eigenmodes for a given body are computed using a FEM for mechanic problems. For these tasks the open-source FEM tool GetFEM++ is convenient [Ren14].

Problem-dependent different element types may suit the problem. For the given example of a straight wing, n-th order prism elements are used [Ren14]. The belonging mesh can be easily generated from extruding a triangular meshed airfoil cross-sectional area, displayed in Figure 2.1.

The resulting 3D mesh is presented in Figure 2.2 as well as an eigenmode of the solved system.

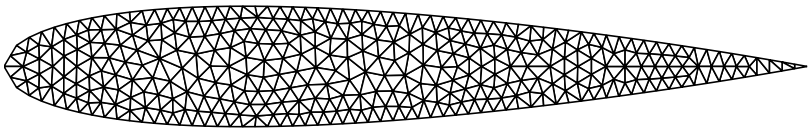

Figure 2.1.: Tetrahedral mesh of an airfoil section with NACA0015 profile.

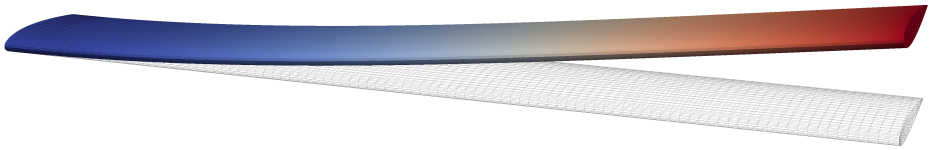

Figure 2.2.: Qualitative visualisation of first eigenmode of wing. Magnitude of deflection coloured increasingly from blue to red. Neutral position of wing displayed with mesh.

Mounted nodes

In a technical application, parts of the wing are connected to other components. In case of a clamped wing some nodes are fixed to a mount. To account for this in a FEM analysis the fixed nodes can be handled in two different ways: either they are neglected in the system matrices or their stiffness is increased by a penalty function.

The benefit of the penalty function is, that no extra transformation of the system matrices is needed both before and after the MOR. However, the choice of the penalty value has a large influence and needs to be set by the user. The advantage of row and column cancellation for neglected nodes is a lower influence on resulting eigenvalues of the system. The drawback is a higher computational effort for the matrix manipulation of large systems.

In this work cancellation is used, since the system size is manageable and the focus is on correct eigenvalues against the background of MOR.

2.2 MODEL ORDER REDUCTION TECHNIQUES

Common reduction techniques are the Guyan reduction and derivatives, modal reductions, two-step and multi-step methods. The Guyan reduction was initially published by [Guy65] and is an example for single-step methods. Modal reduction bases on a preliminary modal decomposition and uses only modal parameters for input such as the system equivalent reduction expansion process (SEREP) reduction [OAR89]. The iterative meth-

ods commonly start from a single-step method like Guyan reduction and proceed with a correcting step.

The advantage of single-step methods is to solve the task in only one system of equations, which however may need the handle of large matrices and leads to larger computational costs. In iterative methods the computational time is adaptive to the degree of accuracy.

In [Qu04] several reduction processes are analysed and compared. The Guyan reduction and the improved reduced system (IRS) are depicted and applied to the wing in this setup.

In the first step of a reduction process the DOFs are separated into n master and m slave degrees. The slave DOFs will be deleted in the process of the reduction. The master degrees remain and will contain all necessary information to represent the significant system properties.

The nomenclature is presented in Equation (2.2) for a dynamic system.

$$\begin{bmatrix} \mathbf{M}_{mm} & \mathbf{M}_{ms} \\ \mathbf{M}_{sm} & \mathbf{M}_{ss} \end{bmatrix} \begin{bmatrix} \ddot{\mathbf{x}}_m \\ \ddot{\mathbf{x}}_s \end{bmatrix} + \begin{bmatrix} \mathbf{K}_{mm} & \mathbf{K}_{ms} \\ \mathbf{K}_{sm} & \mathbf{K}_{ss} \end{bmatrix} \begin{bmatrix} \mathbf{x}_m \\ \mathbf{x}_s \end{bmatrix} = \begin{bmatrix} \mathbf{f}_m \\ \mathbf{f}_s \end{bmatrix} \tag{2.2}$$

This leads to the equation for the slave nodes in dependency of the full system,

$$\mathbf{x}_s = -\mathbf{K}_{ss}^{-1} \left(\mathbf{M}_{sm} \ddot{\mathbf{x}}_m + \mathbf{M}_{ss} \ddot{\mathbf{x}}_s + \mathbf{K}_{sm} \mathbf{x}_m \right) , \tag{2.3}$$

see [YQ00].

The outcome of a reduction calculation is a transformation matrix $\mathbf{T}$, which is applied on all system matrices.

$$\mathbf{M}_r = \mathbf{T}^T \mathbf{M} \mathbf{T} \tag{2.4}$$

$$\mathbf{K}_r = \mathbf{T}^T \mathbf{K} \mathbf{T} \tag{2.5}$$

$$\mathbf{F}_r = \mathbf{T}^T \mathbf{F} \tag{2.6}$$

From the sorting of the master and slave nodes results the assembly of the transformation matrix. It holds a unity matrix $\mathbf{I}$ for the remaining master nodes and a reduction matrix $\mathbf{R}$.

$$\mathbf{T} = \begin{bmatrix} \mathbf{I} \\ \mathbf{R} \end{bmatrix} \tag{2.7}$$

Another reduction concept, the hybrid reduction, additionally contains modal coordinates, which are not connected to physical nodes. A modal reduction is not applied in this work, but leads to similar resulting reduced systems, such as the SEREP reduction.

In terms of eigenvalues a modal reduction is exact. However, a major drawback of most implementations of modal reductions is the necessity of (pseudo) inverse computation leading potentially to badly conditioned reduced matrices.

All referred methods have in common, that they end in non-sparsely populated system matrices. In [KB07a] and [KB07b] a Krylov subspace based method is used preserving a sparse structure of the system matrix. Since the reduced matrices proceed into a modal analysis in this work, sparse matrices are not necessary.

2.2.1 *Guyan reduction*

The Guyan reduction yields good results, if applied to a static excitation in terms of a FE model. However, looking at the dynamic response this method fails, i.e. the eigenmodes are not preserved during the reduction process.

The reduced matrices $\mathbf{M}_G$, $\mathbf{K}_G$ and vector $\mathbf{f}_G$ are computed with the reduction matrix $\mathbf{R}_G$, which is computed by

$$\mathbf{R}_G = -\mathbf{K}_{ss}^{-1}\mathbf{K}_{sm}\,, \tag{2.8}$$

and defines the transformation between master and slave nodes

$$\mathbf{x}_s = \mathbf{R}_G\mathbf{x}_m\,, \tag{2.9}$$

formulated by [Quo4].

2.2.2 *Improved reduced system*

The IRS extends the Guyan reduction by accounting for the inertia effects of the reduction approach in Equation (2.3).

Relating the master and slave states and their derivatives to the definition of Guyan leads to the statement

$$\ddot{\mathbf{x}}_s = -\mathbf{R}_G\mathbf{M}_G^{-1}\mathbf{K}_G\mathbf{x}_m\,. \tag{2.10}$$

This leads to the reduction matrix

$$\mathbf{R}_{IRS} = \mathbf{K}_{ss}^{-1}\left[\left(\mathbf{M}_{sm} + \mathbf{M}_{ss}\mathbf{R}_G\right)\mathbf{M}_G^{-1}\mathbf{K}_G\right] + \mathbf{R}_G\,, \tag{2.11}$$

developed by [YQoo].

2.3 VALIDATION OF THE REDUCED MODEL

The specified methods will be validated on a loaded wing with a NACA-type aerofoil section. These section are defined by a work of the national advisory committee for aeronautics (NACA), see [ADS45]. For the NACA-ooxx series the section distribution can be defined as a function, see appendix A.1.

In this section a solid wing with parameters listed in Table 2.1 is analysed. Numerical results are compared to analytic solutions.

Table 2.1.: Geometric parameters and material properties of solid wing for MOR.

aerofoil section	NACA0015
span size	$s = 1.2\,\mathrm{m}$
chord length	$c = 0.185\,\mathrm{m}$
material	aluminium
Young's modulus	$6.90 \cdot 10^{10}\,\mathrm{N\,m^{-2}}$
density	$\rho_s = 2700\,\frac{\mathrm{kg}}{\mathrm{m}^3}$
Poisson's ratio	$\nu_s = 0.32$

The used FE model consists of 31k DOFs and will be reduced to 600 master DOFs, which leads to a reduction in system size of 98%.

The wing is loaded on the tip and the flap-wise deflection of the wing measured. The static answer of a single load can be analytically determined by the beam theory for small deflections, i.e. bending of an Euler-Bernoulli beam. For a beam clamped on one side the maximum displacement states as

$$w_{max} = \frac{f l^3}{3EI}\,, \tag{2.12}$$

with force f, length $l = s$, Young's modulus E and area moment of inertia I.

The natural frequencies of a beam clamped on one side are determined by the transient form of the beam equation, derived from the Timoshenko beam theory. The solution yields

$$0 = \cos(\lambda_k) \cdot \cosh(\lambda_k) + 1\,, \tag{2.13}$$

with the k-th wave number λ_k. The natural frequencies for the wing are

$$\omega_{n,k} = \sqrt{\frac{\lambda_k^4 EI}{l^4 \rho_s A}}, \tag{2.14}$$

with the section area A.

The results of the analytic solution, the FEM and the reduced models are listed in Table 2.2. It shows the static deflection and the frequencies of the first nine eigenmodes. For the static case a force is applied at the tip point of the wing and the deflection is measured. The error of the FEM results is related to the analytic solution. Furthermore, the error of the reduction method is related to the FEM results, since the response of a reduced system can only be as accurate as of the full system.

The deflection response of a static load is computed with following formulas.

$$\mathbf{d}_{FEM} = \mathbf{K}^{-1}\mathbf{f} \tag{2.15}$$

$$\mathbf{d}_r = \mathbf{K}_r^{-1}\mathbf{f}_r\,, \tag{2.16}$$

where $\mathbf{K}_r$ is the reduced stiffness matrix and $\mathbf{f}_r$ the reduced force vector.

Table 2.2.: Comparison of relative error of static deflection and flap-wise modes to analytic solution for FEM and different reduction methods. First nine modes of analysed wing are listed. Error of reduction methods is related to FE model.

method:	analytical	FEM	Guyan	IRS
static defl.	0.0539[m]	0.00629%	-0.000197%	-0.000246%
natural frequency ω_n [Hz]				
1st	12.906	1.589%	$2.59 \cdot 10^{-4}$%	$1.68 \cdot 10^{-8}$%
2nd	80.880	1.440%	0.0102%	$1.03 \cdot 10^{-9}$%
3rd	226.466	1.208%	0.0793%	$5.36 \cdot 10^{-10}$%
4th	443.783	0.875%	0.302%	$2.7 \cdot 10^{-8}$%
5th	733.605	0.446%	0.816%	$5.33 \cdot 10^{-7}$%
6th	1095.879	-0.078%	1.79%	$5.69 \cdot 10^{-6}$%
7th	1530.608	-0.695%	1.983073%	$6.4 \cdot 10^{-6}$%
8th	2037.791	-1.404%	3.420341%	$4.01 \cdot 10^{-5}$%
9th	2617.430	-2.204%	5.886580%	0.000209%

2.4 MODAL ANALYSIS

Both the FEM model and the reduced model are analysed in their modal properties. This is executed by an eigenanalysis of the system matrices and results in eigenmodes of the system representing the characteristic shapes of an elastic part.

The eigenvalue problem for the FEM models states as

$$\mathbf{K}\mathbf{X}_v = \boldsymbol{\lambda}_v \mathbf{M}\mathbf{X}_v\,, \tag{2.17}$$

with the eigenvector matrix $\mathbf{X}_v \in \mathbb{R}^{n\times n}$ and the eigenvalues in vector $\boldsymbol{\lambda}_v \in \mathbb{R}^n$. At this application only the lowest modes are of interest. Additionally, the system matrices are sparse, thus Arnoldi iterations are used to compute the eigenvalues and eigenvectors.

The resulting matrices of an eigenanalysis are input for flexible body dynamics in the MBS solver, q.v. [FE10] and [LE07]. The first four eigenmodes of the given wing are illustrated in Figure 2.3.

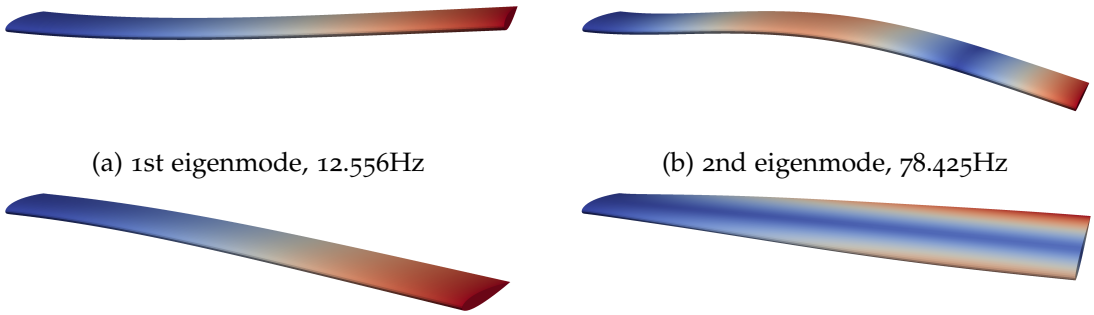

(a) 1st eigenmode, 12.556Hz

(b) 2nd eigenmode, 78.425Hz

(c) 3rd eigenmode, 83.792Hz

(d) 4th eigenmode, 201.414Hz

Figure 2.3.: Qualitative visualisation of first four eigenmodes of wing. Magnitude of deflection coloured increasingly from blue to red. Frequencies sorted increasingly from Figure (a) to (d).

Besides the eigenmodes the modal mass and stiffness matrices are required by the MBS solver. They will be assembled from the reduced system matrices and a selected set of k eigenvectors $\mathbf{X}_v \in \mathbb{R}^{n \times k}$ of the (reduced) system,

$$\mathbf{M}_v = \mathbf{X}_v^T \mathbf{M} \mathbf{X}_v \tag{2.18}$$

$$\mathbf{K}_v = \mathbf{X}_v^T \mathbf{K} \mathbf{X}_v \,, \tag{2.19}$$

or for the reduced system $\mathbf{X}_{v,r} \in \mathbb{R}^{m \times k}$.

In this chapter suitable reduction techniques for the simulation task are depicted and validated. The IRS shows sufficient accuracy in terms of eigenmodes of the FEM analysed wing, all with a low amount of user interaction.

Furthermore, the modal matrices for the MBS solver are prepared.

3 MULTI-BODY SYSTEM

With the MBS approach a framework is provided to solve dynamics of bodies, which are exposed to external forces. Several implementations of a MBS library are available providing fast computation of body motion in generic formulation, such as: MSC Adams, Neweul-M^2, Robotran, Simpack, compare [SE12]. A MBS approach includes a well-arranged choice of reference frames and flexible body dynamics, either by flexible elements or reduced bodies from MOR (Chapter 2).

As an alternative to a MBS solver, a mechanical solver with FEs could be taken into account. The drawbacks of the FEM are a potentially higher computational time and the need of an additional rigid body motion framework. The latter is accomplished with a six DOF solver, which then handles one individual body only. Furthermore, extended constraints of rigid body motion and interaction of multiple bodies cannot be covered by a six DOF solver directly.

The MBDyn-suite developed at the Politecnico di Milano [MMM14] provides a MBS solver including flexible body dynamics. Furthermore, it offers a robust and open source implementation, already used in FSI application [CMQ09]; [CMQ11]; [Ben+11]; [MS11]; [YLV07]. MBDyn is used as mechanical solver in this work.

3.1 STRUCTURE OF MULTI-BODY SYSTEMS

For transient problems, i.e. time progression of multi-body dynamics, two types of solvers are distinguished: forward and inverse dynamics. The forward dynamics, which are used in this work, return the body position and state at a certain time after applying forces. In opposition to this, the inverse dynamics receives a position of a body and returns the forces needed to bring the body into this position at the requested time step [RS88]. A brief derivation of multi-body equations is presented in the following section.

To begin with, the position and orientation of a rigid body are defined by its state vector $\mathbf{x}$. Velocity variables are stored in $\dot{\mathbf{x}}$.

In terms of equation of motion, unreduced kinematic equations and state space representation are distinguished. Both can be derived from Newton-Euler equations.

The unreduced and unconstrained kinematic equation of motion yields

$$\mathbf{M}(\mathbf{x})\,\ddot{\mathbf{x}} = \mathbf{f}(\mathbf{x}, \dot{\mathbf{x}}, t)\,. \tag{3.1}$$

A state space representation is formulated as

$$\mathbf{M}_\mathbf{y}\dot{\mathbf{y}} = \mathbf{h}_\mathbf{y}\,, \tag{3.2}$$

with the state variables $\mathbf{y}$ containing the generalised coordinates. The number of DOFs is $n_f = n_z - n_c$, where n_z are all DOFs of $\mathbf{x}$ and n_c the constrained ones. In this derivation the unreduced equations will be used.

For constrained systems further equations are defined [SE12]. For holonomic constraints the implicit formulation yields

$$\boldsymbol{\phi}(\mathbf{x}, t) = \mathbf{0} \tag{3.3}$$

and the explicit formulation

$$\mathbf{x} = \mathbf{x}(\mathbf{y}, t)\,. \tag{3.4}$$

Introducing the state vector $\mathbf{q} = \begin{bmatrix}\mathbf{x}\\ \dot{\mathbf{x}}\end{bmatrix}$ and the momentum vector $\mathbf{p}$, the equation of motion are derived as a first-order system of equations,

$$\mathbf{M}\dot{\mathbf{q}} = \mathbf{p} \tag{3.5}$$

$$\dot{\mathbf{p}} = \mathbf{f}(\mathbf{q}, \dot{\mathbf{q}}, t)\,. \tag{3.6}$$

The constraints in Equation (3.3) are added to the equations of motion (3.5) and (3.6) by Lagrange multipliers [CMQ09]. The resulting constrained equations of motion are

$$\mathbf{M}\dot{\mathbf{q}} = \mathbf{p} \tag{3.7}$$

$$\dot{\mathbf{p}} + \boldsymbol{\phi}_\mathbf{q}^T\boldsymbol{\lambda} = \mathbf{f}(\mathbf{q}, \dot{\mathbf{q}}, t) \tag{3.8}$$

$$\boldsymbol{\phi}(\mathbf{q}, t) = \mathbf{0}\,. \tag{3.9}$$

These equations are combined in a residual function $\mathbf{r}(\mathbf{q}, \dot{\mathbf{q}}, t)$ [MMM14].

3.2 TRANSIENT SOLVER

Considering the implementation used in this work, the transient simulation of a MBS splits into two parts. The first part is the computation of the initial derivative, defined as an initial value problem. The second part is the regular solution phase, in which a Newton-Raphson method is applied, see appendix B.1. The initial value problem is stated as a differential-algebraic equation (DAE),

$$\mathbf{r}(\mathbf{q}, \dot{\mathbf{q}}, t) = \mathbf{0}. \tag{3.10}$$

After the computation of the derivatives, an implicit integration scheme is applied. For this, Equation (3.10) needs to be solved for $\dot{\mathbf{q}}$, which is computed with a Newton-Raphson method,

$$\mathbf{r}_{\dot{\mathbf{q}}} \partial \dot{\mathbf{q}}_k = -\mathbf{r}\,, \tag{3.11}$$

where $\mathbf{r}_{\dot{\mathbf{q}}} = \mathbf{J}_{\dot{\mathbf{q}}} = \frac{\partial \mathbf{r}}{\partial \dot{\mathbf{q}}}$ is the Jacobian matrix of $\mathbf{r}$ with respect to $\dot{\mathbf{q}}$. The index k defines the current convergence step of the integration scheme. [MMM14]

3.3 FLEXIBLE BODIES

The MBS solver MBDyn offers the feature to include a flexible body. Due to the definition by its modal shapes, it is declared as modal body. This body can be build from a reduced model or can potentially contain a full FE model.

The integration of flexible bodies in a multi-body framework is mentioned, amongst others by [Wal91], later depicted in [Wal94] and reviewed by [Sha97].

The state, in terms of deformation, of the flexible body is captured with the modal amplitude vector $\mathbf{v} \in \mathbb{R}^{n_v}$. The node position of the discretised body is thus

$$\tilde{\mathbf{x}}(t) = \mathbf{\Psi}\mathbf{v}\,, \tag{3.12}$$

with the modal matrix $\mathbf{\Psi} \in \mathbb{R}^{3\times n_v}$.

The equations of motion of a flexible body are derived from the principle of virtual work. Equation (3.1) and (3.5), respectively, are rearranged to

$$\begin{bmatrix} \mathbf{M}_{xx} & \mathbf{M}_{x\theta} & \mathbf{M}_{xv} \\ & \mathbf{M}_{\theta\theta} & \mathbf{M}_{\theta v} \\ & & \mathbf{M}_{vv} \end{bmatrix} \begin{bmatrix} \ddot{\mathbf{x}} \\ \dot{\boldsymbol{\omega}} \\ \ddot{\mathbf{v}} \end{bmatrix} + \begin{bmatrix} \mathbf{0} \\ \mathbf{0} \\ \mathbf{K}_{vv} \end{bmatrix} \mathbf{v} + \mathbf{k}_\omega(\boldsymbol{\omega}, \mathbf{v}, \dot{\mathbf{v}}) = \mathbf{h}\,. \tag{3.13}$$

Hereby $\mathbf{x}$ holds only the displacement and $\boldsymbol{\omega}$ is the vector of rotational states. The mass matrix on the left-hand side contains the coupling terms $\mathbf{M}_{xv}$ and $\mathbf{M}_{\theta v}$ between rigid and flexible states, approximated with Taylor series. The matrix $\mathbf{M}_{vv}$ and $\mathbf{K}_{vv}$ holds the modal mass and stiffness. The vector $\mathbf{k}_\omega$ accounts for gyroscopic and centrifugal forces. The forces vector $\mathbf{h}$ is derived from the generalised force vector $\mathbf{p}$ complemented with the internal forces $\mathbf{f}_v$. [CMQ09]

Validation

For the case of a wing clamped on one side, the deflection of a tip loaded, flexible body is measured in the MBS solver and compared to the analytic solution, which is defined in Section 2.3. Parameters of the setup are listed in Table 6.1 and further mechanical

quantities in Table 3.2. The relative error is defined as $\varepsilon_w = \frac{w - w_{model}}{w}$, where w_{model} is the deflection of the analysed model and w the reference.

The reduced model of 156 DOFs is condensed from a full FE model with 8112 DOFs. Only the flap-wise modes are taken into account. The error of the reduced body in MBDyn is 2.87% with respect to the full model. When using more modes, the error may increase to 5.27%. Inconsistently with the results from Section 2, the static deflection within the multi-body solver differs (see Table 3.1). This is probably caused by a noisy force $\mathbf{f}$ in contrast to the reduced force vector $\mathbf{f}_r$. Nearby modes are excited in the simulation, which is affirmed in the output of the simulation. These nearby modes may lead to a false deflection for the tip loaded wing.

Concerning the application in the FSI, this phenomenon has minor influence, because the force distribution is less scattered and every mode relevant.

Table 3.1.: Error of static deflection of tip loaded wing with respect to analytic solution. Error of reduced and modal model is related to full FE model.

model	DOF	ε_w	
full	8112	0.0641	%
reduced	156	$-4.69 \cdot 10^{-6}$	%
modal		2.87	%

3.4 BEAM MODEL

Besides reduced models, an approach using beam elements is suitable for turbine related problems. For straight-bladed or shaped wings in a discretised approach, the mechanic properties can be represented section-wise using beam elements. This suits an engineering approach, where blade properties are commonly offered as section-wise listings.

The used beams are finite elements of higher order, which allow bending and twisting of a slender structure in a model context.

The MBDyn framework offers two- and three-noded beam elements. The properties of a specific part, in this work a wing, are mapped to the beam element with a constitutive law. It is defined in a 6D-matrix containing the mechanical properties as follows,

$$\begin{bmatrix} f_x \\ f_y \\ f_z \\ M_x \\ M_y \\ M_z \end{bmatrix} = \mathbf{f} \left(\begin{bmatrix} \varepsilon_x \\ \gamma_y \\ \gamma_z \\ \kappa_x \\ \kappa_y \\ \kappa_z \end{bmatrix}, \begin{bmatrix} \dot{\varepsilon}_x \\ \dot{\gamma}_y \\ \dot{\gamma}_z \\ \dot{\kappa}_x \\ \dot{\kappa}_y \\ \dot{\kappa}_z \end{bmatrix} \right) . \tag{3.14}$$

Hereby, x is the direction along the wing, f_x is the axial force, f_y, f_z are the shear forces, M_x the torsional moment, M_y, M_z the bending moments, ε_x the axial strain, γ_y, γ_z the shear strain, κ_x torsional curvature, κ_y, κ_z bending curvature (see MBDyn manual [Mas13] for detailed definitions).

The function $\mathbf{f}$ is dependent on the constitutive law $\mathbf{k}_c$, which contains

$$\mathbf{k}_c = \begin{bmatrix} EA_x \\ GA_y \\ GA_z \\ GI_p \\ EI_y \\ EI_z \end{bmatrix} , \tag{3.15}$$

where E is the Young's modulus, G the shear modulus, A_x the airfoil section area and A_y and A_z the corrected shear area (compare [GW01]). The area moments of inertia for y and z direction are I_y and I_z, whereas the polar moment around the x-axis is defined as

$$I_p = I_y + I_z. \tag{3.16}$$

Applying this element, a wing can be discretised with N independent elements, which are connected in a chain with $N + 1$ nodes.

3.4.1 *Validation*

The beam elements are applied according to the setup in Table 3.2 and the deflection is compared to the analytic solution.

The area moments of inertia are determined from a numerical summation of the polygonal airfoil section of the wing. The discrete formulation of appendix C.1 states

$$I_x = \frac{1}{12} \sum_i (y_i^2 + y_i y_{i+1} + y_{i+1}^2)(x_i y_{i+1} - x_{i+1} y_i) \tag{3.17}$$

$$I_y = \frac{1}{12} \sum_i (x_i^2 + x_i x_{i+1} + x_{i+1}^2)(x_i y_{i+1} - x_{i+1} y_i) , \tag{3.18}$$

compare [Som14].

For an increasing number of elements the error stays sufficiently low, as depicted in Figure 3.1. The three-noded beams provide a more accurate solution with fewer elements compared to the two-noded beams. This can be caused by so-called shear-locking and corrected by scaling of the constitutive law. The correcting factor is internally applied to the two-noded beam in a later implementation, compare [Mas14].

Table 3.2.: Geometric parameters and material properties of solid wing for tip load examination

material	aluminium
Young's modulus	$6.90 \cdot 10^{10}\,\mathrm{N\,m^{-2}}$
density	$\rho_s = 2700\,\frac{\mathrm{kg}}{\mathrm{m}^3}$
Poisson's ratio	$\nu_s = 0.32$
area moment of inertia	$I_z = 9.5320 \cdot 10^{-6}\,\mathrm{m}^4$
	$I_y = 0.0017\,\mathrm{m}^4$
section area	$A = 0.0274\,\mathrm{m}^2$
force	$10^5\,\mathrm{N}$

3.4.2 *Interface node mapping*

Depending on the source of external forces, the nodes of the discretised body usually do not match with the nodes of the forces. In order to connect the position and velocity of the body with the forces, a valid mapping of interface nodes for both directions needs to be defined.

In this work two possible mappings are used, one to connect a set of surface forces with a volumetric body and another to distribute the state of a single node to a slice of a slender body, namely a wing. The former is applied when a surfaces-based code is employed for the fluid forces and a reduced body on the mechanical side. The latter is relevant for the ALM and a reduced body, where the ALM consists of a line of single nodes. For beam elements in connection with the ALM, it is appropriate to space the beam element nodes according to the nodes of the actuator line. Thus, the nodes of both sides are concentric.

The mapping of surface nodes to a volumetric body is determined with linear interpolation between elements of the FEM. Hereby, the Ansatz functions of the underlying elements are utilised to map nodes on the fluid side to the nearby nodes on the mechanical side. The use of the Ansatz functions is possible, because the surface nodes are close to or within the elements of the discretised body. Additionally, the forces are evenly dis-

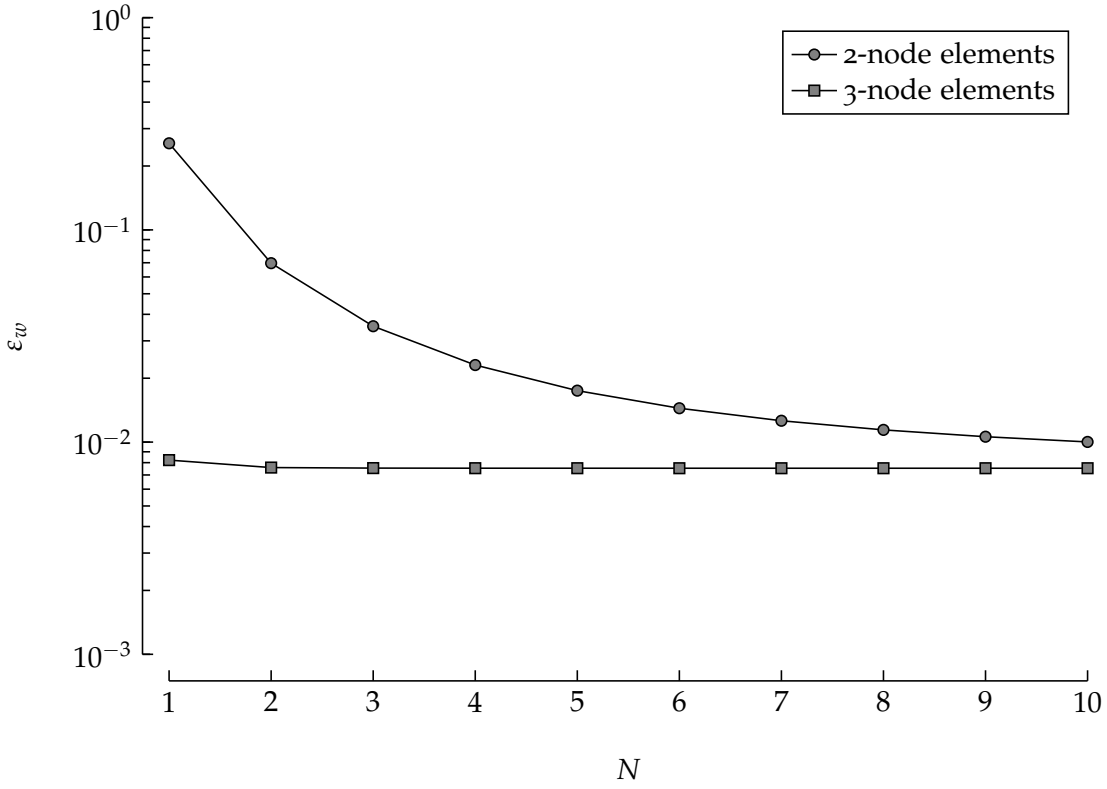

Figure 3.1.: Relative error of wing tip deflection compared to analytic solution for different beam models and increasing number of beam elements. Error is plotted on logarithmic axis.

tributed and singular loads avoided.

For the mapping of a line of nodes to a volumetric body, the interpolation between the nearest neighbour nodes leads to a discontinuous load distribution or displacements. Alternatively, the connection can be established with radial basis functions (RBFs), as implemented in MBDyn. Therefore, the interface field is marked with Γ. An accurate mapping premises that the trace of the virtual displacement of the interface nodes δd_Γ remains equal on both sides,

$$\mathrm{Tr}(\delta \mathbf{d}_{\Gamma,f}) = \mathrm{Tr}(\delta \mathbf{d}_{\Gamma,s})\,. \tag{3.19}$$

This mapping function is stated as a minimisation problem, which is solved by a weighted least squares (LS) approach,

$$\min \int_\Gamma \phi \left(\mathrm{Tr}(\delta \mathbf{d}_{\Gamma,f}) - \mathrm{Tr}(\delta \mathbf{d}_{\Gamma,s})\right)^2 dA\,, \tag{3.20}$$

compare [QMM05]. As a weighting function compact supported RBFs are used.

The used RBF of order two is formulated as a truncated power function,

$$\phi(r) = (1-r)_+^4(4r+1)\,, \tag{3.21}$$

where $r = \|\mathbf{x} - \mathbf{x}_i\|$ is the relative node distance, see [QMM05] and [Wen95].

3.4.3 *Node mapping for reduced bodies*

When handling reduced bodies in the multi-body solver, the kinematics of the master nodes need to be connected with the interface nodes. In case of the ALM, this is sufficiently specified in the prior Section 3.4.2. A direct mapping from the small set of master nodes to the line of force is defined without loss of information.

For surface based fluid code the set of interface nodes is significantly larger than the master nodes of the reduced body. Hence, the transformation matrix of the MOR needs to be used in order to restore the information of the slave nodes. Concerning the displacement this is defined in Equation (2.9) and must be extended to account for the relative motion between the reference node and the flexible nodes. By this, the position and velocity of the interfaces nodes is composed of the rigid body motion and the relative flexible body motion. In this context, the reference node holds the rigid body motion. Its position is defined as $\mathbf{x}_{O'}$. Quantities relative to the reference node are marked with the lower index *rel*.

The following equations define the absolute position of the full set of nodes in dependence on the reference node and the current state of the master nodes. The initial, unexcited states are defined using the lower index 0.

$$\Delta\mathbf{x}_m = \mathbf{x}_m(t) - \mathbf{x}_{m,0} \tag{3.22}$$

$$\Delta\mathbf{x} = \mathbf{T}\,\Delta\mathbf{x}_m \tag{3.23}$$

$$\mathbf{x} = \Delta\mathbf{x} + \mathbf{x}_0 + \mathbf{x}_{O'}\,. \tag{3.24}$$

The derivation of the node orientation is straight forward, but not relevant for the surface-based fluid solvers in this work.

The same holds true for velocities, however rotational terms must be taken into account,

$$\dot{\mathbf{x}}_{rel} = \mathbf{T}\,\dot{\mathbf{x}}_m \tag{3.25}$$

$$\dot{\mathbf{x}}_{abs} = \boldsymbol{\omega} \times \mathbf{r}_{rel} + \dot{\mathbf{x}}_{O'} \tag{3.26}$$

$$\dot{\mathbf{x}} = \dot{\mathbf{x}}_{rel} + \dot{\mathbf{x}}_{abs}\,. \tag{3.27}$$

With these equations and the mapping of surface nodes to a volumetric body (see Section 3.4.2) it is possible to derive the absolute position and velocity of a set of interfacing surface nodes from a reduced body motion.

In this chapter the MBS framework is specified and computations are applied in the MBDyn software [MMM14]. The concept of flexible bodies within a MBS is depicted, including beam elements and modal bodies on basis of order-reduced bodies. The interface between mechanical and fluid solver is prepared, which allows the exchange of forces and body kinematics.

The validation is fulfilled by the example of a wing. The static responses of both beam and modal body show sufficient agreement with the analytic results. An example of a full model for a VATT is listed in appendix C.2.

4 FLUID DYNAMICS

A solid body in a fluid environment experiences forces caused by the surrounding flow. The flow depends on the shape of the body, boundary condition of the control volume and physical parameters of the fluid. The field of numerical approaches to the flow behaviour are named computational fluid dynamics (CFD).

In this work an implementation of a model-based method for lifting devices, called actuator-line method (ALM) is utilised as CFD solver. The ALM is proposed by [SS02] for the application in wind energy. The method is integrated in the open source CFD framework OpenFOAM. An implementation of the ALM is realised by Wenzel in [Wen15] and its scheme outlined in this chapter.

4.1 OPENFOAM

The fundamental equations of fluid dynamics are stated by Navier [Nav23] and later by Stokes [Sto45]. The so-called Navier-Stokes equations contain the continuity equation

$$\frac{\partial \rho}{\partial t} + \nabla \rho \mathbf{u} = 0 \tag{4.1}$$

and the momentum equation for compressible fluids

$$\rho \left(\frac{\partial \mathbf{u}}{\partial t} + \mathbf{u}(\nabla \mathbf{u}) \right) = \rho \mathbf{f} - \nabla p + \nu \nabla^2 \mathbf{u} + \frac{\nu}{3} \nabla (\nabla \mathbf{u}) \,, \tag{4.2}$$

where ν is the dynamic viscosity, assumed to be constant. [KP01]

In the setups of this work the fluid dynamics can be reduced to incompressible flows, since effects of compressibility can be neglected for low Mach numbers.

A numerical approach to fluid dynamics is the finite volume method, which is available in the OpenFOAM [Ope14] framework, a set of solvers and tools initiated by [WT98]. With OpenFOAM the so called Reynolds-averaged Navier-Stokes (RANS) equations are solved. The RANS equation are time averaged Navier-Stokes equations, in which the averaging time span is dependent on the Reynolds number **Re**. The equations in Cartesian tensor notation with the Einstein summation convention yields

$$\frac{\partial \bar{\rho}}{\partial t} + \bar{u}_j \frac{\partial \bar{\rho}}{\partial x_j} + \bar{\rho} \frac{\partial \bar{u}_j}{\partial x_j} = 0 \tag{4.3}$$

$$\bar{\rho} \left(\frac{\partial \bar{u}_i}{\partial t} + \bar{u}_j \frac{\partial \bar{u}_i}{\partial x_j} \right) = f_i - \frac{\partial \bar{p}}{\partial x_i} + \frac{\partial T_{v,ij}}{\partial x_j} \,, \tag{4.4}$$

where $\bar{u}$ is the averaged flow and $T_{v,ij}$ is the viscous stress tensor, representing the so-called Reynolds stress. [FP12]

In order to solve the Reynolds stresses a turbulence model is used. In this thesis, the turbulence is modelled with the k-ω-SST model, a two-equation eddy-viscosity model with shear stress transport (see [Men93]; [Men94]).

The transient formulation of flow problems are solved with the PISO-SIMPLE algorithm (PIMPLE) of OpenFOAM, which is a transient solver for incompressible flows. The PIMPLE solver is a combination of the transient solver for incompressible flows (PISO) and the steady-state solver for incompressible, turbulent flows (SIMPLE).

The discretisation of the control volume is done with a rectilinear mesh with local refinement. The 3D mesh for the simulation of a VATT is exemplified in Figure 4.1.

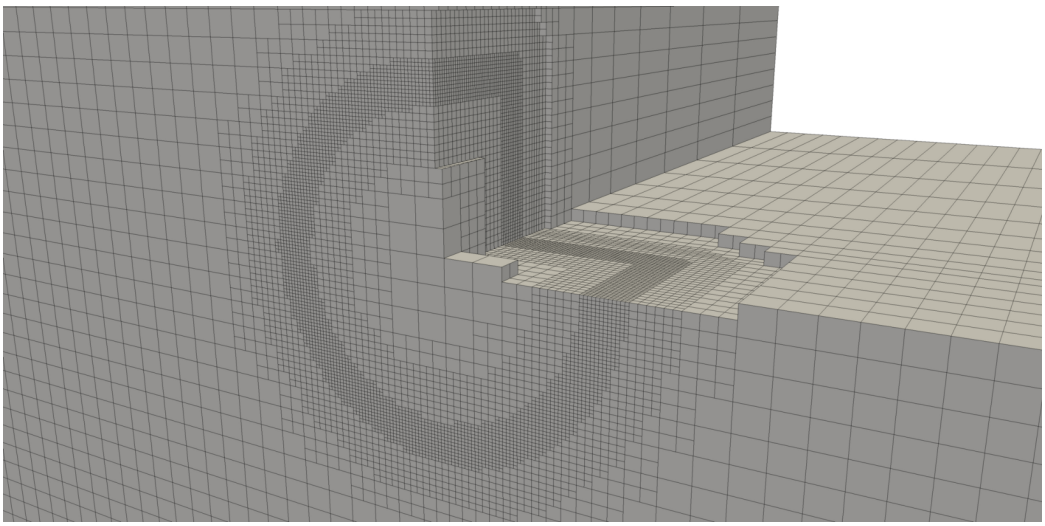

Figure 4.1.: Cutout of 3D mesh of control volume for VATT simulation. Front side is symmetry plane.

The mesh is refined at regions where the rotor of the turbine moves through the fluid. Additionally, the face at the end of the rotor is refined to observer vortex shedding at the blade tips.

4.2 LIFTING BODIES

Flow problems in application of wind or water energy can be broken down to the flow around lifting bodies, i.e. wings or blades in terms of turbines. The tower and further structural parts of a turbine can also be considered as a variant of a lifting body.

The forces on a lifting body result from the surrounding flow. To represent this circulation correctly, a detailed solution of the flow is required. This includes the resolution of boundary layers, which can be done by a sufficiently fine mesh and turbulence models. The exact solution of the boundary layer is critical for the accuracy of the computed forces [KP01].

The resulting forces of a blade are specified as lift f_L and drag f_D, whereby the lift is perpendicular to the inflow and the drag parallel as sketched in Figure 4.2. The representing dimensionless coefficients for an airfoil section are the lift coefficient C_l and the drag coefficient C_d. They are defined for an airfoil section with a chord length of c as

$$C_l = \frac{f_l}{\frac{1}{2}\rho u^2 c} \tag{4.5}$$

$$C_d = \frac{f_d}{\frac{1}{2}\rho u^2 c}, \tag{4.6}$$

where f_l is lifting force per span and f_d the drag, respectively, and ρ the density of the fluid. For the entire wing the coefficients C_L and C_D are

$$C_L = \frac{f_L}{\frac{1}{2}\rho u^2 S} \tag{4.7}$$

$$C_D = \frac{f_D}{\frac{1}{2}\rho u^2 S}, \tag{4.8}$$

with the wing planform area S.

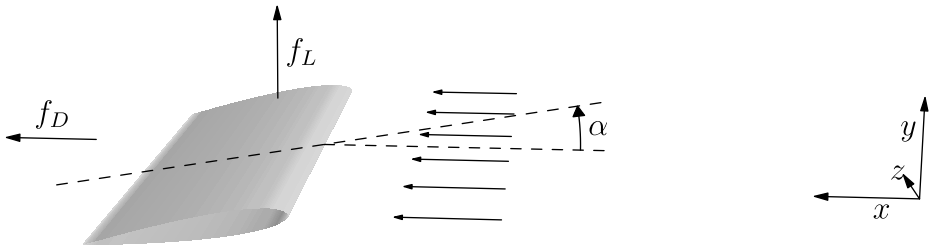

Figure 4.2.: Schematic presentation of lift and drag force acting on a wing with angle of attack for inflow in x-direction.

The angle of the inflow relative to the chord line is defined as angle of attack α. The angle of attack is composed of the angle of the inflow and the pitch β,

$$\alpha = \beta - \arctan\left(\frac{u_y}{u_x}\right), \tag{4.9}$$

in the coordinate system of Figure 4.2.

Structural parts of the turbine can also be represented with these coefficients, e.g. struts with a cylindric shape generate zero lift and a constant drag for every angle of attack. By this, the aerodynamic properties of structural parts are covered by the ALM in Section 4.3 as well.

4.2.1 *Potential flow methods*

Beside the later proposed ALM, basic methods of fluid dynamics are used in this thesis in order to provide an estimation of a problem or compare accuracy.

A set of methods for lifting bodies in steady flows are provided by potential flow methods, such as implemented in the XFOIL [Dre89] and XFLR5 software [Dep10]. The former offers a panel method computing aerodynamic coefficients of an airfoil section. The XFLR5 tool is based on XFOIL and solves 3D problems. Both tools assume a constant inflow and therefore handle stationary problems only. The available solvers in XFLR5 are a lifting-line theory (LLT), vortex lattice method (VLM) and a 3D panel method. The LLT and the VLM are outlined in appendix A.2.1 and A.2.2. A short derivation of the numerical panel method and its system matrices is depicted in the following.

Numerical panel method

The panel method offers a numerical approach to potential flow problems. This assumes that the fluid is principally steady, which however varies if a transient wake distribution is concerned. Further assumptions for the fluid are incompressible, inviscid and irrotational.

In the following a short derivation of the basic equations is depicted, compare [KP01]. The interface area between body and fluid shall be defined as surface Γ_f. By solving the Laplace's equation for the mentioned assumptions, the total potential of the control volume becomes zero,

$$\nabla^2 \Phi = 0\,. \tag{4.10}$$

With the Green's identity the velocity potential can be expressed as a distribution of sources σ and doublets μ,

$$\Phi = -\frac{1}{4\pi} \int_{\Gamma_f} \left[\sigma \left(\frac{1}{r} \right) - \mu \mathbf{n} \nabla \left(\frac{1}{r} \right) \right] d\Gamma + \Phi_\infty\,, \tag{4.11}$$

with vector $\mathbf{n}$ as surface normal and the free-stream potential Φ_∞.

After a short computation and defining a potential for the body wake, the potential states

$$\frac{1}{4\pi} \int_{\text{body+wake}} \mu \frac{\partial}{\partial n} \left(\frac{1}{r} \right) d\Gamma - \frac{1}{4\pi} \int_{\text{body}} \sigma \left(\frac{1}{r} \right) d\Gamma = 0\,. \tag{4.12}$$

The surface is discretised with n_p panels and the coefficients for the integration summarized in a_m for the doublets and b_m for the sources. For each collocation point and each unknown doublet strength μ_m the Equation (4.12) becomes

$$\sum_m a_m \mu_m = -\sum_m b_m \sigma_m \tag{4.13}$$

and gathered in a matrix formulation to solve the n_p equations,

$$\mathbf{A} \cdot \boldsymbol{\mu} = -\mathbf{B} \cdot \sigma \,. \tag{4.14}$$

Knowing the doublet distribution, the resulting force of a panel can be derived. The local coordinates of a panel are defined as $(\tilde{x}, \tilde{y}, \tilde{z})$ and thus the local velocity $\mathbf{u}_m$. Furthermore, the pressure coefficient c_{p_m} and force coefficient c_{f_m} are introduced. The area of a panel is declared as S_m.

$$\mathbf{u}_m = \mathbf{u}_{\infty_m} + \left(-\frac{\partial \mu_m}{\partial \tilde{x}}, -\frac{\partial \mu_m}{\partial \tilde{y}}, -\sigma_m \right) \tag{4.15}$$

$$\mathbf{c}_{p_m} = 1 - \frac{\mathbf{u}_m^2}{\mathbf{u}_\infty^2} \tag{4.16}$$

$$\mathbf{c}_{f_m} = -\frac{\mathbf{c}_{p_m} S_m}{S} \cdot \mathbf{n}_m \tag{4.17}$$

$$\mathbf{f}_m = \mathbf{c}_{f_m} \frac{1}{2} \rho \mathbf{u}_\infty^2 S \tag{4.18}$$

$$= \left(1 - \frac{\mathbf{u}_m^2}{\mathbf{u}_\infty^2} \right) S_m \cdot \mathbf{n}_m \cdot \frac{1}{2} \rho \mathbf{u}_\infty^2 \tag{4.19}$$

With the Neumann boundary condition for the body surface follows

$$\sigma = \mathbf{n} \cdot \mathbf{u}_\infty \,. \tag{4.20}$$

An open source implementation is provided by [Baa12].

4.2.2 *Streamtube methods*

An approach specialised for vertical-axis turbines is the double-multiple streamtube (DST) method. Its basis, the multiple streamtube method is initially developed by [Str75]. It is an extension of the of blade element theory (BET) and a single streamtube model applied to vertical-axis turbines. For the BET, a precomputed table of aerodynamic properties of the airfoil is required.

The streamtube model observes the flow passing the turbine. In the multiple streamtube method the observed flow is discretised with multiple strips. In the DST, published in [Par81], the flow is split into up- and downstream side. An open source implementation is available by [Val14].

4.2.3 *Analytic lift distribution*

In order to provide an estimation of aerodynamic forces of a finite wing an analytic approach is used. The LLT provides a solution for the case of a wing with a constant downwash. The solution is an elliptic circulation distribution, as formulated in [Pra23].

The circulation strength is thus

$$\Gamma(z) = \Gamma_0 \sqrt{1 - \frac{2z}{s}^2}, \tag{4.21}$$

where z is the coordinate in span direction. For a given total wing lift coefficient C_L and an integration over the circulation strength the prefactor states

$$\Gamma_0 = \frac{2u_0 S C_L}{s\pi}. \tag{4.22}$$

4.3 ACTUATOR-LINE METHOD

The ALM is a model-based approach to determine resulting forces of a lifting body and the influence on the fluid flow. Instead of resolving the surrounding flow with a detailed boundary layer, a reduced model is applied. The ALM thereby represents the blade as a line of additional forces in the momentum equation. It was firstly applied on wind turbines by [SS02], later by [TSM07]; [Tro08] and [WM10]. A discretised *actuator-line* is schematically displayed in Figure 4.3. The actuator line can be interpreted as a line of *actuator points*, where each point represents the section-wise dynamics of the blade. These dynamics are processed in two ways. First, they provide the local lift and drag forces of the body in dependence of the flow field. Furthermore, they are applied to the momentum equation and determine the influence of the body on the surrounding flow.

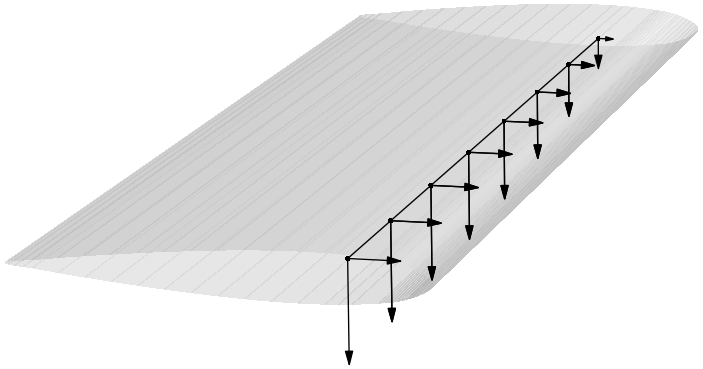

Figure 4.3.: Concept of an actuator-line representing force acting on the fluid generated from wing. Force is split in lift and drag.

The reduced model is based on results of experiments or a panel method. The basis is defined by a list of lift and drag coefficients for different angles of attack. This basis states as a mapping of inflow parameters to resulting forces $ALM : \mathbf{u} \mapsto f_L, f_D$. For 3D problems the distribution of the forces is calculated from 2D coefficients with a correction based on the induced velocity of a panel method with vortex elements (compare [Wen15]). The 2D coefficients are stored in a so-called look-up table.

This chapter outlined a set of numerical approaches to fluid dynamics. Flow problems in the context of turbines can be reduced to the dynamics of lifting bodies, characterised by their aerodynamic coefficients.

The ALM applied to RANS equations is used in this thesis to solve dynamics of lifting bodies in connection with a FSI. Beside this advanced approach, potential flow methods and a specialised approach for vertical-axis turbines are described.

5 FLUID-STRUCTURE INTERACTION

The influence of the fluid on the body and vice versa is defined as FSI occurring in many technical applications, such as the wing flutter of an airplane [BE98] or in turbomachines [Vah+01]. This chapter depicts how to engage the simulation of a FSI phenomenon.

The interaction occurs in different scales, which can be distinct into two *coupling types*, *weak* and *strong* FSI. A strong, also called two-way FSI occurs at a ratio of solid to fluid density of approximately $\frac{\rho_s}{\rho_f} < 10^3$ [BKF12]. At higher ratios the coupling can be assumed as weak or one-way coupling, i.e. the fluid has an influence on the body, but the motion of the body has none on the fluid within a time step.

The interface between fluid domain and body is defined by a set of interface conditions. The first condition demands equal displacement $\mathbf{d}_\Gamma$ for the fluid, lower index f, and the body, lower index s,

$$\mathbf{d}_{\Gamma_f} = \mathbf{d}_{\Gamma_s} . \tag{5.1}$$

The second condition assumes equal velocities,

$$\mathbf{u}_{\Gamma_f} = \mathbf{u}_{\Gamma_s} , \tag{5.2}$$

and the third equal forces or stresses, respectively,

$$\mathbf{f}_{\Gamma_f} = \mathbf{f}_{\Gamma_s} . \tag{5.3}$$

An *implicit* coupling enforces the interface states on all domains to be equal and is thus a strong coupling. In *explicit* coupling, only the interface conditions (5.2) and (5.3) are fulfilled explicitly with an iterative scheme, and it is therefore referred to as a weak coupling [Fer11].

The coupling of the two physical domains fluid and body requires the exchange of information, in general the forces of the fluid acting on a body and the spatial position of the body itself. The sequence in which the exchange takes place can vary, as the type and concept of fluid and mechanical solver differ. The different methods will be referred to as *coupling method*. The principal sequences of the solver calls are outlined in Figure 5.1.

The two different approaches to the coupling method are the *partitioned* approach, on which every solver is principally executed stand-alone, and the *monolithic* approach, at which the governing equations of both systems are coupled and solved at once [HWD04]. The advantages and drawbacks of each coupling method depend strongly on the coupling type and on the solvers used on each domain [HWL12].

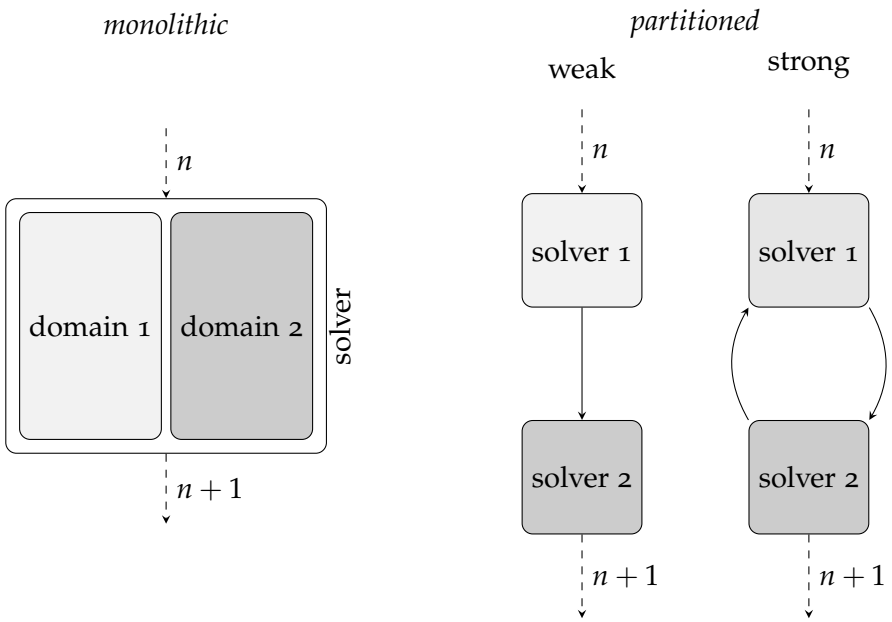

Figure 5.1.: Sequence of solver calls of different approaches for time step n. Domains are marked with different levels of grey.

The advantage of the monolithic approach is potentially lower computational costs in a strong coupling scheme, as the exchange of information is explicitly fulfilled in the system equation. In contrast, the partitioned approach requires a transfer of information over the interface after every solution step until convergence is reached. Particularly for strong FSI problems, the number of convergence iterations is large [Deg+08]. For a weak coupling the advantage of the monolithic approach drops, since only a single exchange is performed per time step.

Regarding the choice of solvers, the advantage of less convergence steps in the monolithic approach may vanish. If large systems are handled, it becomes a drawback to handle both fluid and mechanical problem in one system of equations [FWR07]. Another drawback is caused by large deformation, which may require a cost intensive remeshing [GTK06].

Beside performance considerations, the implementation needs to be examined. Firstly, some solution processes inhibit the generation of a node-by-node connection to another solver for a monolithic approach. This is the case, if both solvers base upon iterative procedures. Furthermore, in terms of stability it is suitable to use separate solvers [Weno6]. Thereby, known problems can be identified and distinguished from those, which rise up from the interaction.

In this work the partitioned approach is applied to FSI problems. It provides the flexibility to choose the ALM on the fluid side for an optimized and parallelised CFD solver. Furthermore, the complexity is kept low and problems on each domain can be mastered a priori by running the solvers separately.

Nevertheless, a monolithic approach will be depicted and implemented in principle to verify the concept.

5.1 PARTITIONED APPROACH

The partitioned approach couples both solvers over an interface Γ. The solvers are defined as mapping of interface displacements to forces and vice versa. The mechanical solver yields $S_\Gamma : \mathbf{d}_\Gamma \mapsto \mathbf{f}_\Gamma$ and the fluid solver $F_\Gamma : \mathbf{f}_\Gamma \mapsto \mathbf{d}_\Gamma$. Against the background of a time marching scheme, the latest time step is marked with the upper index with n and the currently computed time step is marked with $n+1$ and the current convergence step with $k+1$. The interface displacements, $\mathbf{d}_\Gamma$, i.e. the body positions, are a function of the interface forces,

$$\mathbf{d}_\Gamma^{n+1} = S_\Gamma(\mathbf{f}_\Gamma^{n+1})\,. \tag{5.4}$$

In return, the interface forces are a function of the displacement,

$$\mathbf{f}_\Gamma^{n+1} = F_\Gamma(\mathbf{d}_\Gamma^{n+1})\,. \tag{5.5}$$

In the partitioned approach, the interface conditions are handled explicitly. In order to fulfil the force condition (5.3) an estimation of the interface displacement is computed by

$$\tilde{\mathbf{d}}_{\Gamma,k+1}^{n+1} = S_\Gamma\left(F_\Gamma(\mathbf{d}_{\Gamma,k}^{n+1})\right)\,. \tag{5.6}$$

Equation (5.6) leads to a fixed-point problem, which defines the constitutive fluid-structure interface problem [DBV09],

$$\begin{aligned}\mathbf{r}_{\Gamma,k+1}^{n+1} &= \tilde{\mathbf{d}}_{\Gamma,k+1}^{n+1} - \mathbf{d}_{\Gamma,k}^{n+1} \\ &\stackrel{!}{=} 0\,.\end{aligned} \tag{5.7}$$

The fixed-point problem is solved by sequentially reinserting the solvers' results until convergence is reached. The convergence criterion is reached, when the residual $\mathbf{r}_{\Gamma,k+1}^{n+1}$ drops under a bound η,

$$\frac{\left\|\mathbf{r}_{\Gamma,k+1}^{n+1}\right\|^2}{\sqrt{n_\Gamma}} < \eta\,, \tag{5.8}$$

where n_Γ is the number of interface states [BKF12]. Instead of displacements, all interface states can be monitored, gathered in the interface state vector

$$\mathbf{q}_\Gamma = \begin{bmatrix}\mathbf{d}_\Gamma \\ \mathbf{f}_\Gamma\end{bmatrix} \tag{5.9}$$

and thus

$$\mathbf{r}_{\Gamma,k+1}^{n+1} = \tilde{\mathbf{q}}_{\Gamma,k+1}^{n+1} - \mathbf{q}_{\Gamma,k}^{n+1} \,. \tag{5.10}$$

The sequence of the solver calls differs in the convergence step the operation is related to [Weg10]. In the Jacobi method each solver uses the results of the previous convergence step. A Gauß-Seidel method calls one solver first and then hands over the estimation to the second solver within the current convergence step. For a Jacobi method this yields

$$\mathbf{d}_{\Gamma,k+1}^{n+1} = S_\Gamma(\mathbf{f}_{\Gamma,k}^{n+1}) \tag{5.11}$$

$$\mathbf{f}_{\Gamma,k+1}^{n+1} = F_\Gamma(\mathbf{d}_{\Gamma,k}^{n+1}) \,, \tag{5.12}$$

whereas a Gauß-Seidel method yields

$$\mathbf{d}_{\Gamma,k+1}^{n+1} = S_\Gamma(\mathbf{f}_{\Gamma,k}^{n+1}) \tag{5.13}$$

$$\mathbf{f}_{\Gamma,k+1}^{n+1} = F_\Gamma(\mathbf{d}_{\Gamma,k+1}^{n+1}) \,. \tag{5.14}$$

The Gauß-Seidel method is common in FSI problems which are not fully parallelised, compare [BKF12]; [KW08]; [DBV09]; [BS06]. It is also chosen for the scope of this work. The sequence of the solver calls and the convergence loop is indicated in Figure 5.2.

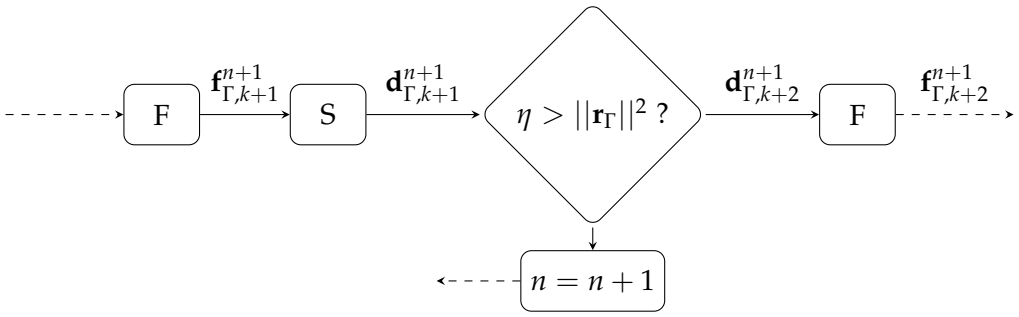

Figure 5.2.: Sequence of solver calls in partitioned approach with convergence criterion at time step n and convergence step k.

Beside the depicted sequence, another approach is applicable, in which the inverse of the mechanical solver S_Γ^{-1} is available, as shown in [KW08] or mentioned by [UB13]. However, the inverse is not accessible for the MBS solver used in this work.

To reduce the overall computational time, a method for the acceleration of convergence is employed, depicted in the Section 5.2.

5.2 RELAXATION SCHEMES

The reduction of coupling steps is commonly carried out by an underrelaxation of the interface states, as in [Vie06]. Relaxation is applied before every convergence step by the following formula,

$$\mathbf{d}_{\Gamma,k+1}^{n+1} = \xi_{k+1}\tilde{\mathbf{d}}_{\Gamma,k+1}^{n+1} + (1-\xi_{k+1})\mathbf{d}_{\Gamma,k}^{n+1}\,. \tag{5.15}$$

The relaxation parameter ξ thereby ranges from 0 to 1.

A common relaxation scheme is the Aitken's underrelaxation [KW08] computing the scalar relaxation parameter ξ. This scheme can also be extended to a vectorial formulation using $\boldsymbol{\xi}$.

A set of other schemes is based on the concept of Newton-Raphson iterations [DBV09]. A Newton-Raphson iteration in order to compute the interface displacement is applied by

$$\mathbf{r}'_{\Gamma,k+1}\Delta\mathbf{d}_{\Gamma,k} = -\mathbf{r}_{\Gamma,k} \tag{5.16}$$

$$\mathbf{d}_{\Gamma,k+1} = \mathbf{d}_{\Gamma,k} + \Delta\mathbf{d}_{\Gamma,k}\,. \tag{5.17}$$

Here, the Jacobian matrices $\mathbf{r}'_{\Gamma,k+1} = \frac{\partial \mathbf{r}_{\Gamma,k+1}}{\partial \mathbf{d}_\Gamma}$ of the solvers are not directly accessible. However, they can be computed approximatively, thus these schemes are called quasi-Newton iterations and will be depicted in Section 5.2.2.

5.2.1 *Aitken's underrelaxation*

The underrelaxation by Aitken or Aitken's Δ^2 method is a series acceleration, which improves convergence rates with the use of the previous two convergence steps. The formula for the accelerated step x' is

$$x'_k = x_k - \frac{(x_k - x_{k-1})^2}{x_k - 2x_{k-1} + x_{k-1}}\,, \tag{5.18}$$

see [Mac86]. In terms of Equation (5.15), the scalar underrelaxation scheme can be formulated as

$$\xi_{k+1} = -\xi_k \frac{r_k}{r_{k+1} - r_k}\,, \tag{5.19}$$

with $r_{k+1} = \tilde{x}_{k+1} - x_k$. This scheme can be applied to $\|\mathbf{r}_{k+1}\|^2$, in this case ξ becomes a global relaxation parameter. Alternatively, it can be applied node-wise, where Equation (5.19) is calculated for each node separately.

Instead, the interface states can be handled as vector. A vectorial approach is formulated as

$$\boldsymbol{\xi}_{k+1} = \boldsymbol{\xi}_k \frac{\mathbf{r}_k^T(\mathbf{r}_{k+1} - \mathbf{r}_k)}{\|\mathbf{r}_{k+1} - \mathbf{r}_k\|^2}\,, \tag{5.20}$$

see [KW08] and [IT69].

In the application of all schemes it is suitable to apply a limit,

$$\xi = \max(\xi, 1) \tag{5.21}$$

$$\xi = \min(\xi, \xi_{\min}) \,. \tag{5.22}$$

The lower bound $\xi_{\min}$ is set to a small value. If ξ_k would become zero, Equation (5.19) is zero for following ξ_{k+1} terms.

The formulation of the Aitken relaxation for vectors can vary, see [Mac86]. However, Bogaers, Kok, and Franz and other already have showed the advantage of quasi-Newton methods.

5.2.2 *Quasi-Newton methods*

Quasi-Newton methods accelerate the convergence of the fixed-point iterations by adapting the Newton-Raphson algorithm. Since the Jacobian $\mathbf{r}'_{\Gamma,k+1}$ is not accessible, an approximation based on the system dynamics is considered. The previous steps of the coupling iterations reflect these dynamics. Gathering the steps in an observation matrix, an approximative Jacobian matrix can be computed. The observation matrices for the residuals and the displacements are

$$\mathbf{V}^k = \left[\Delta\mathbf{r}^k_{\Gamma,0}, \ldots, \Delta\mathbf{r}^k_{\Gamma,k-1}\right] \qquad \text{with } \Delta\mathbf{r}^k_{\Gamma,i} = \mathbf{r}(\mathbf{d}_{\Gamma,k}) - \mathbf{r}(\mathbf{d}_{\Gamma,i}) \tag{5.23}$$

$$\mathbf{W}^k = \left[\Delta\tilde{\mathbf{d}}^k_{\Gamma,0}, \ldots, \Delta\tilde{\mathbf{d}}^k_{\Gamma,k-1}\right] \qquad \text{with } \Delta\tilde{\mathbf{d}}^k_{\Gamma,i} = \tilde{\mathbf{d}}_{\Gamma,k} - \tilde{\mathbf{d}}_{\Gamma,i} \,, \tag{5.24}$$

with $\mathbf{V}^k, \mathbf{W}^k \in \mathbb{R}^{n_k \times n_\Gamma}$ containing the number of convergence steps n_k and the number of states n_Γ. The residual $\mathbf{r}$ is defined as $\mathbf{r}(\mathbf{d}_{\Gamma,k}) = \tilde{\mathbf{d}}_{\Gamma,k} - \mathbf{d}_{\Gamma,k}$, see Equation (5.7). The quasi-Newton method is considered as mapping from a computed displacement, as in Equation (5.6), to an accelerated state, $QN : \tilde{\mathbf{d}}_{\Gamma,k+1} \mapsto \mathbf{d}_{\Gamma,k+1}$ for the current convergence step k.

The change in the next convergence step is assumed to be a linear combination of the prior states

$$\Delta\mathbf{r}_{\Gamma,k} \approx \mathbf{V}^k\boldsymbol{\alpha} \tag{5.25}$$

$$\Delta\tilde{\mathbf{d}}_{\Gamma,k} \approx \mathbf{W}^k\boldsymbol{\alpha} \,, \tag{5.26}$$

with $\boldsymbol{\alpha} \in \mathbb{R}^{n_k}$. In most cases the number of gathered steps is smaller than the interface states $n_k < n_\Gamma$ and thus Equation (5.25) is overdetermined. A solution for $\boldsymbol{\alpha}$ is then received by LS approximation,

$$\boldsymbol{\alpha} = (\mathbf{V}^k)^{-1}\Delta\mathbf{r}_{\Gamma,k} \,. \tag{5.27}$$

Using the definition of Equation (5.7), Equation (5.26) yields

$$\Delta \mathbf{d}_{\Gamma,k+1} = \mathbf{W}^k \boldsymbol{\alpha} - \Delta \mathbf{r}_{\Gamma,k} \,. \tag{5.28}$$

Assuming the desired residual for the current convergence step to be zero

$$\Delta \mathbf{r}_{\Gamma,k} = \mathbf{0} - \mathbf{r}_{\Gamma,k} \,, \tag{5.29}$$

and taking into account Equation (5.16) it yields

$$\Delta \mathbf{d}_{\Gamma,k+1} = \mathbf{W}^k \boldsymbol{\alpha} + \mathbf{r}_{\Gamma,k} \tag{5.30}$$

$$= (\mathbf{r}'_{\Gamma,k})^{-1}(-\mathbf{r}_{\Gamma,k}) \,. \tag{5.31}$$

Thus, the Jacobian matrix is not explicitly computed, but the resulting product, compare [BKF12].

The accelerated displacement finally yields,

$$\mathbf{d}_{\Gamma,k+1} = \mathbf{W}^k \left((\mathbf{V}^k)^{-1} \Delta \mathbf{r}_{\Gamma,k} \right) + \tilde{\mathbf{d}}_{\Gamma,k} \,. \tag{5.32}$$

However, for the first two convergence steps of an iteration, a constant relaxation is applied, since at least two steps are needed in order to construct the observation matrices. An alternative to a constant relaxation is depicted in Section 5.2.5.

This scheme is strongly dependent on the quality of the LS estimation and the accuracy of its implementation. Furthermore, by gathering convergence steps of multiple time steps, the method may fail, since it is sensitive to large changes in the observation matrices or a too large number of observed steps.

5.2.3 *Proper orthogonal decomposition*

The proper orthogonal decomposition (POD) evades the sensitivity to ill-conditioned observation matrices of the LS-based approach. It achieves an optimal, lower dimensional approximation of the observed data.

In this scheme previous states and errors are gathered and the dynamic decomposed into its eigenspace. This way, only the parts with the largest influence are taken into account or in terms of eigenmodes, parts with the highest energy.

The decomposition is applied to the autocorrelation matrix

$$\mathbf{R}_v = \frac{1}{n_n} \mathbf{V}\mathbf{V}^T \,, \tag{5.33}$$

with n_n as the number of rows of $\mathbf{V}$. By solving the eigenvalue problem

$$\mathbf{R}_v \mathbf{X}_{\Gamma,v} = \boldsymbol{\lambda}_{\Gamma,v} \mathbf{X}_{\Gamma,v} \,, \tag{5.34}$$

with $\mathbf{R}_v \in \mathbb{R}^{n_n \times n_n}$, $\boldsymbol{\lambda}_{\Gamma,v} \in \mathbb{R}^{n_v}$, the eigenvector matrix $\mathbf{X}_{\Gamma,v} \in \mathbb{R}^{n_n \times n_v}$ with n_v eigenvalues is obtained. Since the autocorrelation matrix $\mathbf{R}_v$ is symmetric and positive semidefinite, an eigensolver, which benefits from the properties of a selfadjoint matrix is used. For the used implementation, see [Gun+13].

The basis modes of the system are computed as a linear combination of the eigenvectors

$$\boldsymbol{\varphi} = \mathbf{X}_{\Gamma,v}^T \mathbf{V} \,. \tag{5.35}$$

In order to drop irrelevant observed dynamics only the highest n_c-th modes φ_i are used. The corresponding eigenvalues are denoted by λ_i of the eigenvector in $\mathbf{x}_{v,i}$. The bound is defined by

$$\frac{\lambda_1}{\lambda_c} \leq 10^{12} \,, \tag{5.36}$$

where λ_1 is the highest and λ_c the smallest eigenvalue used. An advantage of this limitation is the ability to use an iterative eigensolver and solve only for the first n_c modes.

Now, Equation (5.25) can be expressed by new basis modes,

$$\Delta \mathbf{r}_{\Gamma,k+1} \approx \boldsymbol{\varphi}\, \boldsymbol{\alpha}_v \tag{5.37}$$

and is inserted in Equation (5.28). In order to reduce numerical errors, the new term is solved with a linear solver based on a Householder QR-decomposition depicted as

$$\Delta \tilde{\mathbf{d}}_{\Gamma,k+1}^{n+1} = \mathbf{W}^T \mathbf{X}_{\Gamma,v} \left(\left(\boldsymbol{\varphi}^T \right)^{-1} \Delta \mathbf{r}_{\Gamma,k}^{n+1} \right) . \tag{5.38}$$

The definition of Equation (5.32) with a POD states then

$$\Delta \mathbf{d}_{\Gamma,k+1}^{n+1} = \mathbf{W}^T \mathbf{X}_{\Gamma,v} \left(\left(\boldsymbol{\varphi}^T \right)^{-1} \Delta \mathbf{r}_{\Gamma,k}^{n+1} \right) + \tilde{\mathbf{d}}_{\Gamma,k+1} \,. \tag{5.39}$$

This scheme was originally developed by [BKF12], but in the scope of this work extended to the LS approach introduced in [DBV09].

5.2.4 *Choice of states*

In the quasi-Newton methods illustrated above, the observation matrices hold the residual $\mathbf{r}_\Gamma$ and the interface displacement $\mathbf{d}_\Gamma$. However, the choice of states may differ, as [BKF12] considers forces and positions, whereas [UB13] refers to states in general. In [DBV09] the states are limited to interface displacement, as in the sections above.

In the present work the relaxation schemes are based on the interface displacements as shown in [DBV09]. The other schemes are implemented and examined, though. The convergence rates are similar, as affirmed in [Bog+14], but the residual based approach

retains fewer states in the observation matrix achieving a potentially lower computational time.

The set of states can be extended to interface velocities $\dot{\mathbf{d}}_\Gamma$, which are relaxed by passing the interface. A relaxation of velocities is implemented and examined in Section 5.3. The relaxation of the velocity has a large influence on setups in which the body velocity is approximately in the same order of magnitude as the fluid flow, as it directly influences the resulting forces of the ALM. A velocity relaxation cannot be applied for every method, though. A quasi-Newton method based on displacements and forces, presumes that two observation matrices of the same size for two sets of states can be created.

5.2.5 *Initial iteration step*

Some acceleration methods such as the Aitken's method fail in calculating correct relaxation factors for time step crossovers. Thus, a constant relaxation is commonly used for the first convergence steps of a time step.

A method proposed by [Gal10] evades this conservative approach using polynomial extrapolation. The previous n_p interface displacements are used to extrapolate the displacement of the first iteration step $\mathbf{d}_{\Gamma,0}$ in order to additionally accelerate the convergence loop.

The polynomial extrapolations for 1st to 3rd order are

$$\mathbf{d}_{\Gamma,0}^{n+1} = 2\mathbf{d}_\Gamma^n - \mathbf{d}_\Gamma^{n-1} \tag{5.40}$$

$$\mathbf{d}_{\Gamma,0}^{n+1} = 3\mathbf{d}_\Gamma^n - 3\mathbf{d}_\Gamma^{n-1} + \mathbf{d}_\Gamma^{n-2} \tag{5.41}$$

$$\mathbf{d}_{\Gamma,0}^{n+1} = 4\mathbf{d}_\Gamma^n - 6\mathbf{d}_\Gamma^{n-1} - \frac{20}{3}\mathbf{d}_\Gamma^{n-2} - \mathbf{d}_\Gamma^{n-3}, \tag{5.42}$$

where $\mathbf{d}_\Gamma^n$ is the converged displacement of the previous time step n. [Gal10]

Beside the potential acceleration, the extrapolation provides stability, since the first steps are often error-prone and result in large displacements or forces.

5.3 STUDIES OF CONVERGENCE

As a reason of comparing the acceleration of the listed methods, a study of convergence of the tolerance η was carried out. For reference, a constant relaxation of 0.5 is used. The number of convergence steps of the constant relaxation is compared to an Aitken method with node-wise relaxation. The initial constant relaxation for the Aitken scheme is 0.5. Quasi-Newton schemes in this study observe all past steps, including time step changes. The initial relaxation for the first step is 0.1.

The analysed setup is an order-reduced model of a wing coupled to a panel code. The wing is pitched with a sinusoidal function over time and deflected by the flow. The FE model of the wing has a Young's modulus of aluminium and the fluid medium is water. The resulting average number of convergence steps $\bar{n}_k$ are plotted in Figure 5.3.

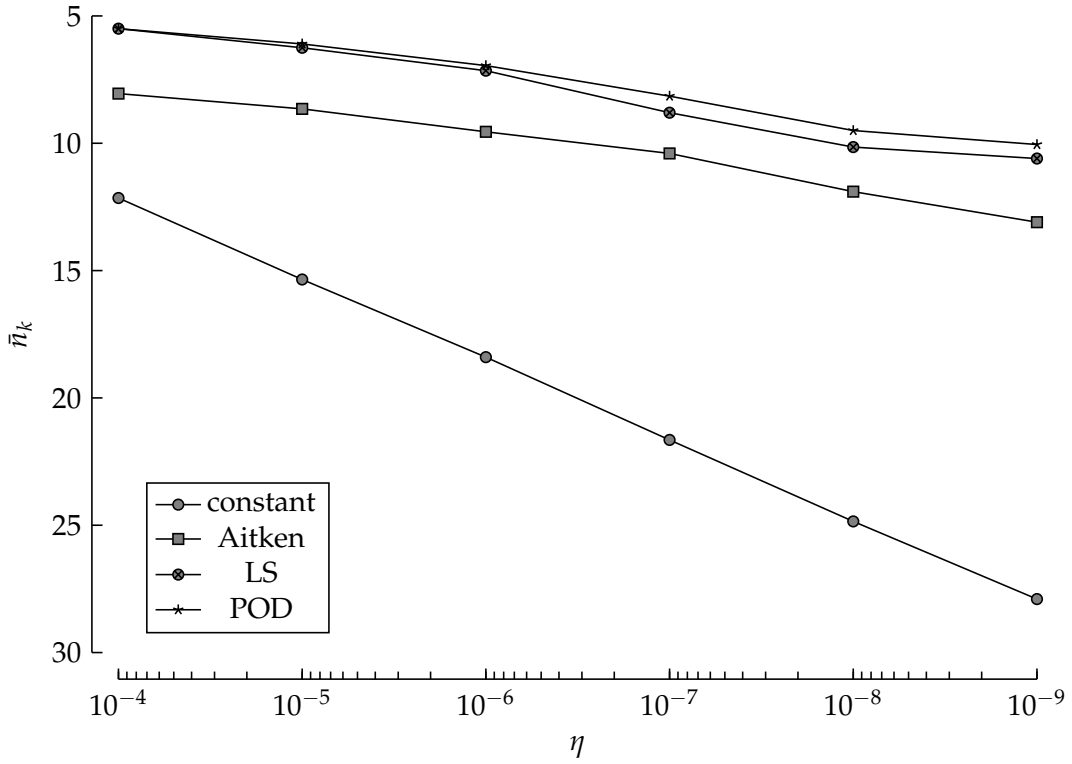

Figure 5.3.: Study of convergence rates for different relaxation schemes. Average number of convergence steps is plotted against convergence bound on a logarithmic scale.

The constant relaxation in this study offers a stable solution with a linearly increasing number of convergence steps per refined tolerance. The Aitken method accelerates convergence observably and keeps below 15 iterations for low tolerances.

The quasi-Newton methods need nearly half the steps of the Aitken method. For a lower tolerance the POD uses slightly fewer steps than the LS approach. The difference increases for stiffer problems and a larger amount of observed steps.

Nevertheless, the LS approach can give good convergence rates for stiff problems. But this requires well-conditioned matrices aided by the limitation of the number of observed convergence steps.

In a further study, the available methods are applied to the coupling with the ALM. The scenario is an airfoil in water flow mounted on a spring suspension (compare [MPB11]). The suspension allows a heave and pitch motion so the fluid deflects the airfoil. The resulting average iteration steps of the simulation are listed in Table 5.1.

The POD is applied to different states, which are force, displacement and velocity of the interface. As a basis both, residuals and direct states are used. The number of observed previous steps is varied. In the LS approach the observation matrix is reset after every time step.

The lowest number of convergence steps is achieved by the POD approach based on residuals and relaxing forces only. For other setups this result may vary, because the relaxation of forces is an intervention in the ALM and thus divergence can occur. Similarly, the constant relaxation can give good convergence rates for a light relaxation of 0.8, however can potentially fail with divergence in a single time step. The LS approach can give good rates as well, but is sensitive to time step changes and larger observation matrices.

The acceleration rates are strongly problem-dependent. Reviews show the potential of current methods [Lin+15]; [BD12]. For the presently examined setups conservative methods provide sufficient convergence rates, because the problems analysed in this work are generally non-stiff. For stiff problems, quasi-Newton methods reveal their strength.

For further simulations in connection with the ALM, the observed states are limited to 30-50 convergence steps, which equals up to eight time steps. This yields a good trade-off between acceleration and computational costs of the accelerating method itself. The cost intensive element of the POD is mainly the computational time of the eigensolver.

5.4 MONOLITHIC APPROACH

In a monolithic approach to FSI, both the mechanical and the fluid system equations are dealt with by one solver. This approach is illustrated by the example of a coupling to a numerical panel code (see Section 4.2.1). This implementation belongs to the Newton-Raphson based methods in contrast to other, such as an arbitrary Lagrangian–Eulerian (ALE) based methods [HT06].

The system matrices of the MBS and the panel code are based on a combined set of states. The set contains firstly the position of the body and excitation of the flexible eigenmodes, respectively. The remaining states include the fluid properties, which are

Table 5.1.: Average number of iteration steps for different relaxation schemes and observed steps used by coupled simulation with the ALM. The problem configuration is derived from [MPB11]. Observed steps marked with $*$ were reset after a time step.

method	relaxed states	basis	observed steps	average iterations
constant	$\mathbf{f}_\Gamma$	–	–	86.3
POD	$\mathbf{f}_\Gamma$	residuals	30	**23.4**
POD	$\mathbf{f}_\Gamma$	residuals	50	25.0
POD	$\mathbf{f}_\Gamma$	residuals	100	26.6
POD	$\mathbf{d}_\Gamma$	residuals	30	31.1
POD	$\mathbf{f}_\Gamma$, $\mathbf{d}_\Gamma$	residuals	30	24.2
POD	$\mathbf{f}_\Gamma$, $\mathbf{d}_\Gamma$, $\dot{\mathbf{d}}_\Gamma$	residuals	30	25.8
POD	$\mathbf{f}_\Gamma$	states	30	42.9
POD	$\mathbf{f}_\Gamma$, $\mathbf{d}_\Gamma$	states	30	42.9
LS	$\mathbf{f}_\Gamma$	residuals	5^*	27.9
LS	$\mathbf{f}_\Gamma$	residuals	15^*	34.3

the doublet strengths per panel. Additionally, the momentum states $\mathbf{p}$ from Equation (3.5) are included in form of the constraining forces $\mathbf{f}_l$,

$$\mathbf{q}^* = \begin{bmatrix} \mathbf{x}_l \\ \dot{\mathbf{x}}_l \\ \mathbf{f}_l \\ \boldsymbol{\mu}_m \end{bmatrix} . \tag{5.43}$$

The state vector is of the size $\mathbf{q}^* \in \mathbb{R}^{n_n \cdot (3 \cdot 6) + n_p}$, where n_n are the number of nodes in the MBS and n_p are the number of panels. The lower index l lists all n_n nodes and the index m all n_p panels.

Concerning the definition of the Newton-Raphson scheme in Equation (3.11) the Jacobian matrix is defined as $\mathbf{J}_{\dot{\mathbf{q}}} = \frac{\partial \mathbf{r}}{\partial \dot{\mathbf{q}}} = f(\mathbf{q}, \dot{\mathbf{q}})$. In the new system including the panel states, the residual function is defined as $\mathbf{r}_p = f(\mathbf{q}, \dot{\mathbf{q}}, \boldsymbol{\mu})$ and thus the Jacobian matrix yields

$$\mathbf{J}_{\dot{\mathbf{q}}^*} = f(\mathbf{q}, \dot{\mathbf{q}}, \dot{\boldsymbol{\mu}}) = f(\dot{\mathbf{x}}, \ddot{\mathbf{x}}, \dot{\boldsymbol{\mu}}) . \tag{5.44}$$

The panel code Equations (4.14) need to be integrated into the Newton-Raphson steps to enable a solution of both domains using the MBS solver. Regarding the solution step

in Section 3.2, the residual function $\mathbf{r}_p$ and the corresponding Jacobian matrix must be formulated as

$$\mathbf{J}_\mu = -\mathbf{A} \tag{5.45}$$
$$:= \left(\frac{\partial \mu_i}{\partial \mu_j}\right) \tag{5.46}$$
$$\mathbf{r}_\mu = \mathbf{B} \cdot \sigma + \mathbf{A} \cdot \boldsymbol{\mu}\,. \tag{5.47}$$

Using these definitions a regular Newton-Raphson step leads to the solution of the panel code,

$$\mathbf{x}^{k+1} = \mathbf{x}^k - \mathbf{J}_\mu^{-1}(\mathbf{x}^k)\mathbf{f}(\mathbf{x}^k) \tag{5.48}$$
$$\boldsymbol{\mu}^{k+1} = \boldsymbol{\mu}^k - \mathbf{J}_\mu^{-1}\mathbf{r} \tag{5.49}$$
$$= \boldsymbol{\mu}^k - \mathbf{J}_\mu^{-1}\left(\mathbf{B} \cdot \sigma + \mathbf{A} \cdot \boldsymbol{\mu}^k\right) \tag{5.50}$$
$$= -\mathbf{J}_\mu^{-1}\left(\mathbf{B} \cdot \sigma\right) \tag{5.51}$$
$$= \mathbf{A}^{-1}\left(\mathbf{B} \cdot \sigma\right) \quad \blacksquare\,. \tag{5.52}$$

In this definition both the mechanical and fluid problem are solved simultaneously, however not connected to each other. The connection is described in the off-diagonal entries of the Jacobian matrix. The entries are computed by partial derivatives of the panel code with respect to mechanical states.

The entries of the Jacobian matrix concerning the forces acting on the body are derived in the following. Thereby, rotational parts of the MBS state vector are neglected, since the position and velocity of the panel nodes define the force components entirely. The doublet strength derivative of a panel in the local coordinates $(\tilde{x}, \tilde{y}, \tilde{z})$ is defined as $\dot{\boldsymbol{\mu}}_m = \left(-\frac{\partial \mu_{\tilde{x}}}{\partial \tilde{x}}, -\frac{\partial \mu_{\tilde{y}}}{\partial \tilde{y}}, -\sigma_{\tilde{z}}\right)$.

The force per panel is a function of the pressure coefficient, the panel area S_m, the panel normal $\mathbf{n}_m$ and the global velocity $\mathbf{u}_\infty$ and local velocity $\mathbf{u}_m$ for each panel m, see Equation (4.19),

$$\mathbf{f}_m = f(\mathbf{c}_{p_m}, S_m, \mathbf{n}, \mathbf{u}_m) \tag{5.53}$$
$$= \left(1 - \frac{\mathbf{u}_{\infty_m}^2}{\mathbf{u}_\infty^2} + \frac{\dot{\boldsymbol{\mu}}}{\mathbf{u}_\infty^2}\right) \cdot S_m \cdot \mathbf{n} \cdot \frac{1}{2}\rho\mathbf{u}_\infty^2 \tag{5.54}$$
$$= \tfrac{1}{2} S_m \mathbf{n} \rho \left(\mathbf{u}_\infty^2 - \mathbf{u}_{\infty_m}^2 + \dot{\boldsymbol{\mu}}\right)\,. \tag{5.55}$$

The entries of the Jacobian matrix with respect to position and doublet strength are computed,

$$\frac{\partial \mathbf{f}_m}{\partial \dot{\mathbf{x}}} = S_m \mathbf{n} \rho \left(\mathbf{u}_\infty - \mathbf{u}_{\infty_m} \right) \tag{5.56}$$

$$\frac{\partial \mathbf{f}_m}{\partial \dot{\boldsymbol{\mu}}} = \tfrac{1}{2} S_m \mathbf{n} \rho \tag{5.57}$$

The derivative with respect to the position is calculated from equation (4.14) and (4.20),

$$\frac{\partial \boldsymbol{\mu}}{\partial \dot{\mathbf{x}}} = \mathbf{B} \cdot (-\mathbf{n}) \,. \tag{5.58}$$

Gathering all the terms of the Jacobian matrix $\mathbf{J}_{\dot{\mathbf{q}}^*}$, the coupling is defined explicitly and executed in the Newton-Raphson iterations. The missing sub-matrices of the Jacobian matrix $\frac{\partial \dot{\mathbf{x}}}{\partial \mathbf{f}}, \frac{\partial \ddot{\mathbf{x}}}{\partial \mathbf{f}}, \frac{\partial \mathbf{f}}{\partial \mathbf{f}}, \frac{\partial \boldsymbol{\mu}}{\partial \mathbf{f}}, \frac{\partial \mathbf{x}}{\partial \boldsymbol{\mu}}$ are zero or can be neglected, since they are not influencing the interface between body motion and forces.

The implemented monolithic approach achieves satisfactory convergence and accurate results for a basic and stationary setup. The configuration inhibits deeper examination, because the integrated panel method lacks flexibility and transient terms. In addition, the solver structure of MBDyn is not designed for numerous states, which are added by the panel method. Therefore, panel code methods use adapted solvers for large system of equations, such as the biconjugate gradient stabilized method (BiCGSTAB) of [Vor92] in [Baa12].

This chapter depicts the different approaches to solve a FSI problem. The partitioned approach is presented in detail, including methods to accelerate the convergence rates. The parameters of the acceleration methods are tuned problem-dependent.

6 VALIDATION

The depicted solvers for the fluid domain and the FSI coupling will be verified with analytic approximations and validated with experimental results. A step-by-step validation of components of the entire simulation is required to assure correct statements regarding the dynamics of a complexer model. On the fluid side the properties of a 3D blade in a stationary parallel flow are validated including both scalar results and distributions. The FSI side is validated for a stationary solution with a wing deflection and for a transient solution with a gust response of a turbine in a 2D domain. Finally, quasi-steady power coefficients of a VAWT and a VATT are compared to experimental results.

6.1 STEADY-STATE RESULTS

In a stationary setup, a blade is exposed to a uniform, constant flow hitting the blade with the angle of attack α. The simulation can be either computed with the stationary solver SIMPLE or with the transient solver PIMPLE. The latter simulation is run, until the blade forces are converged to a steady state. In the simulations in this chapter, PIMPLE is used for reasons of stability.

The resulting forces of the simulations are compared as non-dimensional quantities, i.e. lift and drag coefficient. The flow regime is defined by the Reynolds number and the fluid is air in all stationary studies.

STRAIGHT WING, NACA0015 In the experiments of [MT91] a wing in a parallel flow is examined. Detailed pressure distributions and derived quantities are proposed. The analysed straight wing has a NACA0015 airfoil section. Results of two flow regimes are extracted from the experiments with a Reynolds number of $1.50 \cdot 10^6$ and $2 \cdot 10^6$, respectively. Further values are listed in Table 6.1. The wing in this configuration is unswept, i.e. it is orientated perpendicular to the flow.

The experimental setup is realised in an ALM simulation. The used look-up tables for the 2D aerodynamic coefficients are based on the experiments in [SK81].

Additionally, the wing is computed in a LLT, a VLM and a panel method. Resulting lift and drag coefficients are listed in Table 6.2.

The error of the ALM relative to the experimental coefficients is below 10 % and the result can compete with the potential flow methods, but the ALM over-determines the lift coefficients for the analysed regimes. The potential flow methods are a more robust

Table 6.1.: Geometric configuration of wing and flow parameters for experiments in [MT91]. Derived values from the experimental description are listed separately.

airfoil section	NACA0015
pitch	$\beta = 6°, 8°$
aspect ratio	$\mathit{AR} = 6.6$
sweep angle	$0°$
chord length	$c = 20.4\,\text{in} = 0.51816\,\text{m}$
dynamic viscosity	$\nu = 1.50 \cdot 10^5\,\text{N}\,\text{s}\,\text{m}^{-1}$ (air, 20°)
density	$\rho = 1.205\,\text{kg}/\text{m}^3$
Reynolds number	$\text{Re} = 1.50 \cdot 10^6, 2 \cdot 10^6$
derived values	
inflow	$u_0 = \text{Re}/c \cdot \nu = 43.4, 57.9\text{m}\,\text{s}^{-1}$
span length	$s = c \cdot \mathit{AR} = 3.419856\,\text{m}$

Table 6.2.: Comparison of lift coefficients of rectangular wing to experimental data in [MT91] for different methods, Reynolds numbers and angles of attack.

Re	α	method				
		exp.	ALM	LLT	VLM	panel
$1.5 \cdot 10^6$	8°	0.617	0.670	0.641	0.615	0.626
$2 \cdot 10^6$	6°	0.471	0.502	0.488	0.464	0.471
$2 \cdot 10^6$	8°	0.613	0.670	0.645	0.615	0.626

choice for stationary problems, but are inapplicable for subsequent transient problems of vertical-axis turbines.

TAPERED WING, NACA0015 In a further validation, aerodynamic coefficients of a tapered wing are compared to experimental and numerical results. The experimental setup of [WF58] is used and its parameters listed in Table 6.3. A principal sketch of the configuration with its symmetry plane is displayed in Figure 6.1.

The look-up table of aerodynamic coefficients is generated from results in [SK81] as well.

The resulting lift and drag coefficients are listed in Table 6.4. The LLT diverged for the given setup, so no values are listed.

The resulting lift coefficient of the ALM has a larger relative error compared to the results of the straight wing. The drag coefficient is smaller than in the experiment and the potential flow methods. This implies a sensitivity of the ALM to the used look-up tables. For simulations with a strong dependence to the drag, the tables need to be generated

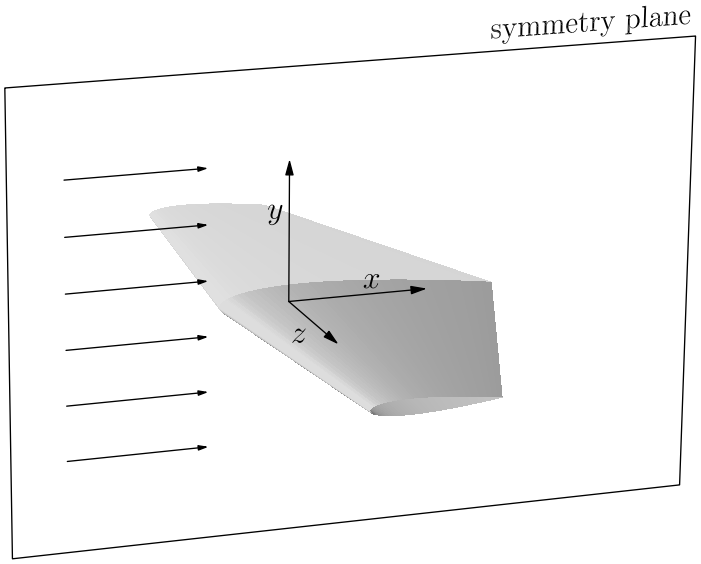

Figure 6.1.: Schematic configuration for fluid simulation of tapered wing with local coordinate system and symmetry plane. Direction of inflow is marked with arrows.

with caution and viscous models used for calculation of the coefficients. Nonetheless, this validation shows the capability of the ALM to simulate shaped blades.

6.1.1 *Lift distribution*

The lift distribution of a wing in a steady flow is validated with experimental results from [MT91]. This is an extension of the validation of scalar aerodynamic coefficients in the prior section. It assures a correct load distribution in FSI application, not only a correct entire load. The parameters of the setup are the same as listed in Table 6.1. The ALM approach in this setup is corrected with a model based distribution of the induced velocity, compare Section 4.3.

The resulting distribution of the section-wise lift coefficient is displayed in Figure 6.2 and Figure 6.3 and compared to experimental results of [MT91]. In the former, the lift coefficients from potential flow methods are added and an elliptic distribution displayed as well. The coordinate system the results are related to is according to Figure 6.1.

The lift distribution of the ALM is in very good agreement with the experimental results for the analysed Reynolds numbers and pitches. It surpasses potential flow methods in this context. The elliptic approximation is an acceptable approach using only a scalar value as reference.

All numerically determined distributions share a declining lift at the wing tip, but the experimental results show a small peak at the outer 5% of the wing. This peak arises

Table 6.3.: Geometric configuration of tapered wing and flow parameters for experiments in [WF58]. Derived values from the experimental description are listed separately.

airfoil section	NACA0015
pitch	$\beta = 8°$
semi-span length	$s/2 = 3\,\text{ft} = 0.9144\,\text{m}$
aspect ratio	$\mathit{AR} = 3$
sweep angle	$0°$
root chord length	$c_{root} = 33.110\,\text{in} = 0.840994\,\text{m}$
mean chord	$c = 24\,\text{in} = 0.610\,\text{m}$
taper ration	$\Lambda = 0.45 = \frac{c_{tip}}{c_{root}}$
planform area	$S = 6\,\text{ft}^2 = 0.557\,\text{m}^2$
dynamic viscosity	$\nu = 1.500 \cdot 10^5\,\text{N s m}^{-1}$ (air, 20°)
density	$\rho = 1.205\,\text{kg/m}^3$
Reynolds number	$\text{Re} = 0.912 \cdot 10^6$
derived values	
inflow	$u_0 = \text{Re}/c \cdot \nu = 22.5\,\text{m/s}$
tip chord	$c_{tip} = 0.3785\,\text{m}$

Table 6.4.: Comparison of lift and drag values of a tapered wing to experimental data in [WF58] for different methods. Diverged results of the LLT are omitted.

	exp.	ALM	LLT	VLM	panel
C_L	0.4125	0.533	–	0.453	0.454
C_D	0.03	0.008 91	–	0.0290	0.0289

from the wake roll up and the resulting downwash, respectively. The potential flow methods include this downwash in their solution and thus the ALM with its correction. An ALM without corrected induced velocity evolves the peak as well, but provides overall an improper distribution.

6.1.2 *Wing deflection*

In this numerical experiment the stationary response of the FSI coupling is validated with an analytic approximation. The setup is a finite, straight and rectangular wing, as used in the experiment in [Jon52]. Since no continuous resulting force distribution of the wing is given, an analytic approximation is required. A solution for this basic flow problem is

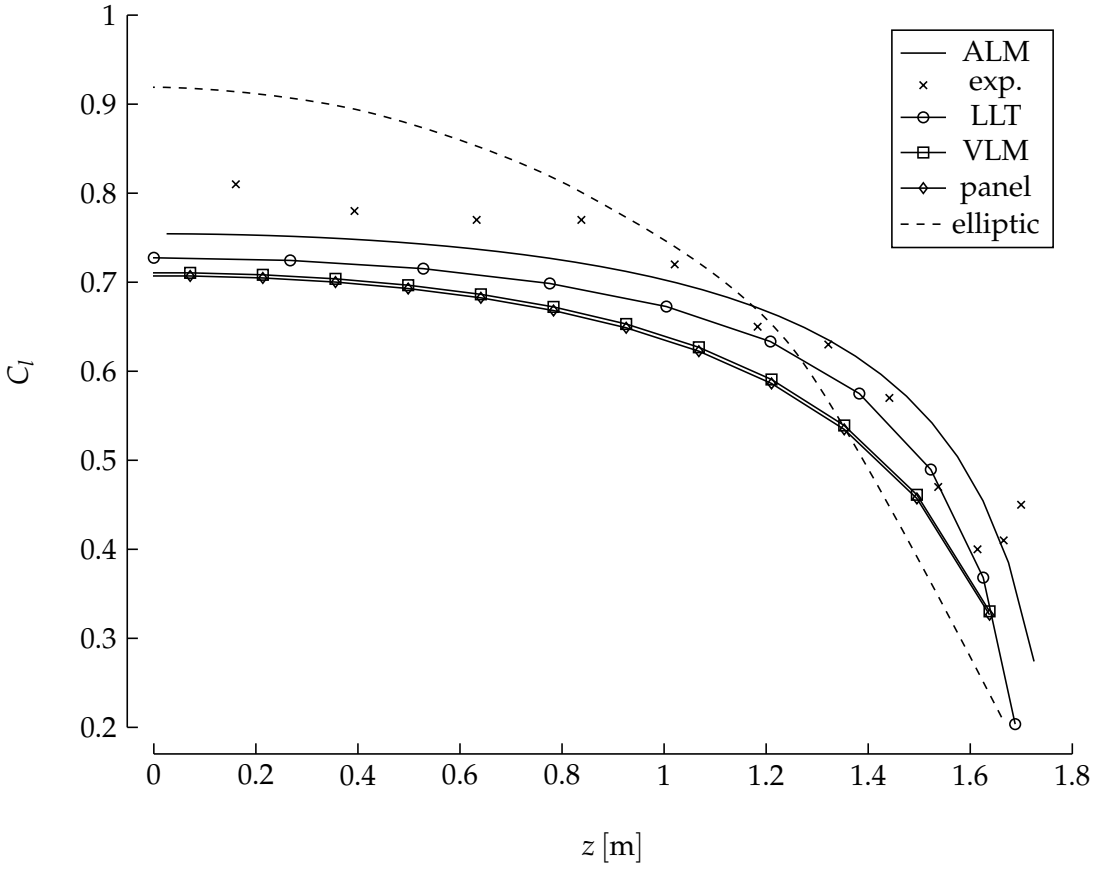

Figure 6.2.: Lift coefficient distribution of wing in parallel flow for different methods compared to experimental data in [MT91] for Re $= 1.5 \cdot 10^{10}$ and pitch 8°. Distribution is plotted against span length. An elliptic distribution is presented scaled with total lift.

approximated with the infinite LLT. The resulting lifting force for a straight wing shows an elliptic distribution.

To complete the approximation of the FSI, the mechanical properties of the wing are represented by beam theory.

The lift force acting on a wing is proportional to the circulation strength Γ generated by the wing in a given flow. According to the analytic solution for a parallel flow in Section 4.2.3 the circulation distribution $\Gamma(z)$ is an elliptic function, defined in Equation (4.21). The local lift force at the position z can be computed from

$$L(z) = \rho u_0 \Gamma(z)\,, \tag{6.1}$$

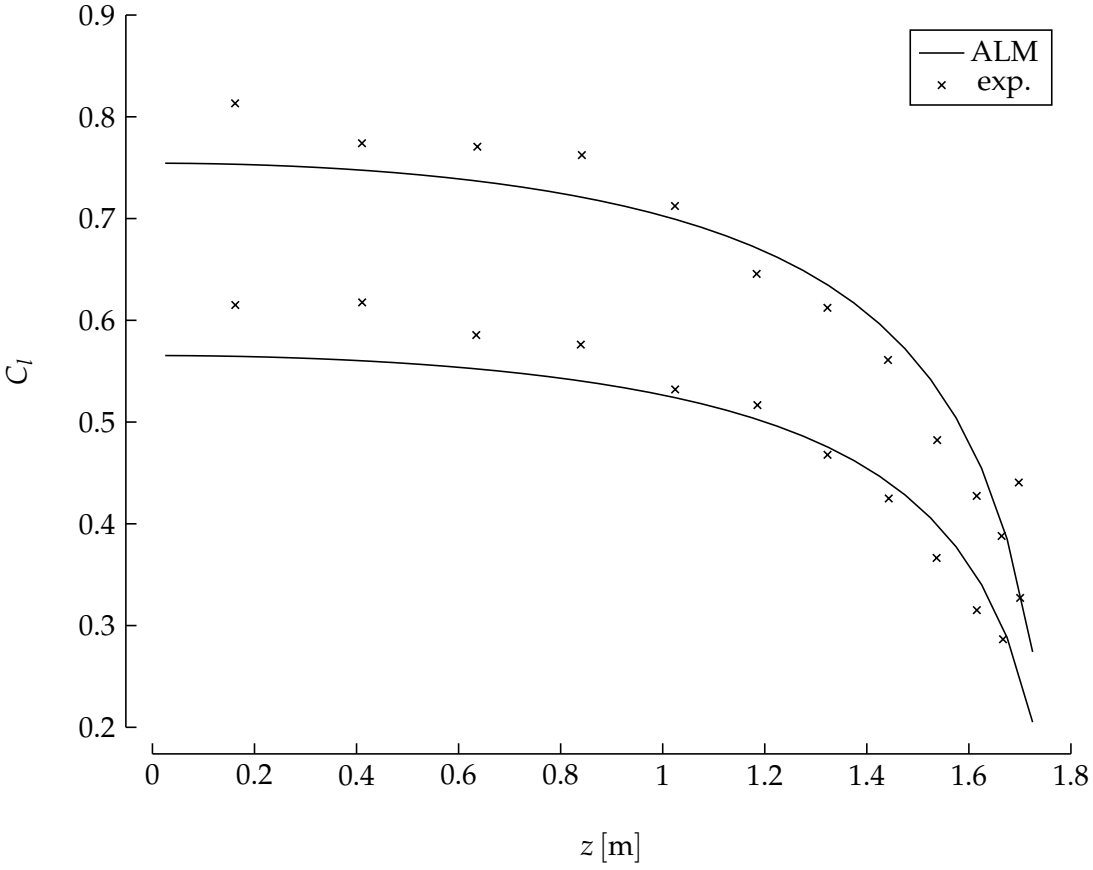

Figure 6.3.: Lift coefficient distribution of wing in parallel flow of the ALM compared to experimental data in [MT91] for $\mathrm{Re} = 2 \cdot 10^{10}$ and pitch 6° and 8°. Distribution is plotted against span length.

see [And85].

The mechanical response of a beam with a distributed load will be approximated by the Euler-Bernoulli beam theory. The bending line of the beam depends on the area moment of inertia, the Young's-modulus, load distribution and boundary conditions. Since the wing is symmetric, only the half of the wing is analysed, thus the lift has to be scaled by $\frac{1}{2}$.

The fourth derivative of the bending line is defined as

$$EIw^{IV} = q(z) = L(z)/2\,. \tag{6.2}$$

After four integrations and inclusion of the boundary conditions for bearing in the middle of the full wing, it yields

$$\begin{aligned} EIw(z) = \frac{k_1}{384} sz(3s^2 + 16z^2) \arcsin\left(\frac{2z}{s}\right) + ... \\ \cdots + k_1 \frac{\sqrt{1 - \left(\frac{2z}{s}\right)^2}(4s^4 + 83s^2z^2 + 24z^4)}{2880} - ... \\ \cdots - \frac{k_1 s\pi z^3}{48} - \frac{k_1 s^4}{720} \end{aligned} \tag{6.3}$$

with

$$k_1 = \frac{2u_0^2 \rho S C_L}{s\pi} \,. \tag{6.4}$$

The resulting bending line for an elliptic lifting load and the results from a simulation with the ALM are shown in Figure 6.4. There, the ALM is coupled with a beam model of a wing and a modal body. The modal body contains a FE model after a model-order reduction. The remaining DOFs are located on a line of nodes.

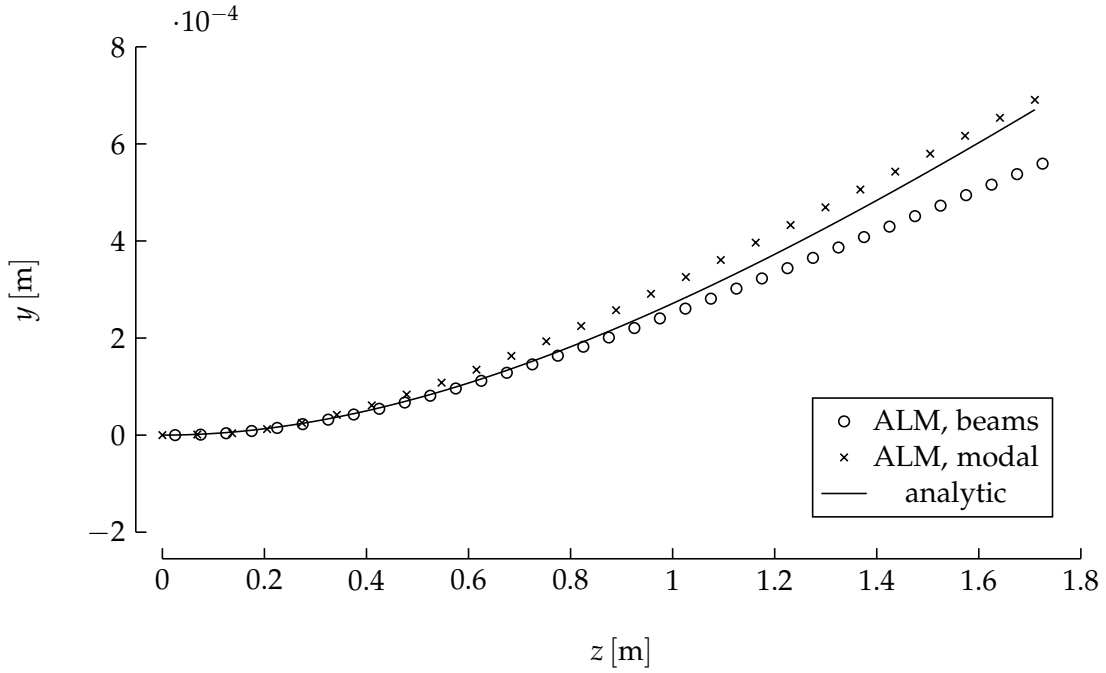

Figure 6.4.: Local deflection in y-direction of wing in parallel flow simulated using ALM in coupling with beams and modal model compared to analytic solution. Deflection is plotted against span length.

Both beam and modal model in the MBS achieve good results compared to the analytic approximation. The modal body is slightly closer to the reference, but the choice of the used modes is crucial. Including too many modes, the error becomes larger by trend.

6.2 VERTICAL-AXIS WIND TURBINE

The aerodynamic properties and dynamic responses of a VAWT are simulated and validated with experimental results. A VAWT is a wind turbine, with the axis of rotation perpendicular to the incoming air flow. In contrast, the axis of rotation of a HAWT is parallel to the inflow. The analysed turbines consists of two and three blades. The displayed setup in Figure 6.5 is a two-bladed VAWT.

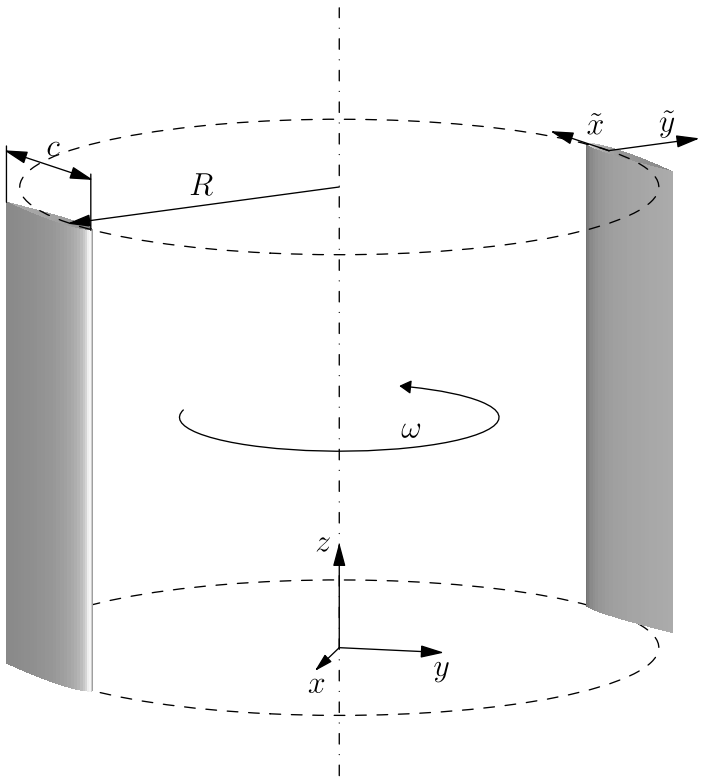

Figure 6.5.: Schematic representation of geometric configuration of vertical-axis turbine. Rotor with two blades and axis of rotation is displayed. Chord length, radius and local coordinate system are marked.

The flow regime of wind turbines is characterised by the so-called tip speed ratio (TSR). It is defined by the ratio between the velocity measured at the wing tip and the free stream inflow,

$$\lambda = \frac{\omega r}{u_0} \,. \tag{6.5}$$

The TSR offers a dimensionless quantity to compare the rotational velocity of wind turbines.

As convention, the rotational position of turbines is defined by the azimuth θ. It is the integral of the rotational velocity,

$$\theta(t) = \int_0^t \omega \, dt \,. \tag{6.6}$$

The 3D setup of the analysed turbines is symmetric with respect to the plane perpendicular to the rotational axis in the middle of the span. The blades are mounted at the quarter chord. The origin of the local coordinate system $(\tilde{x}, \tilde{y})$ is in the quarter chord as well. The turbine rotates about the global z axis and the inflow is perpendicular to this axis.

The validation of the turbine dynamics is split into the comparison of the power outcome and the dynamic behaviour under a gust excitation.

The power outcome is a quasi-steady analysis: a transient simulation is run until the rotor torque of the turbine converges. Thus, the surrounding flow field is assumed to be settled. However, the field is only quasi-steady, i.e. its pattern oscillate with the periodicity of the rotational velocity.

The dynamic validation starts from the quasi-steady state and is superposed with a varying inflow. The inflow velocity is thereby following a sinusoidal function, imitating a gust of wind.

In [DEH13] the power output and gust response of a VAWT are experimental determined and numerically confirmed. The resulting power coefficients and gust response are compared to the results of the methods used in this work. A more detailed analysis of forces acting on a single blade of a VATT are performed in [Wen15] and show very good agreement with the experimental results of [Van78].

Further experimental results are available, such as [Kor+13], however with a TSR of 1.5, which implies large angles of attack and is affected by dynamic stall. Additionally, VAWTs are usually driven in a regime above TSR 3 to reach a high power outcome, compare [Par02].

Nonetheless, simulations of turbines with a TSR smaller than 3 were performed with the methods proposed in this thesis, but inaccurately determine the power output compared to experiments. The angle of attack raises above 15° with a high pitch ratio and thus a dynamic stall model is necessary.

6.2.1 *Power estimation*

Firstly, the power output of a vertical-axis rotor is estimated and confirmed by experimental results from [DEH13]. The setup of the turbine is listed in Table 6.5. The airfoil section of the blades is a NACA0022. The aerodynamic coefficients are determined with XFOIL (see Chapter 4).

Table 6.5.: Geometric and flow parameters of turbine according to experiments in [DEH13].

airfoil section	NACA0022
span length	$s = 0.6\,\mathrm{m}$
chord length	$c = 0.04\,\mathrm{m}$
aspect ratio	$\mathit{AR} = 15$
turbine radius	$R = 0.350\,\mathrm{m}$
number of blades	3
dynamic viscosity (air, 20°)	$\nu = 1.50 \cdot 10^5\,\mathrm{N\,s\,m^{-2}}$
density	$\rho = 1.21\,\mathrm{kg\,m^{-3}}$
Reynolds number	$\mathrm{Re} = 8 \cdot 10^4$

The numerical experiments are performed in a 2D domain. Thus, the blades are represented with one actuator point each.

The section-wise forces are defined per unit span-length and must be scaled to the actual span. Additionally, 3D effects must be accounted for, such as span-wise pressure losses at the wing tip [WLW76]. A scaling factor is determined by computing aerodynamic properties of a wing in a parallel inflow. The static lift and drag values are computed for the given wing geometry with the VLM of XFLR5 in Chapter 4. These are set in relation to the section-wise coefficients of XFOIL. For the linear regime a linear regression is applied (see Figure 6.6) and the slope ratio is taken as scaling factor of $h_{3D} = 0.596$.

The numerical experiment is run near the maximum performance of the turbine, as determined in [DEH13]. The nominal rotational velocity, TSR and the inflow are listed in Table 6.6.

Table 6.6.: Operational parameters and inflow of experiment for power estimation in [DEH13].

nominal rotational velocity	$\omega = 81.1\,\mathrm{rad\,s^{-1}}$
TSR	$\lambda = 4.1$
mean inflow	$u_0 = 6.9\,\mathrm{m/s}$

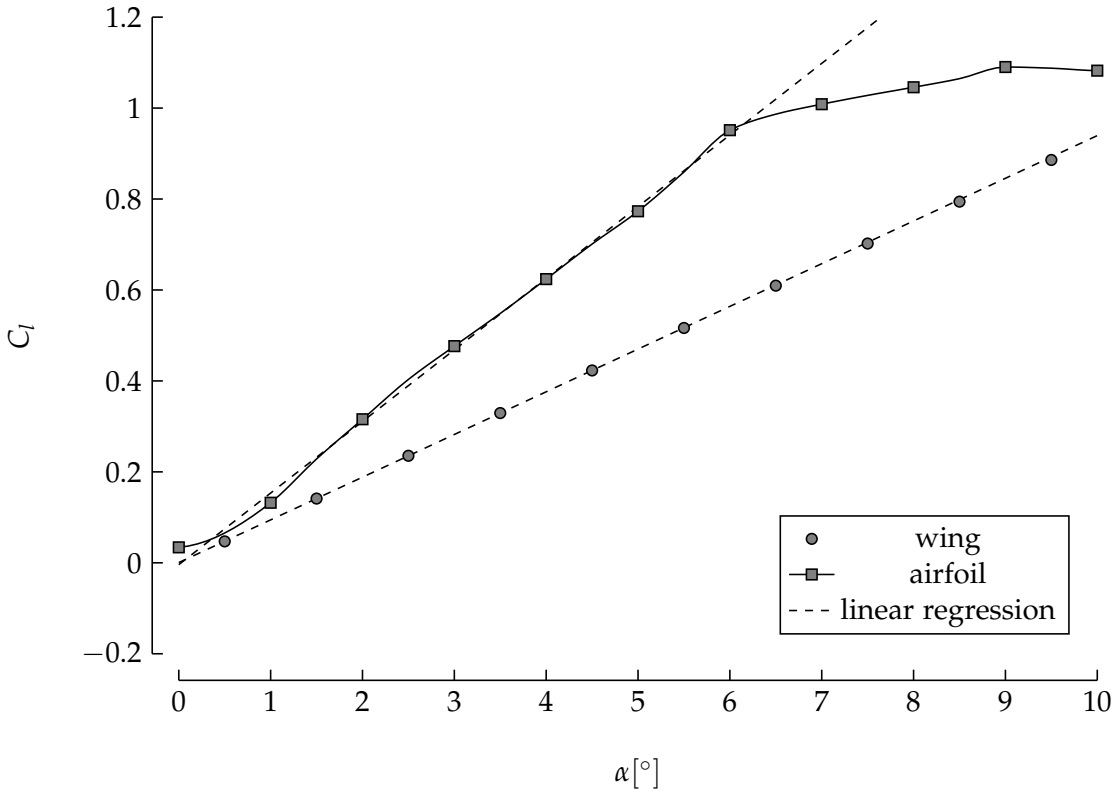

Figure 6.6.: Section-wise lift coefficients of airfoil and wing in experiments of [DEH13] against angle of attack. Linear regressions related to lift coefficients of $0^\circ \leq \alpha \leq 5^\circ$ are plotted.

The simulation is run with the transient solver until a steady state of the power output of the turbine is reached. Two simulations are performed: one with a constant rotational velocity and one with a free running turbine in a coupled simulation with a rigid turbine model. Therefore, the actuator points of the blade can rotate about the turbine centre, all connected to a body with the moment of inertia of the analysed turbine (see Figure 6.7). The coupled FSI simulation allows the turbine to spin free against a certain breaking torque. The torque is manually varied until the mean rotational velocity settles to the nominal value.

In order to study the relative power output of different turbines, a power coefficient C_P is introduced. It is a dimensionless quantity to compare power estimations. The coefficient for the numerical experiments is determined by the time-averaged power output related to the maximum energy of the inflow. The power output is defined as

$$P = \omega \overline{T} \,. \tag{6.7}$$

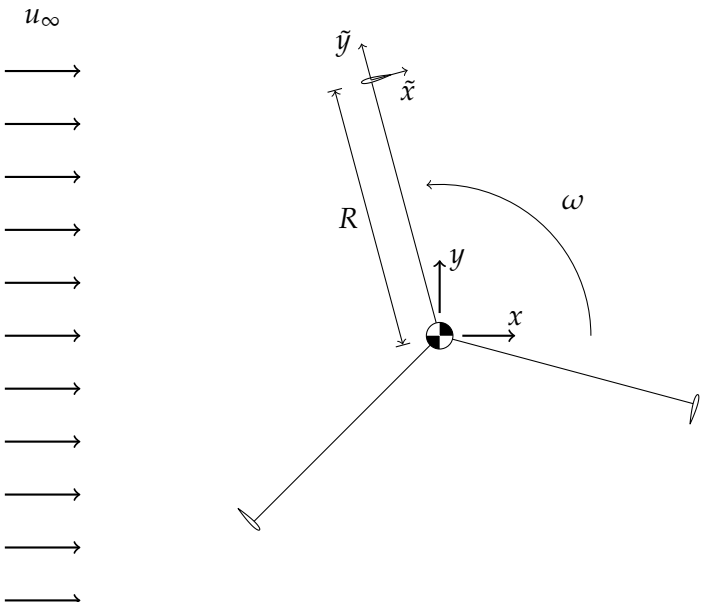

Figure 6.7.: Top-view of schematic rotor configuration of experiments in [DEH13]. Direction of inflow u_∞, sense of rotation, radius and local coordinate system are marked.

The summed turbine torque $\overline{T}$ is integrated and related to the observed runtime,

$$\overline{T} = \frac{1}{t_1 - t_0} \int_{t_0}^{t_1} T \, dt \,, \tag{6.8}$$

where T is the current turbine torque. The energy P_v contained in the inflow is a function of the rotor swept area A_R,

$$A_R = 2Rs \tag{6.9}$$

$$P_v = \frac{1}{2} \rho A_R u_0^3 \,. \tag{6.10}$$

The power coefficient is then

$$C_P = \frac{P}{P_v} \,. \tag{6.11}$$

The resulting power coefficients of experiment and simulation are listed in Table 6.7.

The power estimation of the ALM is in very good agreement with the analysed experimental results. In the simulation with a constant rotational speed the power outcome of the turbine is slightly over-predicted by 4%.

The power coefficient of the free running turbine is different from the constant rotating turbine. Both have the same magnitude and are close to the experimental results, but the FSI simulation estimates a lower power outcome.

Table 6.7.: Numerically determined power coefficients of VAWT compared to experiments in [DEH13] for uncoupled ALM and FSI simulation.

method	C_P	error
exp.	0.199	–
ALM	0.207	4.18 %
FSI	0.190	−4.42 %

The fluctuation of the rotational velocity of the free running turbine is displayed in Figure 6.8 for a small time frame. The amplitude of the fluctuation may vary in a practical application, because the turbine generator can be driven with a ramp characteristic [Hau08].

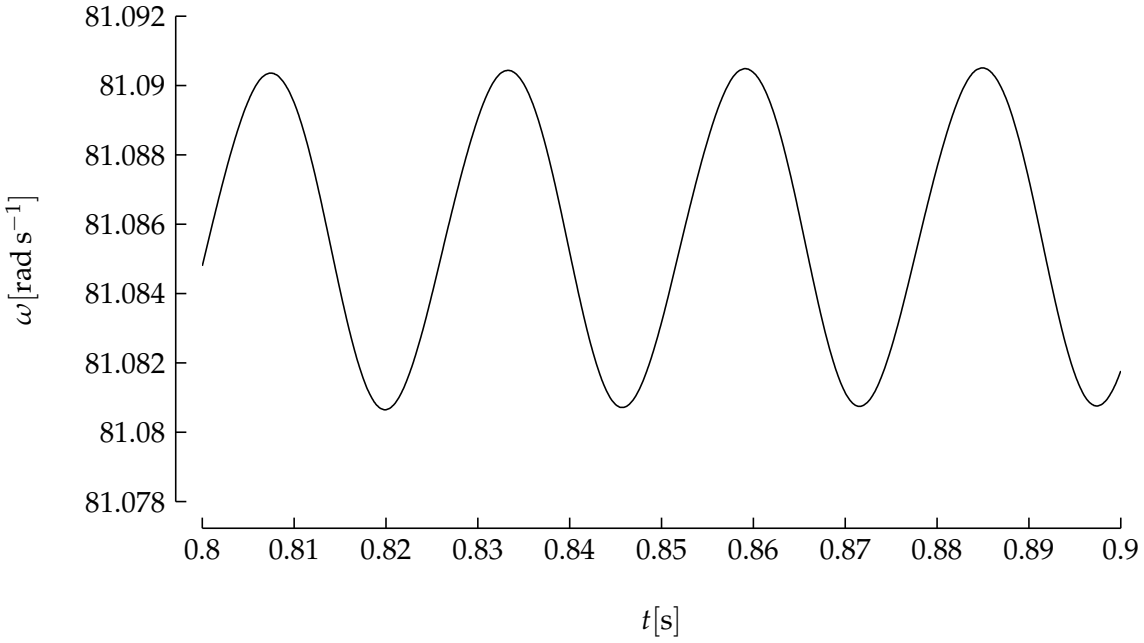

Figure 6.8.: Time dependent rotational velocity of rotor of free running VAWT in numerical simulation for power estimation with configuration according to [DEH13].

The observed difference in the power estimation implies, that a sufficient statement about the expected power output of a turbine cannot only be done with a plain fluid simulation. The variations of the rotor azimuth in the flow field influence the forces

acting on the blades and thus the rotor torque. The rate of the variance is dependent on the rotor's inertia.

Another effect that influences the forces acting on a body, is called *added mass*. It covers the mass inertia of the flow, when a body is moving through the fluid. However, the effect is small for a fluid with a low relative density, [CGN05]; [FWR07], and assumed to be relevant for loose coupling approaches only [BKF12].

6.2.2 *Dynamic response*

The interaction between air flow and the mechanical part of the turbine is a problem of FSI and thus the validation of the used methods requires dynamic experimental results. A series of experiments in [DEH13] provide quantitative results of a dynamic response.

The setup of the experiments for the dynamic response in [DEH13] is the same as for the power estimation in the prior section and listed in Table 6.5.

The free stream flow for the turbine is varied with a harmonic oscillation superposed to a mean inflow of 7.0 m/s. The amplitude of the fluctuation is 12% (see [Dan12]). The parameters of the gust excitation setup are listed in Table 6.8.

Table 6.8.: Operational parameters and inflow for experiments with gust excitation in [DEH13]. Measured rotational variations of experiments are quoted.

nominal rot. velocity	$\overline{\omega} = 791\,\mathrm{rpm} = 82.8\,\mathrm{rad\,s^{-1}}$
mean inflow	$u_0 = 7.0\,\mathrm{m/s}$
inflow fluctuation	$\hat{u} = \pm 0.12 u_0$
measured values	
rot. velocity amplitude	$\hat{\omega} = {}^{+3.15}_{-3.58}$ rpm

The fluctuation of the rotational velocity is shown in Figure 6.9. Additionally, the amplitudes of the fluctuation in the experiments are displayed as horizontal lines. The rotational velocity of the turbine in the numerical experiment is displayed as period-averaged values and as unfiltered values. The filter is a moving average with length of one rotational period. The time axis ranges from 0 to 2π relating to the period of the gust excitation. The results are extracted after the turbine dynamics settle at a quasi-steady state.

The period-averaged velocity shows a good agreement with the experimental margins. The upper peak is very close to the experimental one and the lower peak is slightly above the lower limit of the experiment. The gust reaches its maximum at a period of $\frac{\pi}{2}$ with the maximum acceleration of the turbine. The same holds for the gust minimum and the maximum deceleration at $\frac{3\pi}{2}$.

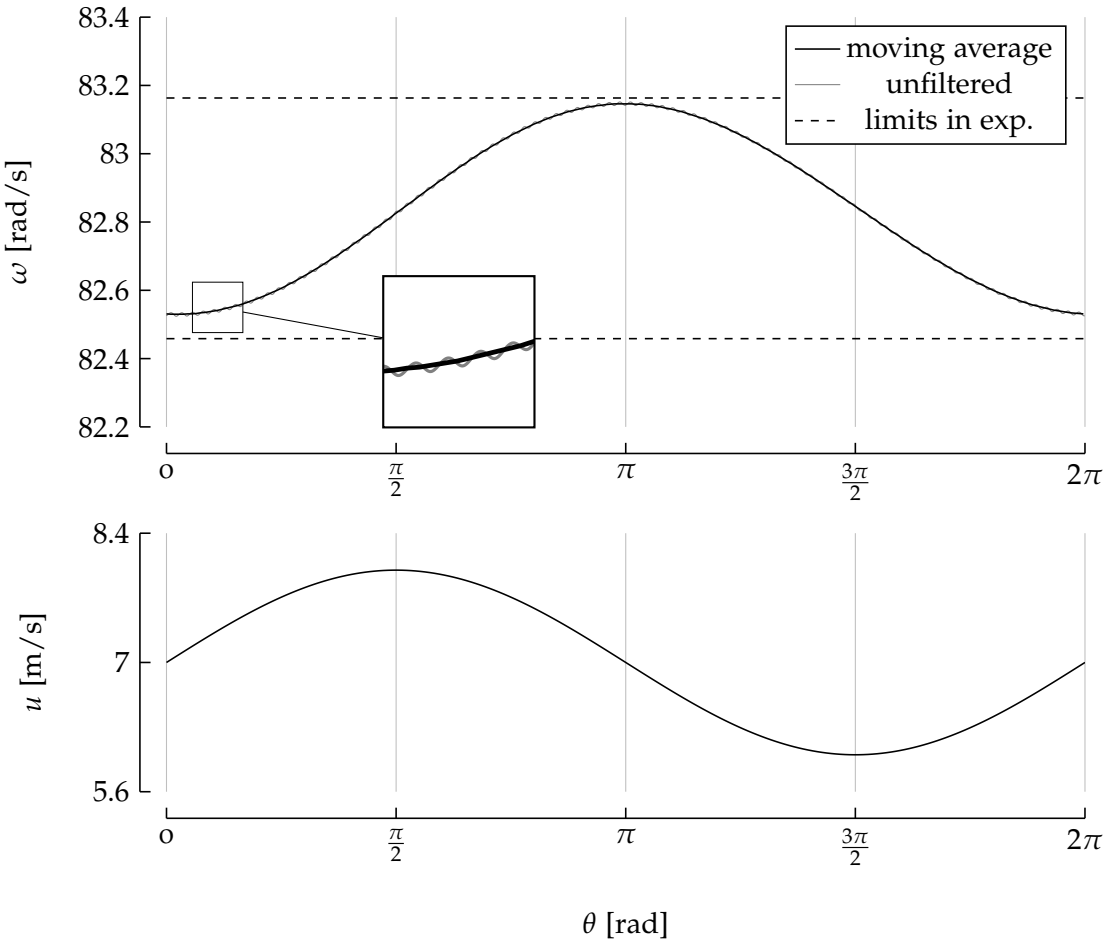

Figure 6.9.: Fluctuation in rotational velocity of one gust period resulting from gust excitation in numerical experiment. Limits of fluctuations in experiments of [DEH13] are marked by horizontal lines. Gust excitation is displayed in the lower plot.

6.3 VERTICAL-AXIS TIDAL TURBINE

The structural layout of a VATT rotor is identical to the VAWT and thus the estimation of the power output. The fluid medium is water and has a different density and viscosity compared to the prior numerical experiments. Thus, further validation of power estimation in a water domain is performed in this section. In terms of FSI, the density ratio between the fluid and solid domain has a large influence on the dynamics and leads potentially to the necessity of two-way iterations (see Chapter 5).

The power outcome of a VATT is experimental determined in [Hil83] for a range of TSRs. The turbine parameters are listed in Table 6.9.

Table 6.9.: Parameters of the turbine geometry and flow regime for the experiments in [Hil83].

airfoil section	NACA0015
span length	$s = 2.4\,\mathrm{m}$
chord length	$c = 0.185\,\mathrm{m}$
turbine radius	$R = 1.50\,\mathrm{m}$
number of blades	3
solidity	0.18
dynamic viscosity (water, 20°)	$\nu = 1.002 \cdot 10^{-6}\,\mathrm{N\,s\,m^{-2}}$
density	$\rho = 1 \cdot 10^{3}\,\mathrm{kg\,m^{-3}}$
inflow	$u_0 = 0.6\,\mathrm{m/s}$
average Reynolds number	$\mathrm{Re} = 3.50 \cdot 10^{5}$
TSR	$\lambda = 3, \ldots, 5.25$

The aerodynamic coefficients of the airfoil are extracted from experimental results in [SK81] for the averaged Reynolds number. Again, the 2D results are scaled to include 3D power loss effects.

6.3.1 *Power estimation*

A power estimation is performed for a range of TSRs from 3 to 5.25 with 0.25 steps. The coefficients of the numerical experiments and the experiments in [Hil83] are plotted against the TSR in Figure 6.10. Beside the 2D simulations, a simulation for one TSR is carried out in 3D and the resulting power coefficient plot in the figure as well.

To provide an orientation, the results of a linear analysis with a DST model are plotted. The basis of the DST simulation is the same table of aerodynamic coefficients as for the ALM.

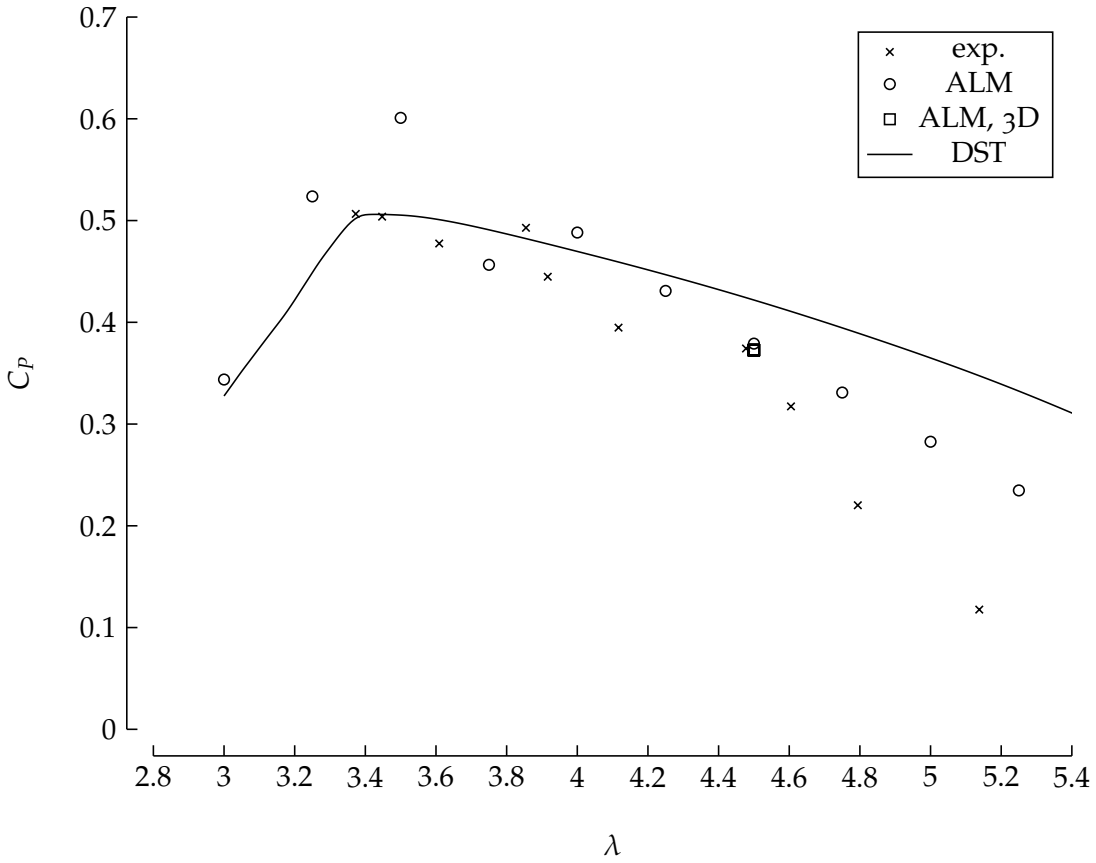

Figure 6.10.: Power coefficient against TSR of ALM simulation compared to experimental results in [Hil83] and the DST model. Single result of 3D simulation is drawn in for TSR of 4.5.

The results of the ALM simulation of the VATT are in good agreement with the experimental power coefficients. For the TSR of 3.5 the ALM over-predicts the power outcome of the turbine in the experiment. However, for TSRs above 3.5 it stays close to the experiments and gives better results than the linear model, especially for high TSRs.

The comparison between 2D and 3D power coefficient validates the scaling factor. The power coefficient for $\lambda = 4.5$ in 2D is 0.385 and 0.373 in 3D, which is a very good agreement and close to experimental data. For comparison, the DST predicts a power coefficient of 0.422 and linear theory 0.431 at a TSR of 4.5 and thus over-estimates the power outcome.

In this chapter a validation of all including elements of the FSI simulation is performed. At first quasi-steady aerodynamic properties of wings are validated with the experiments of [MT91]. The quasi-steady deflection of a flexible wing in a FSI coupling based on both

an order-reduced model and beam elements, is validated with an analytic solution. All quasi-steady results show sufficient agreement with the references. The power estimation for both VAWTs and VATTs are in good agreement with available experimental data from [DEH13] and [Hil83]. A dynamic validation of the FSI coupling is referred to results of [DEH13]. The dynamic response of the VAWT matches the results from the experiment. Thus, the FSI approach is validated and prepared for an advanced application.

7 APPLICATION

In Chapter 5 an approach to solve FSI problems is depicted and the validity of resulting forces and dynamics sufficiently confirmed in Chapter 6. In this chapter an application of the outlined methods is performed with a VATT in a 3D simulation.

Similar simulations are carried out in [Baz+14] for a VAWT with a flexible tower. For an air domain the blades are relatively rigid, but for water the forces acting on the blades become larger compared to air. In the following simulation a turbine with flexible blades will be simulated in a water domain and the resulting deflection of the blades analysed. Considering the density ratio and the resulting magnitude of the blade deflection, the setup defines a strong FSI.

7.1 FLUID-STRUCTURE INTERACTION OF VERTICAL-AXIS TIDAL TURBINE

The analysed turbine is a VATT with a configuration used in the experiments of [Hil83] (see Table 6.9). The material of the blades is assumed to be glass-reinforced plastic (GRP) as employed in the experiments, but without the mentioned tubular reinforcements. The Young's-modulus for the GRP is extracted from [Sch07].

The 3D setup is sketched in Figure 7.1. The analysed turbine is a H-type VATT, i.e. the straight blades are mounted to the rotational axis in the midspan with a rigid rod. The symmetry plane is in the midspan as well.

The blades are represented with 39 beam elements. The area moment of inertia is determined for a hollow NACA-type airfoil with 2 mm wall thickness. The parameters are summarised in Table 7.1. The local coordinates for the area moments of inertia are displayed in Figure 7.1. The area moment I_x refers to the $\tilde{x}$ axis and specifies the flap-wise bending and I_y the chord-wise, respectively. The Young's modulus is chosen for a parallelly loaded cases of an orthotropic reinforced part.

The fluid domain and its respective mesh is displayed in Figure 7.2. The domain spans $27 \times 18 \times 9$ m with the origin in the turbine centre. The boundary of type inlet is a Dirichlet boundary condition with a defined inflow for the velocity and a Neumann boundary condition with a zero gradient for the pressure. The outlet has vice versa a zero gradient in velocity and is zero for the pressure. The walls are zero for the velocity and zero gradient for the pressure. The displayed viewport area in Figure 7.2 is the symmetry plane.

The fluid side is simulated with a k-ω-SST turbulence model (see Chapter 4). The aerodynamic coefficients in the ALM are extracted from [SK81].

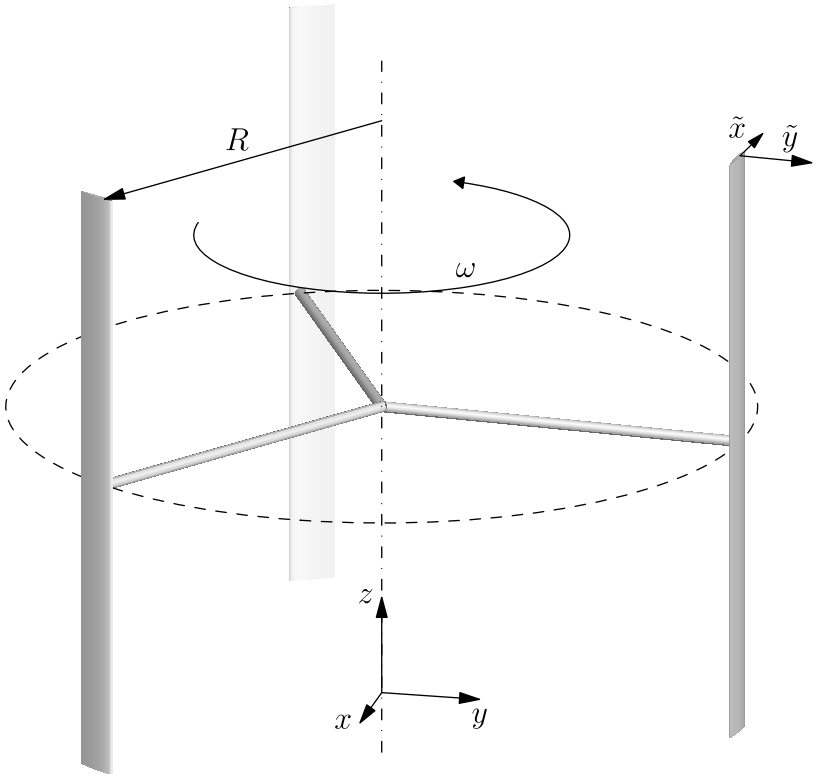

Figure 7.1.: Geometric configuration of turbine for 3D FSI simulation with symmetry plane and sense of rotation. Global and local coordinate system are drawn in.

The simulation is run with a time step of $\Delta t = 1 \cdot 10^{-3}\,\mathrm{s}$. The nominal rotational velocity of the turbine's rotor is blended in to avoid steep initial states. It starts from rest at $t = 0.100\,\mathrm{s}$ and accelerates to the nominal value at $t = 0.200\,\mathrm{s}$.

The computation is performed on a single dodeca-core E5-2680v3 Intel Xeon® processor. The computational time is 180 hours for a simulation time of 37 s, which are about 10 revolutions of the turbine. The average iterations per time step are 27.1 and the average computational time per rotation 18 hours. For comparison, an uncoupled, 2D unsteady Reynolds-averaged Navier-Stokes (URANS) simulation of a VAWT in [Dan12] requires 135 hours per rotation on 12 cores.

Table 7.1.: Structural and material parameters of blades for FSI simulation.

material	GRP
Young's modulus	$E = 4.52 \cdot 10^{10}\,\mathrm{N\,m^{-2}}$
shear modulus	$G = 5.60 \cdot 10^{9}\,\mathrm{N\,m^{-2}}$
airfoil	NACA0015
area moments of inertia	$I_x = 5.53 \cdot 10^{-8}\,\mathrm{m^4}$
	$I_y = 4.18 \cdot 10^{-7}\,\mathrm{m^4}$

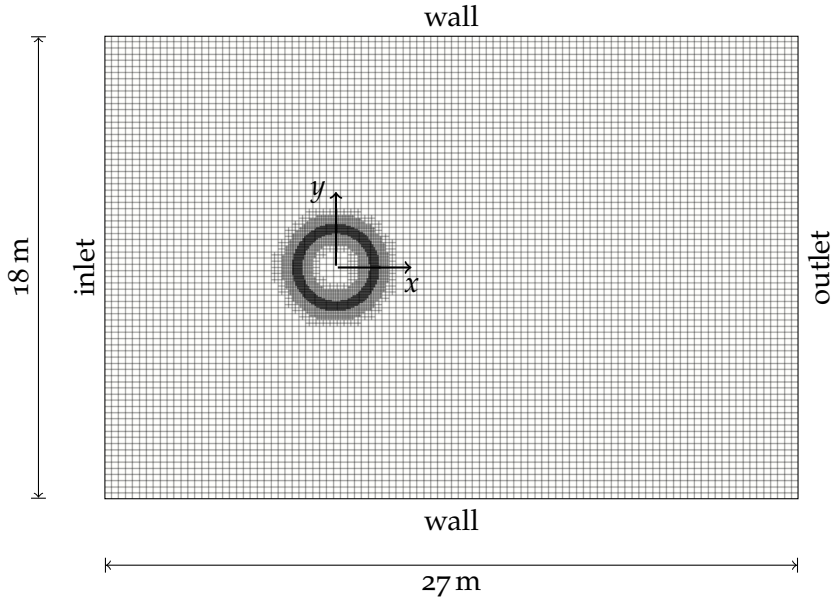

Figure 7.2.: Side-view in z-direction of mesh for FSI simulation with boundaries. Three types of boundary conditions and origin of control volume are marked.

The resulting deflections of the beam elements are mapped onto to the blade bodies and displayed in Figure 7.3. The states are extracted after a runtime of 30 s for distinct azimuths. The blades deflect up to 0.0500 m, which is 27% of the chord length.

The largest blade deformations are at positions, where the blade stands perpendicular to the inflow. The deflection is large at the upstream side at 270°, but also in the area of the downstream wake between 90° and 180°.

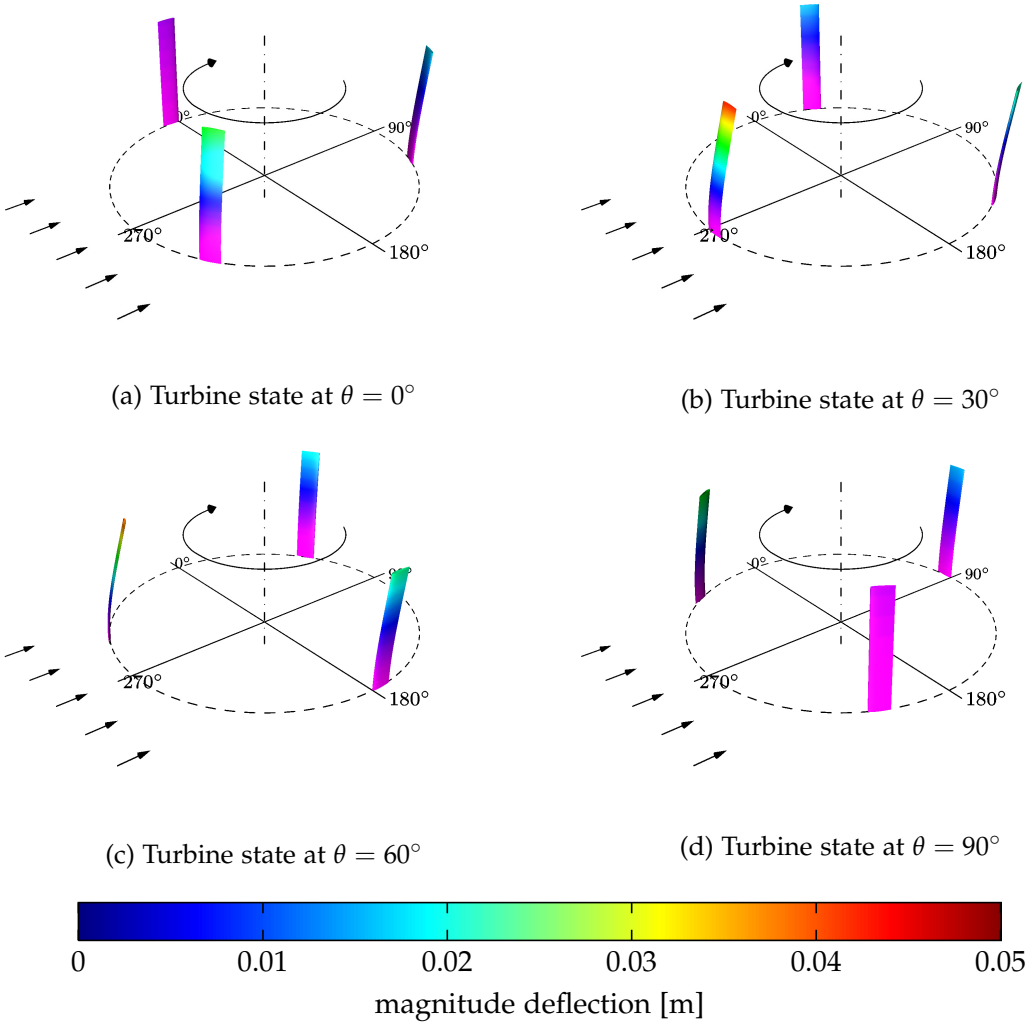

(a) Turbine state at $\theta = 0°$

(b) Turbine state at $\theta = 30°$

(c) Turbine state at $\theta = 60°$

(d) Turbine state at $\theta = 90°$

Figure 7.3.: Deflections of rotor blades in FSI simulation at four azimuth positions from 0° to 90° in Figures (a) to (d). Direction of inflow is outlined and magnitude of local blade deflections represented according to colormap.

7.2 COMPARISON TO LINEAR THEORY

The effect of wake interactions is visible by comparing the deflection of the beams to a linear solution of VATT dynamics. A linear simulation is performed with the same mechanical setup of the turbine as in the coupling with the ALM but in connection with a BET. The underlying table of aerodynamic coefficients is the same in both simulations.

In Figure 7.4 the trajectory of a wing motion is displayed. The trajectory is generated from the wing tip position of the first blade in a quasi-steady flow field. The orbit of the trajectories is closed and affirms the settled system state. Both the trajectory of the coupling with the ALM and the linear approach are displayed.

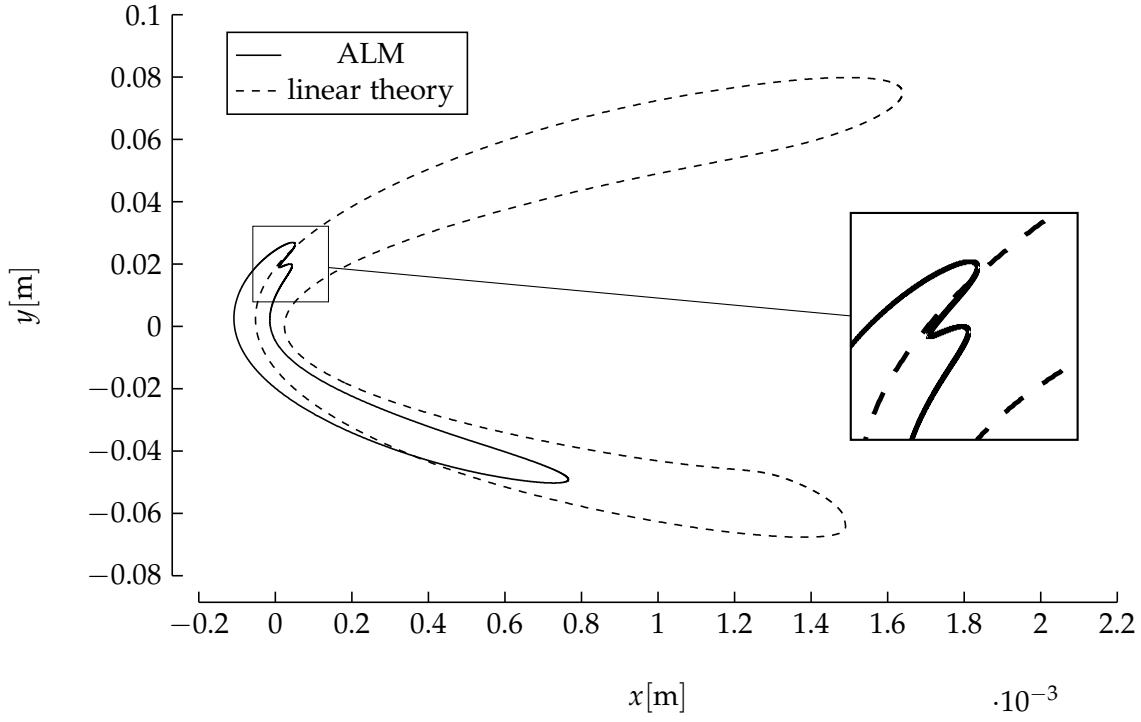

Figure 7.4.: View in z-direction on trajectory in local coordinates of wing tip of first blade starting at $t = 20.2\,\mathrm{s}$ compared to linear simulation of FSI. Magnification on right-hand side points out blade tip deflection near $\theta = 125°$.

The deflection of the linear theory are larger than the ALM, as are the power estimation, compare Section 6.2.1. Additionally, the simulation with the ALM shows a stronger asymmetry in the bending in y-direction, which separates the up- and downstream side. Positive values are thereby deflections in the downstream. Here also a small kink caused by the shed wakes is visible, see magnification in Figure 7.4.

The kink can be explained be reviewing the wake structure. The flow field of the turbine at an azimuth of $\theta = 125°$ is illustrated in Figure 7.5 with aid of velocity streamlines circulating around the deflected blades. An isosurface of the λ^2-criterion represents the vorticity in the flow.

The front blade in the depicted turbine state is located between to vortices: the wake of the previous blade and its own shed wake. The collocation of these two vortices clarifies the changing load on the blade, visible in Figure 7.4. During the rotational motion, the blade experiences a load when shedding its wake. In the next position, it hits the wake of the previous blade. Between these two wakes extinction can occur and thus a temporally reduced blade load.

7.3 COMPARISON TO ONE-WAY APPROACH

A further computation is executed with weak coupling. The used Young's modulus for this simulation is chosen from omnidirectional reinforced GRP of $1.72 \cdot 10^{10}\,\mathrm{N\,m^{-2}}$. The remaining parameter are the same as in Table 7.1.

For this setup the one-way approach tends to diverge in the runtime of the simulation. The computed forces alternate from one to another time step. The resulting blade deflection differs from the two-way coupling, visible in Figure 7.6. The deflection of the wing tip is more than 10% higher in the one-way iterations. This is in agreement with the considerations of added mass, see Section 6.2.1.

However, reviewing the computational time, the one-way coupling performs significant faster than the two-way: an average step number of 3.3 compared to 27.1. But the forces potentially diverge for a blade stiffness of the given numerical experiments. Nonetheless, the resulting deflections for stiff blades of one- and two-way coupling are comparable.

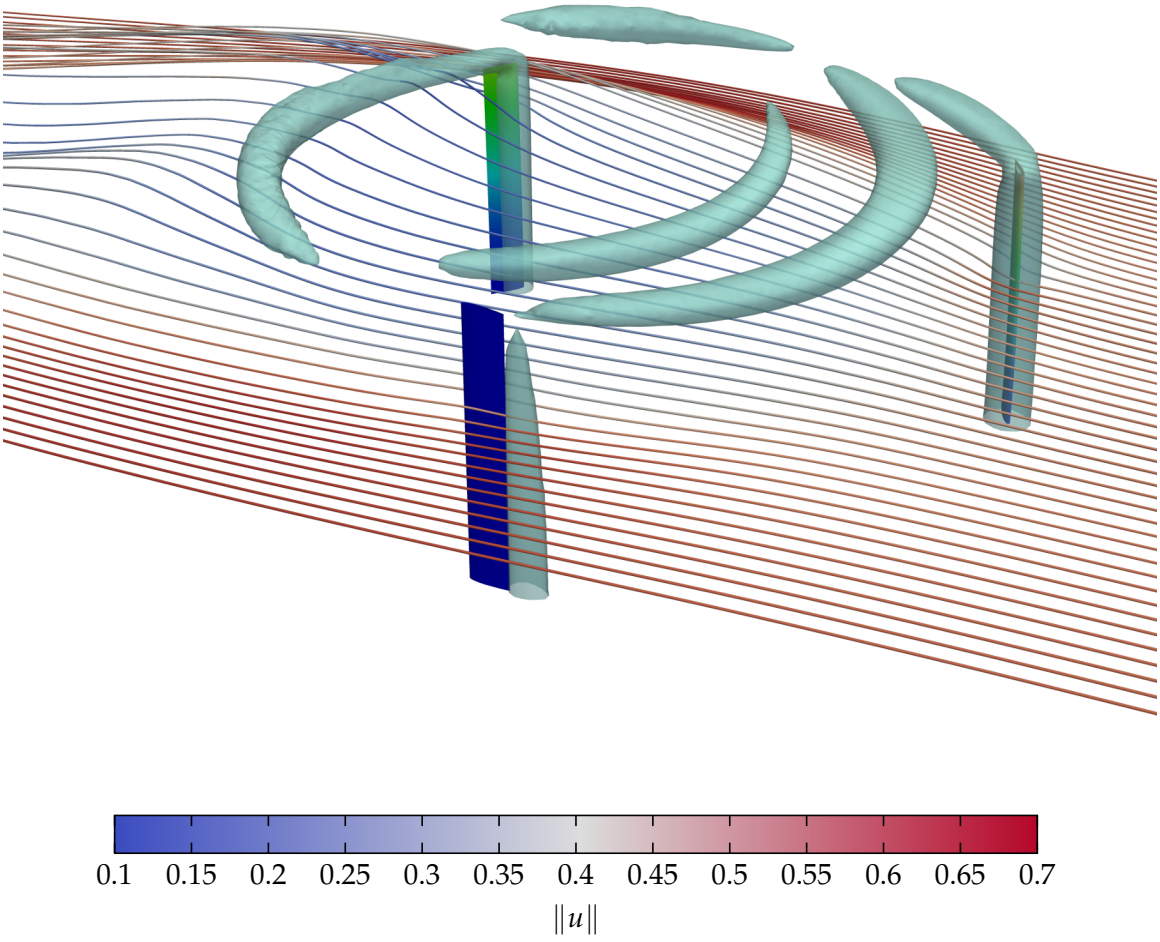

Figure 7.5.: Flow field of turbine at $\theta = 125°$ visualised by velocity streamlines starting from equidistant sources in upstream on right-hand side. Colouring of streamlines depicts magnitude of local velocity according to attached colormap. Vorticity represented by an isosurface of λ^2-criterion. Magnitude of blade deflection coloured according to Figure 7.3

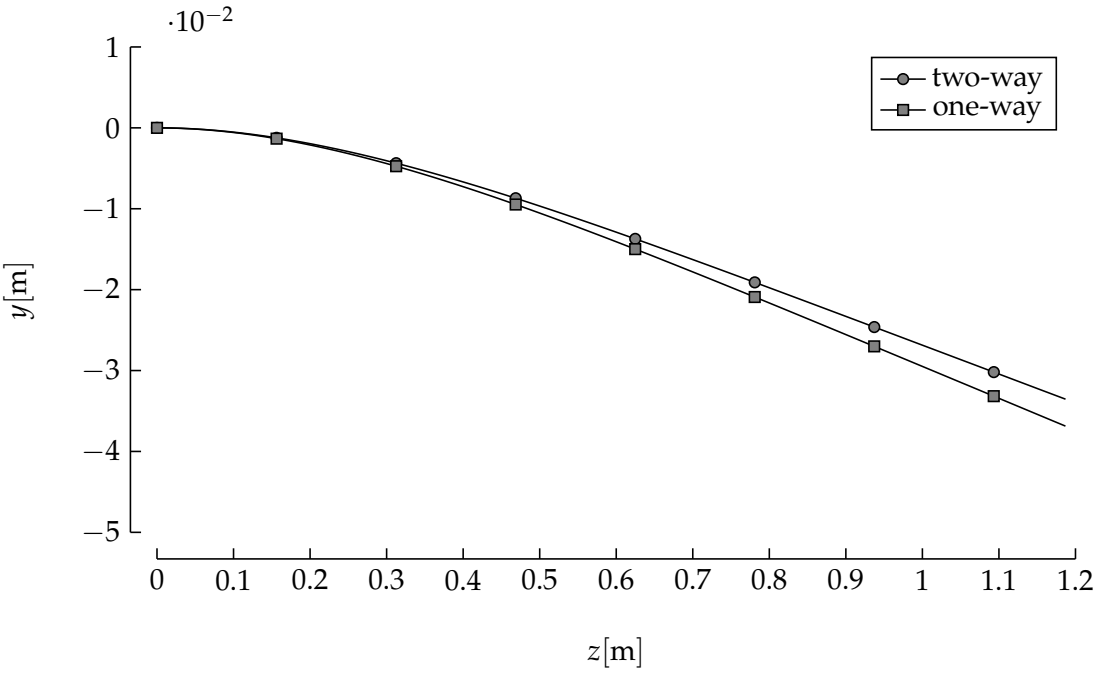

Figure 7.6.: View in x-direction on deflection in local coordinates of first blade at $t = 1.46\,\mathrm{s}$ and $\theta = 225^\circ$ for one- and two-way coupling in FSI simulation. Deflection in y-direction is plotted against span length.

A numerical experiment of a VATT with flexible blades was performed in this chapter. The resulting deflection examined and compared to a linear solution. The deformation of the blades in the ALM simulation are smaller than from linear theory. A significant difference is visible in the effects of wakes on the blades. A further comparison between one- and two-way approach of FSI shows a difference in the resulting deflection, which increases for blades with a lower stiffness.

The numerical experiment demonstrates, that the depicted methods allow to predict blade deflection of VATT in 3D with a realistic computational effort.

8 SUMMARY AND CONCLUSIONS

In the initial stage of this work, a solution for numerical simulation tasks of vertical-axis turbines was requested. These tasks include the aerodynamic and mechanical responses of vertical-axis wind turbine (VAWT) and vertical-axis tidal turbine (VATT). The coupled simulation of fluid and body side states a fluid-structure interaction (FSI) problem.

In order to accomplish a solution of the FSI problem, model based approaches were utilised for both domains. The fluid side of the problem is represented by an actuator-line method (ALM) implemented by Wenzel [Wen15] in the OpenFOAM framework. The ALM enables the analysis of lifting bodies including turbulent wakes without the necessity of extensive meshing.

The mechanical side describes the motion and deformation of a body exposed to external forces. The solution was realised using the multi-body system (MBS) library MBDyn. Flexible bodies are represented with either beam models or so-called modal bodies. The latter consists of a modal decomposition of the body dynamics. The dynamics are resolved with a finite-element method (FEM). For the purpose of reducing computational time the resulting FEM model is reduced considering the order of degrees of freedom with a model order reduction (MOR) technique.

The two domains were connected with a FSI method. A partitioned approach with a two-way coupling was equipped. The solvers of each domain are called sequentially and results are inserted iteratively until the solution converges to a fixed point. The convergence was accelerated with methods based on approximations of Jacobian matrices. The performance of these so-called quasi-Newton schemes was compared with other relaxation schemes. For stiff problems the quasi-Newton methods achieved fast convergence rates.

Beside the two-way approach a monolithic method was implemented in the MBS framework using a panel code. The implementation showed the advantages and limits of this approach. Since the MBS solver is not optimised for a large amount of degrees of freedom, this implementation was dismissed.

All embedded elements of the FSI simulation were validated. Static and dynamic results of the fluid and the MBS solver were compared to experimental results and analytic solution.

An improved version of the ALM [Wen15] was used to resolve the flow field of a flexible wing in steady parallel inflow. Both two- and three-dimensional results showed good agreement with experimental data. In quasi-steady setups vertical-axis turbines were run

with a constant rotational velocity and numerical results were compared to experiments. An accurate prediction of the power output based on the simulation was affirmed. A comparison with a simulation of a free running turbine implies that the power estimation in practice requires for the treatment of FSI.

In order to approve the accuracy of the FSI coupling, the dynamic behaviour of a VAWT was examined. The turbine was loaded with varying inflow and resulting fluctuation in the rotational velocity was observed. The fluctuation was in agreement with the referenced experiments.

Conclusively, the depicted numerical FSI approach was applied to a VATT with flexible blades. The deflections of the blades were analysed and compared to the solution of basic methods. A one-way approach and linear methods tend to over-predict the blade deflection. The two-way coupling provides reasonable results and an accurate blade deflection due to wake-body interaction was computed.

The depicted methods were able to solve the tasks derived from the initial motivation in this thesis. The completed FSI approach accurately simulates the validation problems with reasonable computational costs. Compared to fully meshed solutions, the approach performs several orders of magnitude faster. With the developed simulation tool chain, two goals were achieved: the ability to *optimise turbine designs* and *develop new energy converters*.

The first step for optimisations of a VATT was done in Chapter 7 and the advantage of the implemented methods was depicted. The two-way coupled FSI with an ALM allows an improved fine resolution of blade deflection compared to the results of a linear theory and a one-way approach. Consequently, the expected loads and deflections were determined to be smaller. The structural dimensioning of a rotor depends on the calculated loads and deflections. Since available methods tend to over-estimate loads and deformation, the optimum in material and power outcome was not achieved so far. The new results of the FSI approach allow exploitation of the maximum capacity of the structure and therefore increase the utilisation factor and save material.

Another part of turbine optimisation concerns operational parameters. These are first of all the global blade pitch, which is controlled in dependency on the varying inflow. The controller strategy must be balanced between fatigue loads and power outcome. A detailed resolution of the loads with the FSI allows an accessible tuning of this trade-off. An extension of the global blade pitch is a cyclical pitch variation for VAWTs. Blade-wise pitching, however, adds further parameters to the optimisation problem. The utilised MBS approach allows a straightforward implementation of actuators and thus a study of parameters necessary for pitch optimisation. Current publications show that optimised control can increase the power outcome significantly [PAH15]. In combination with the structural optimisation this reveals an increase in the economic and energetic efficiency of the analysed turbines.

With aid of the optimisation, the competitive position of currently unexploited turbine concepts like the vertical-axis turbine can be raised to the level of horizontal-axis turbines. Furthermore, already established concepts such as horizontal-axis wind turbines (HAWTs) can be optimised considering blade loads.

The second achievement is the ability to develop new energy converters. The demands on the simulation tools are high due to the complexity. Emerging concepts harvesting ocean energy often include fluctuating boundary conditions and loads. The ability of the FSI approach to resolve such configurations was successfully shown in Chapter 6.

Beside the technical demands the assembled tool chain serves economic requirements. Projects realising new concepts using undeveloped sources of renewable energy profit from preservative economic and computational costs of involved simulation tools. The software elements used by the methods depicted in this thesis are open source and the final FSI approach is conservative in hardware requirements and computational time.

FUTURE WORKS

With the developed simulation framework a fast and accurate representation of turbines is possible. The next step is a practical application to tasks in the design process of turbines. In this context, a detailed validation of blade deflections would be possible and necessary.

A limitation of the current implementation is the sensitivity to the flow regime. The Reynolds number is set a priori and generated according to aerodynamic coefficients for the blade geometry. For strongly varying inflows the coefficients should be chosen adaptively from precomputed coefficients for a range of Reynolds numbers. The stability of this approach must be verified.

An obvious extension of this FSI framework is the application to HAWTs, which the ALM is already utilised for [SS02]. This allows examining the dynamics of wind turbines including blade elasticity with interaction of multiple turbines through wake shedding. Additionally, detailed experimental results are available in this field and should be validated, such as the blade deflection in [Ban+13].

Leaving the field of energy generation and regarding propulsion, two concepts come into focus: the Voith-Schneider propeller as equivalent to a VATT and a helicopter rotor similar to a HAWT. The latter is currently a subject of research, which the development FSI approach in this thesis can be applied to. The dynamics are dominated by wake-body interaction and subsequent unresolved questions [Del14]. Both propulsion systems include blade-wise pitch variation and high loads on the structure. The ability to simulate these problems with the depicted methods can be verified and adaptations made.

APPENDIX

A FLUID DYNAMICS

A.1 NACA AIRFOIL SECTIONS

For the NACA-ooxx series the airfoil section distribution is defined in Equation (A.1) [JWP33]. The corresponding coefficients are listed below. For a section with a trailing edge of zero thickness the last coefficient becomes $a_4 = -0.1036$.

$$a_0 = 0.2969, \qquad a_1 = -0.1260$$
$$a_2 = -0.3516, \qquad a_3 = 0.2843$$
$$a_4 = -0.1015$$

$$y(x) = \frac{d}{0.2c}\left[a_0\sqrt{\frac{x}{c}} + a_1\left(\frac{x}{c}\right) + a_2\left(\frac{x}{c}\right)^2 + a_3\left(\frac{x}{c}\right)^3 + a_4\left(\frac{x}{c}\right)^4\right], \tag{A.1}$$

with the airfoil thickness d.

A.2 POTENTIAL FLOW METHODS

The difference between a infinite and finite lifting wing mainly derives from the downwash caused by the wing tip vortices. As first to mention is Prandtl and Betz, who described the losses on a finite wing in his papers on hydro- and aerodynamics, [PB10].

With potential flow methods a simplified approach to the question of wing aerodynamics is provided. The assumptions made therefore are that the fluid is incompressible, inviscid and irrotational.

A.2.1 *Lifting-line theory*

The lifting-line theory (LLT) allows approximating aerodynamic properties of a finite wing on the basis of certain distribution of a circulation strength along the span. The distribution derives from the shed vortex lines downstream of the wing.

A.2.2 *Vortex lattice method*

The vortex lattice method (VLM) is an 2D extension of the LLT. Instead of a vortex line a discrete number of horseshoe elements are used. The method is similar to the panel method, but the VLM is defined for thin lifting bodies only.

B

ALGORITHMS

B.1 NEWTON-RAPHSON METHOD

The Newton-Raphson method solves root-finding problems stated as $\mathbf{f}(\mathbf{x}) = \mathbf{0}$. The multidimensional formulation for a function $\mathbf{f} : \mathbb{R}^n \to \mathbb{R}^n$ at convergence step k yields

$$\mathbf{x}^{k+1} = \mathbf{x}^k - \mathbf{J}^{-1}(\mathbf{x}^k)\mathbf{f}(\mathbf{x}^k) \tag{B.1}$$

$$\Delta\mathbf{x}^k = -\mathbf{J}^{-1}(\mathbf{x}^k)\mathbf{f}(\mathbf{x}^k)\,, \tag{B.2}$$

with $\mathbf{x} \in \mathbb{R}^n$ and the Jacobian matrix $\mathbf{J} = \left(\frac{\partial f_i}{\partial x_i}\right)$.

C MECHANICS

C.1 AREA MOMENT OF INERTIA

The area moment of inertia, also called second moment of area is the integration of a relative distance over the section area A,

$$I_y = \int_A z^2 dA \tag{C.1}$$

$$I_z = \int_A y^2 dA\,. \tag{C.2}$$

C.2 THREE-BLADED VATT MODEL

Listing C.1: MBDyn input file `vawt_hilton_3wings_3d.mbd`

```
### circle steering of 3 wings, const rotation
#   z position in blade intervall center

set: real AOA = -0.0*deg2rad;              # pitch
set: real radius = 1.500000;               # radius [m]
set: real initalpha = -90.0*deg2rad;       # initial angle on circle
set:  integer N = 3;                       # blades per rotor
set:  integer Nz = 39;                     # number slice in z
set:  integer N_curr;                      # current slice number
set:  integer N_blade;                     # current blade number
set: real WING_START = 0.007812;           # start z-position
set: real WING_END = 1.195312;             # end z-position
set: real SPAN = WING_END-WING_START; # blade length
set: real dL = SPAN/Nz;                    # local variables
set:  integer BLADE;
set:  integer CENTER;
set:  integer BEARING;

set: real FADEIN_END = 0.2;           # time to fade in rotation
set: real FADEIN_START = 0.1;
set: real OMEGA = -1.800000;            # rotational speed
set: real FREE = 90;                    # release time
```

```
set: real dt = 1.000000e-03;

set: real E = 4.516e+10;     # glass-reinforced polyester matrix
set: real A = 0.000761048;   # section area
set: real rho = 1850;        # [kg/m^3] GRP
set: real m = rho*A;         # mass per unity length
set: real nu = 0.3;
set: real G = 5.6e+09;
set: real chord = 0.185000;
set: real height = 0.027750;
## area moment of inertia
set: real Iy = 4.18211e-07;
set: real Iz = 5.5311e-08;
set: real Ip = Iy + Iz;

set: real EA = E*A;          # N, main orientation in x-direction,
   extensional stiffness x, axial force
set: real GAy = G*0.833*A;   # N, shear force
set: real GAz = G*0.833*A;   # N
set: real GJ = G*Ip;         # Nm^2, torsional stiffness
set: real EJy = E*Iy;        # Nm^2,
set: real EJz = E*Iz;        # Nm^2
begin: data;
  problem: initial value;
end: data;

begin: initial value;
  initial time: 0.;
  final time: 120.000000;
  time step: dt;

  max iterations: 200;
  tolerance: 1.e-3;

  linear solver:
#   naive;
    umfpack;

  output: iterations;
```

```
    # derivatives coefficient: 1.e-6;
      derivatives tolerance: 1e-1;
      derivatives max iterations: 20;
66
    end: initial value;

    begin: control data;
      structural nodes:
71      +1       # ground
        +1       # machine center
        +1       # rotational centers
        +2*N*Nz # blades + dummy
      ;
76    rigid bodies:
        +117     #
      ;
      joints:
        +2         # clamp
81      +2         # drives
        +3*N       # root only
      ;
      beams: N*(Nz-1);
      forces: 1;
86
      default output: all;
    end: control data;

    set: integer GROUND = 1;     # absolute ground
91  set: integer FRAME = 2;      # body with inertia
    set: integer BEARING1 = 10; # bearing, fixed to frame
    set: integer BEARING2 = 20;
    set: integer CENTER1 = 100; # center of first turbine

96  reference: GROUND,
      reference, global, null,
      reference, global, eye,
      reference, global, null,
      reference, global, null;
101
```

```
    reference: FRAME,
      reference, GROUND, 0.,0., START,
      reference, GROUND, eye,
      reference, GROUND, null,
106   reference, GROUND, null;

    reference: BEARING1,
      reference, FRAME, 0.,0., 0,
      reference, FRAME, eye,
111   reference, FRAME, null,
      reference, FRAME, null;

    # rotation of main frame
    reference: CENTER1,
116   reference, FRAME, 0., 0., 0,
      reference, FRAME, 1, cos(initalpha), sin(initalpha), 0.,    3,
         0., 0., 1.,
      reference, FRAME, null,
      reference, FRAME, null;


121
    set: N_blade = 1;
    set: N_curr = 1;
    include: "vawt_wing.ref";
    set: N_curr = 2;
126 include: "vawt_wing.ref";
    #[...]
    set: N_curr = 39;
    include: "vawt_wing.ref";


131
    set: N_blade = 2;
    set: N_curr = 1;
    include: "vawt_wing.ref";
    set: N_curr = 2;
136 include: "vawt_wing.ref";
    #[...]
    set: N_curr = 39;
    include: "vawt_wing.ref";
```

```
141
    set: N_blade = 3;
    set: N_curr = 1;
    include: "vawt_wing.ref";
    set: N_curr = 2;
146 include: "vawt_wing.ref";
    # [...]
    set: N_curr = 39;
    include: "vawt_wing.ref";

151
    begin: nodes;
      structural: GROUND, static,
        reference, GROUND, null,
        reference, GROUND, eye,
156     reference, GROUND, null,
        reference, GROUND, null;

      structural: FRAME, dynamic,
        reference, FRAME, null,
161     reference, FRAME, eye,
        reference, FRAME, null,
        reference, FRAME, null;

      structural: CENTER1, dynamic,
166     reference, CENTER1, null,
        reference, CENTER1, eye,
        reference, CENTER1, null,
        reference, CENTER1, null;

171 set: N_blade = 1;
    set: N_curr = 1;
    include: "vawt_wing.nod";
    set: N_curr = 2;
    include: "vawt_wing.nod";
176 # [...]
    set: N_curr = 39;
    include: "vawt_wing.nod";
```

```
set: N_blade = 2;
set: N_curr = 1;
include: "vawt_wing.nod";
set: N_curr = 2;
include: "vawt_wing.nod";
#[...]
set: N_curr = 39;
include: "vawt_wing.nod";


set: N_blade = 3;
set: N_curr = 1;
include: "vawt_wing.nod";
set: N_curr = 2;
include: "vawt_wing.nod";
#[...]
set: N_curr = 39;
include: "vawt_wing.nod";


end: nodes;

begin: elements;
  joint: GROUND, clamp, GROUND, node, node;

  joint: FRAME, clamp, FRAME, node, node;

  force: 3, external structural,
    socket,
    create, yes,
    path, "mbdyn.sock",
    coupling,
      tight,
    send after predict, no,
    reference node, GROUND,
    labels, no,
    orientation, orientation matrix, # default
    use reference node forces , yes,
    N*Nz,
      1010,
```

```
221         1020,
    #       [...]
            3390;


226 ### Center node joints

    ## driven rotation
      driven: CENTER1+3, string, "Time < FREE",
      joint: CENTER1+3, axial rotation,
231         FRAME,
              position, null,
                  hinge,
                      1, 1.,0.,0., 2, 0.,1.,0.,
                  CENTER1,
236           reference, FRAME, null,              # relative rotating
                 point position
                  hinge,
                      1, 1.,0.,0., 2, 0.,1.,0.,
              ramp, OMEGA/(FADEIN_END-FADEIN_START), FADEIN_START,
                 FADEIN_END, 0;# drive caller: ramp, slope, init time,
                 final time, init val

241 ## free rotation by revolute hinge
      driven: CENTER1+4, string, "Time >= FREE",
      joint: CENTER1+4, revolute hinge,
          FRAME,
            position, null,
246             CENTER1,
            reference, FRAME, null,
                        hinge,
                                1, 1.,0.,0., 2, 0.,1.,0. ;


251 set: N_blade = 1;
    set: N_curr = 1;
    include: "vawt_wing_body.elm";
    set: N_curr = 2;
    include: "vawt_wing_beam.elm";
256 #[...]
    set: N_curr = 39;
```

```
include: "vawt_wing_beam.elm";


set: N_blade = 2;
set: N_curr = 1;
include: "vawt_wing_body.elm";
set: N_curr = 2;
include: "vawt_wing_beam.elm";
#[...]
set: N_curr = 39;
include: "vawt_wing_beam.elm";


set: N_blade = 3;
set: N_curr = 1;
include: "vawt_wing_body.elm";
set: N_curr = 2;
include: "vawt_wing_beam.elm";
#[...]
set: N_curr = 39;
include: "vawt_wing_beam.elm";


end: elements;
```

Listing C.2: MBDyn input file `vawt_wing.ref`

```
# N_curr: blade number
# N_blade: turbine number

set: BLADE = 1000*N_blade+N_curr*10;     # local blade number
set: CENTER = 100;                       # global center

# rotation of mass node
reference: BLADE,
  reference, CENTER, 0., 0., SPAN*(N_curr-1)/(Nz-1),
  reference, CENTER, 1, cos(2*pi*(N_blade-1)/N), sin(2*pi*(N_blade
     -1)/N), 0.,   3, 0., 0., 1.,
  reference, CENTER, null,
  reference, CENTER, null;
```

Listing C.3: MBDyn input file `vawt_wing.nod`

```
# N_curr: blade number
# N_blade: turbine number

set: BLADE = 1000*N_blade+N_curr*10;        # local blade number

structural: BLADE, dynamic,
  reference, BLADE, 0., radius, 0.,
  reference, BLADE,
    1, cos(AOA),   sin(AOA),        0,    # x:
    3, 0.,         0.,              1.,   # z: heading right
  reference, BLADE, null,
  reference, BLADE, null;

structural: BLADE+10000, dummy, BLADE, relative frame, CENTER1;
```

Listing C.4: MBDyn input file `vawt_wing_body.elm`

```
# N_curr: blade number
# N_blade: turbine number

set: BLADE = 1000*N_blade+N_curr*10;    # local blade number
set: CENTER = 100;                      # local center

# body
body: BLADE, BLADE,
  dL*m, null,
  reference, CENTER, diag, 1./12.*dL^3*m, 1./12.*dL^3*m, 0.;

# connect center and 1st node
joint: BLADE, distance,
  CENTER,
  BLADE,
  radius;

joint: BLADE+1, in line,
  CENTER,
  position, null,
  orientation, reference, BLADE, 1, 1.,0.,0., 3, 0.,1.,0., #
     heading towards mass 2 from center
  BLADE;
```

```
# rotate 1st node parallel to center node
joint: BLADE+2, prismatic,
  CENTER, orientation, reference, BLADE, 1, 1.,0.,0., 2, 0.,1.,0.,
  BLADE;
```

Listing C.5: MBDyn input file `vawt_wing_beam.elm`

```
# N_curr: blade number
# N_blade: turbine number

set: BLADE = 1000*N_blade+N_curr*10;  # local blade number
set: CENTER = 100;                    # global center

### BODY
body: BLADE, BLADE,
  dL*m, null,
  reference, CENTER, diag, 1./12.*dL^3*m, 1./12.*dL^3*m, 0.;

### BEAM2
## two-node beam
beam2: BLADE,
  BLADE-10, null,
  BLADE, null,
  from nodes,
  linear viscoelastic generic,
    diag, GAz, GAy, EA, EJz, EJy, GJ,
    proportional, 0.1;
```

BIBLIOGRAPHY

[ADS45] Ira H. Abbott, Albert E. Von von Doenhoff, and Louis S. Stivers Jr. *Summary of airfoil data*. Tech. rep. 824. National Advisory Committee for Aeronautics, 1945.

[And85] John D. Jr. Anderson. *Fundamentals of aerodynamics*. McGraw-Hill, 1985.

[Baa12] J. H. Baayen. "Vortexje-An Open-Source Panel Method for Co-Simulation". In: *arXiv preprint arXiv:1210.6956* (2012), pp. 1–12.

[Ban+13] Joseph Banks et al. "Fluid structure interaction analyses of tidal turbines". In: *Proceedings of the 16th Numerical Towing Tank Symposium* (2013), pp. 2–7.

[Baz+14] Y. Bazilevs et al. "Fluid-Structure Interaction Modeling of Vertical-Axis Wind Turbines". In: *Journal of Applied Mechanics* 81.8 (2014), p. 081006.

[BD12] S. Brändli and A. Düster. "A flexible multi-physics coupling interface for partitioned solution approaches". In: *Proceedings in Applied Mathematics and Mechanics* 12 (2012), pp. 363–364.

[BE98] Robert M. Bennett and John W. Edwards. "An Overview of Recent Developments in Computational Aeroelasticity". In: *29th AIAA Fluid Dynamics Conference*. 98-2421. 1998.

[Ben+11] Moble Benedict et al. "Aeroelastic Analysis of a Micro-Air-Vehicle-Scale Cycloidal Rotor in Hover". In: *AIAA Journal* 49.11 (2011), pp. 2430–2443.

[BKF12] Alfred E. J. Bogaers, S. Kok, and T. Franz. "Strongly Coupled Partitioned FSI Using Proper Orthogonal Decomposition". In: *Proceedings of the Eighth South African Conference on Computational and Applied Mechanics*. Sept. 2012, pp. 173–180.

[Bog+14] Alfred E. J. Bogaers et al. "Quasi-Newton methods for implicit black-box FSI coupling". In: *Comput. Methods Appl. Mech. Engrg.* 279 (2014), pp. 113–132.

[Bos03] Ervin Bossanyi. "Wind Turbine Control for Load Reduction". In: *Wind Energy* 6.3 (2003), pp. 229–244.

[BS06] Hans-Joachim Bungartz and Michael Schäfer. *Fluid-structure interaction*. Berlin Heidelberg: Springer-Verlag, 2006.

[CGN05] P. Causin, J. F. Gerbeau, and Fabio Nobile. "Added-mass effect in the design of partitioned algorithms for fluid-structure problems". In: *Computer Methods in Applied Mechanics and Engineering* 194.42-44 (2005), pp. 4506–4527.

[CMQ09] Luca Cavagna, Pierangelo Masarati, and Giuseppe Quaranta. "Simulation of Maneuvering Flexible Aircraft By Coupled Multibody/CFD". In: *Multibody Dynamic* (July 2009), pp. 1–29.

[CMQ11] Luca Cavagna, Pierangelo Masarati, and Giuseppe Quaranta. "Coupled Multibody/CFD Simulation of Maneuvering Flexible Aircraft". In: *Journal of Aircraft* 48.1 (2011), pp. 92–106.

[Dan12] Louis Angelo Danao. "The Influence of Unsteady Wind on the Performance and Aerodynamics of Vertical Axis Wind Turbines". PhD thesis. 2012.

[DBV09] Joris Degroote, Klaus-Jürgen Bathe, and Jan Vierendeels. "Performance of a new partitioned procedure versus a monolithic procedure in fluid–structure interaction". In: *Computers & Structures* 87.11-12 (June 2009), pp. 793–801.

[Deg+08] Joris Degroote et al. "Stability of a coupling technique for partitioned solvers in FSI applications". In: *Computers and Structures* 86.23-24 (2008), pp. 2224–2234.

[DEH13] Louis Angelo Danao, Okeoghene Eboibi, and Robert Howell. "An experimental investigation into the influence of unsteady wind on the performance of a vertical axis wind turbine". In: *Applied Energy* 116 (2013), pp. 111–124.

[Del14] Y. Delrieux. "From design to flight testing : overview of rotorcraft acoustic research at Onera for industrial applications". In: *Aerospace Lab* 7.2 (2014), pp. 1–10.

[Dep10] A Deperrois. *XFLR5: a tool for the design of airfoils, wings and planes operating at low Reynolds numbers*. 2010.

[Dre89] Mark Drela. "XFOIL - An analysis and design system for low Reynolds number airfoils". In: *Low Reynolds Number Aerodynamics*. Springer-Verlag, 1989.

[FE10] Jörg Fehr and Peter Eberhard. "Simulation process of flexible multibody systems with non-modal model order reduction techniques". In: *Multibody System Dynamics* 25.3 (Dec. 2010), pp. 313–334.

[Fer11] M. A. Fernández. "Coupling schemes for incompressible fluid-structure interaction: implicit, semi-implicit and explicit". In: *SeMa Journal* 55.1 (2011), pp. 55–108.

[FP12] Joel H. Ferziger and Milovan Perić. *Computational Methods for Fluid Dynamics*. 3rd ed. Springer, 2012.

[FWR07] Christiane Förster, Wolfgang A. Wall, and Ekkehard Ramm. "Artificial added mass instabilities in sequential staggered coupling of nonlinear structures and incompressible viscous flows". In: *Computer Methods in Applied Mechanics and Engineering* 196.7 (2007), pp. 1278–1293.

[Gal10] T. G. Gallinger. "Effiziente Algorithmen zur partitionierten Lösung stark gekoppelter Probleme der Fluid-Struktur-Wechselwirkung". PhD thesis. 2010, p. 183.

[GTK06] Sebastian Geller, Jonas Tölke, and Manfred Krafczyk. "Lattice-Boltzmann Method on Quadtree-Type Grids for Fluid-Structure Interaction". In: *Fluid-Structure Interaction*. Ed. by Hans-Joachim Bungartz and Michael Schäfer. Vol. 53. Berlin Heidelberg: Springer-Verlag, 2006, pp. 270–293.

[Gun+13] Gael Gunnebaud et al. *Eigen - a C++ Linear Algebra Library*. 2013.

[Guy65] Robert J. Guyan. "Reduction of stiffness and mass matrices". In: *AIAA Journal* 3.2 (1965), pp. 380–380.

[GW01] F. Gruttmann and W. Wagner. "Shear correction factors in Timoshenko's beam theory for arbitrary shaped cross-sections". In: *Computational Mechanics* 27.3 (2001), pp. 199–207.

[Hau08] E. Hau. *Windkraftanlagen: Grundlagen, Technik, Einsatz, Wirtschaftlichkeit*. Berlin Heidelberg: Springer, 2008.

[Hil83] D. J. Hilton. "Performance of a Darrieus Water Turbine at Various Solidities". In: *8th Australasian Fluid Mechanics Conference*. 1983.

[HT06] Jaroslav Hron and Stefan Turek. "A monolithic FEM/multigrid solver for an ALE formulation of fluid-structure interaction with applications in biomechanics". In: *Fluid-Structure Interaction*. Ed. by Hans-Joachim Bungartz and Michael Schäfer. Vol. 53. Berlin Heidelberg: Springer-Verlag, 2006, pp. 146–170.

[HWD04] Björn Hübner, Elmar Walhorn, and Dienter Dinkler. "A monolithic approach to fluid-structure interaction using space-time finite elements". In: *Computer methods in applied mechanics and engineering* 193.23 (2004), pp. 2014–2087.

[HWL12] Gene Hou, Jin Wang, and Anita Layton. "Numerical Methods for Fluid-Structure Interaction - A Review". In: *Communications in Computational Physics* 12.2 (2012), pp. 337–377.

[IT69] Bruce M. Irons and Robert C. Tuck. "A version of the Aitken accelerator for computer iteration". In: *International Journal for Numerical Methods in Engineering* 1.3 (July 1969), pp. 275–277.

[Jon52] George Jr. W. Jones. "Investigation of the effects of variations in the Reynolds number between 0.4×10^6 and 3.0×10^6 on the low-speed aerodynamic characteristics of three low-aspect-ratio symmetrical wings with rectangular plan forms." In: *National Advisory Committee for Aeronautics Research* (1952).

[JWP33] E. N. Jacobs, K. E. Ward, and R. M. Pinkerton. "The characteristics of 78 related airfoil sections from tests in the variable-density wind tunnel". In: *National Advisory Committee for Aeronautics* 1820 (1933).

[KB07a] P. Koutsovasilis and M. Beitelschmidt. "Model reduction comparison for the elastic crankshaft mechanism". In: *Proc. Int. Operational Modal Analysis Conference (IOMAC)*. Copenhagen, 2007.

[KB07b] P. Koutsovasilis and M. Beitelschmidt. "Model reduction of large elastic systems: A comparison study on the elastic piston rod". In: *Proc. XII World Congress in Mechanism and Machine Science, Besancon, IFToMM* (2007).

[Kor+13] A. Korobenko et al. "Aerodynamic Simulation of Vertical-Axis Wind Turbines". In: *Journal of Applied Mechanics* 81.2 (2013), p. 021011.

[KP01] Joseph Katz and Allen Plotkin. *Low-Speed Aerodynamics*. 2nd ed. Cambridge: Cambridge University Press, 2001.

[KW08] Ulrich Küttler and Wolfgang A. Wall. "Fixed-point fluid–structure interaction solvers with dynamic relaxation". In: *Computational Mechanics* 43.1 (Feb. 2008), pp. 61–72.

[LE07] Michael Lehner and Peter Eberhard. "A two-step approach for model reduction in flexible multibody dynamics". In: *Multibody System Dynamics* 17.2-3 (Feb. 2007), pp. 157–176.

[Lin+15] Florian Lindner et al. "A comparison of various quasi-newton schemes for partitioned fluid-structure interaction". In: *ECCOMAS Coupled Problems* (2015), pp. 1–12.

[Mac86] Allan J. Macleod. "Acceleration of vector sequences by multi-dimensional Δ^2 methods". In: *Communications in Applied Numerical Methods* 2.4 (1986), pp. 385–392.

[Mas13] Pierangelo Masarati. *MBDyn Input File Format Version 1.5.5*. aero.polimi.it, 2013.

[Mas14] Pierangelo Masarati. *MBDyn Input File Format Version 1.6.0*. aero.polimi.it, 2014.

[Men93] F. R. Menter. "Zonal two-equation k-ω turbulence models for aerodynamic flows". In: *24th AIAA Fluid Dynamic Conference*. 1993.

[Men94] F. R. Menter. "Two-equation eddy-viscosity turbulence models for engineering applications". In: *AIAA Journal* 32.8 (1994), pp. 1598–1605.

[MMM14] P. Masarati, M. Morandini, and P. Mantegazza. "An Efficient Formulation for General-Purpose Multibody/Multiphysics Analysis". In: *ASME J. Comput. Nonlinear Dyn.* 9.4 (2014), p. 041001.

[MPB11] F. Mendes, D. Poirel, and A. Benaissa. "Experimental Investigation of Small Amplitude Self- Sustained Pitch-Heave Oscillations of a NACA0012 Airfoil at Transitional Reynolds Numbers". In: *CASI* (2011), pp. 1–13.

[MS11] Pierangelo Masarati and J. Sitaraman. "Tightly Coupled CFD/Multibody Analysis of NREL Unsteady Aerodynamic Experiment Phase VI Rotor". In: *AIAA Aerospace Sciences Meeting*. 2011.

[MT91] K. W. McAlister and R. K. Takahashi. *NACA 0015 wing pressure and trailing vortex measurements*. Tech. rep. 3151. National Aeronautics and Space Administration, 1991.

[Nav23] C. L. M. H. Navier. "Mémoire sur les lois du mouvement des fluides". In: *Mémoires de l'Académie Royale des Sciences de l'Institut de France* 6 (1823), pp. 389–440.

[OAR89] J. O'Callahan, P. Avitabile, and R. Riemer. "System equivalent reduction expansion process (SEREP)". In: *Proceedings of 7th International Modal Analysis Conference*. 1989, pp. 29–37.

[PAH15] B. Paillard, J. A. Astolfi, and F. Hauville. "URANSE simulation of an active variable-pitch cross-flow Darrieus tidal turbine: Sinusoidal pitch function investigation". In: *International Journal of Marine Energy* 11 (2015), pp. 9–26.

[Par02] Ion Paraschivoiu. *Wind turbine design with Emphasis on Darrieus concept*. Polytechnic International Press, 2002.

[Par81] Ion Paraschivoiu. "Double-multiple streamtube model for Darrieus in turbines". In: *Wind Turbine Dynamics*. Ed. by R. W. Thresher. May 1981, pp. 19–25.

[PB10] Ludwig Prandtl and Albert Betz. *Vier Abhandlungen zur Hydrodynamik und Aerodynamik*. Vol. 3. Universitätsverlag Göttingen, 2010.

[Pra23] L. Prandtl. *Applications of modern hydrodynamics to aeronautics*. Tech. rep. 116. National Advisory Committee for Aeronautics Research, 1923.

[QMM05] Giuseppe Quaranta, Pierangelo Masarati, and Paolo Mantegazza. "A Conservative Mesh-Free Approach for Fluid-Structure Interface Problems". In: *International Conference for Coupled Problems in Science and Engineering*. Greece, 2005, p. 23.

[Qu04] Zu-Qing Qu. *Model reduction techniques: with applications in finite element analysis*. London Berlin Heidelberg: Springer-Verlag, 2004, p. 369.

[Ren14] Yves Renard. *GetFEM++*. `http://download.gna.org/getfem/html/homepage/index.html`. 2014.

[RS88] Robert E. Roberson and Richard Schwertassek. *Dynamics of multibody systems*. Springer-Verlag, 1988.

[Sch07] H. Schürmann. *Konstruieren mit Faser-Kunststoff-Verbunden*. Berlin: Springer, 2007, p. 672.

[SE12] W. Schiehlen and P. Eberhard. *Technische Dynamik*. 3rd ed. Stuttgart: Vieweg+Teubner Verlag, 2012.

[Sha97] Ahmed A. Shabana. "Flexible multibody dynamics: review of past and recent developments". In: *Multibody system dynamics* 1 (1997), pp. 189–222.

[SK81] R. E. Sheldahl and P. C. Klimas. *Aerodynamic characteristics of seven symmetrical airfoil sections through 180-degree angle of attack for use in aerodynamic analysis of vertical axis wind*. Tech. rep. SAND-80-2114. Sandia National Laboratories, 1981.

[Som14] H. J. III Sommer. *polygeom*. `http://www.mathworks.com/matlabcentral/fileexchange/319-polygeom-m`. 2014.

[SS02] J. N. Sørensen and W. Z. Shen. "Numerical modelling of Wind Turbine Wakes". In: *Journal of Fluids Engineering* 124 (2002), pp. 393–399.

[Sto45] George Gabriel Stokes. *On the Friction of Fluids in Motion, and the Equilibrium and Motion of Elastic Solids*. 1845.

[Str75] J. H. Strickland. *The Darrieus Turbine: A Performance Prediction Method Using Multiple Stream Tubes*. Tech. rep. SAND75-0431. Sandia Laboratories, 1975.

[Tro08] Niels Troldborg. "Actuator Line Modeling of Wind Turbine Wakes". PhD thesis. 2008, p. 142.

[TSM07] Niels Troldborg, Jens N. Sørensen, and Robert Mikkelsen. "Actuator Line Simulation of Wake of Wind Turbine Operating in Turbulent Inflow". In: *Journal of Physics: Conference Series*. Vol. 75. 1. 2007, p. 012063.

[UB13] B. Uekermann and H.-J. Bungartz. "A parallel, black-box coupling algorithm for fluid-structure interaction". In: *Proceedings of 5th International Conference on Computational Methods for Coupled Problems in Science and Engineering*. 2013, pp. 1–12.

[Vah+01] M. Vahdati et al. "Mechanisms and Prediction Methods for Fan Blade Stall Flutter". In: *Journal of Propulsion and Power* 17.5 (2001), pp. 1100–1108.

[Val14] David Vallverdú. "Study on vertical-axis wind turbines using streamtube and dynamic stall models". PhD thesis. 2014.

[Vie06] Jan Vierendeels. "Implicit coupling of partitioned fluid-structure interaction solvers using reduced-order models". In: *Fluid-Structure Interaction*. Ed. by Hans-Joachim Bungartz and Michael Schäfer. Vol. 53. Berlin Heidelberg: Springer-Verlag, 2006.

[Vor92] H. A. van der Vorst. "Bi-CGSTAB: A Fast and Smoothly Converging Variant of Bi-CG for the Solution of Nonsymmetric Linear Systems". In: *SIAM Journal on Scientific and Statistical Computing* 13.2 (1992), pp. 631–644.

[Wal91] Oskar Wallrapp. "Linearized Flexible Multibody Dynamics Including Geometric Stiffening Effects". In: *Journal of Structural Mechanics* 19.3 (1991), pp. 37–41.

[Wal94] Oskar Wallrapp. "Standardization of Flexible Body Modeling in Multibody System Codes, Part I: Definition of Standard Input Data*". In: *Journal of Structural Mechanics* 22.3 (1994), pp. 37–41.

[Weg10] Michiel Weghs. "Efficiency Improvement of Strongly Coupled Fluid-Structure Interaction Simulations". PhD thesis. 2010.

[Wen06] Holger Wendland. "Spatial coupling in aeroelasticity by meshless kernel-based methods". In: *European Conference on Computational Fluid Dynamics*. 2006, pp. 1–12.

[Wen15] Arne Wenzel. "Modeling lifting devices in hydrodynamics using actuator methods". PhD thesis. 2015.

[Wen95] Holger Wendland. "Piecewise polynomial, positive definite and compactly supported radial functions of minimal degree". In: *Advances in Computational Mathematics* 4.1 (1995), pp. 389–396.

[WF58] L. F. Whicker and L. F. Fehlner. *Free-stream characteristics of a family of low-aspect-ratio, all-movable control surfaces for application to ship design*. Tech. rep. 933. Washington, D. C.: David Taylor Model Basin, Dec. 1958.

[Whi+07] Trevor Whittaker et al. "The development of Oyster - A shallow water surging wave energy converter ". In: *7th European Wave and Tidal Energy Conference* (2007).

[WLW76] R. E. Wilson, P. B. S. Lissaman, and S. N. Walker. *Aerodynamic performance of wind turbines*. Tech. rep. Corvallis, Oregon: Oregon State University, 1976.

[WM10] Christophe Sibuet Watters and Christian Masson. "Modeling of lifting-device aerodynamics using the actuator surface concept". In: *International Journal for Numerical Methods in Fluids* 62.11 (2010), pp. 1264–1298.

[WT98] H. G. Weller and G. Tabor. "A tensorial approach to computational continuum mechanics using object-oriented techniques". In: *Computers in Physics* 12.6 (1998), pp. 620–631.

[YLV07] Camille Yvin, Alban Leroyer, and Michel Visonneau. "Co-simulation in fluid-structure interaction problem with rigid bodies". In: *Numerical Towing Tank Symposium 23-25*. 2007.

[YQ00] Yun Ye and Z.-Q. QU. "Iterative methods for dynamic condensation of structural matrices". In: *SPIE proceedings series*. Society of Photo-Optical Instrumentation Engineers. 2000, pp. 1776–1782.

[Bun14] Bundesverband der Energie- und Wasserwirtschaft e. V. *BDEW aktualisiert Angaben zum Erzeugungsmix 2014: Erneuerbare Energien erzeugen immer mehr Strom*. Press release. BDWE.de, 2014, pp. 1–2.

[Eur14] European Commission. *A policy framework for climate and energy in the period from 2020 to 2030*. COM(2014) 15 final. 2014, pp. 1–18.

[Eur15] European Commission. *Horizon 2020 - Work Programme 2014-2015*. Decision C (2015)2453. Apr. 2015.

[Ope14] OpenFOAM Foundation. *OpenFOAM - The open source CFD toolbox*. `http://www.openfoam.org/`. 2014.

[Pre12] Presse- und Informationsamt der Bundesregierung. *Erneuerbare Energien - tragende Säule künftiger Energieversorgung*. Press release. Bundesregierung.de, 2012.

[Sac11] Sachverständigenrat für Umweltfragen. *Erneuerbare Energien bis 2050 kostengünstigste Energieträger für Europa*. Press release. Umweltrat.de, 2011.

[Sta14] Statistisches Bundesamt. *Klimaschutzbranche 2012: 40,3 Milliarden Euro Umsatz*. Press release. Destatis.de, 2014.

[Van78] Thong Van Nguyen. "A Vortex Model of the Darrieus Turbine". M.Sc. Texas Tech University, 1978.